

AD-A192 212

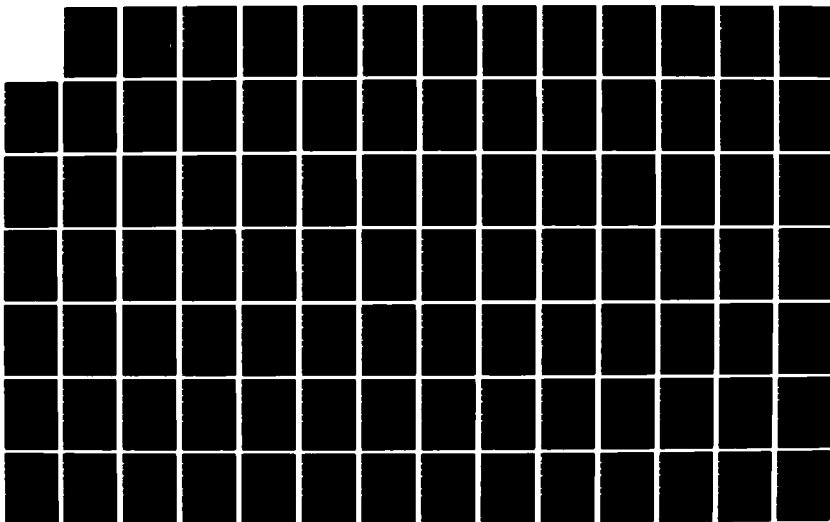
FORWARD AND INVERSE MODELING OF NEAR-FIELD SEISMIC  
WAVEFORMS FROM UNDERGR (U) WOODWARD-CLYDE CONSULTANTS  
PASADENA CA L J BURDICK ET AL 85 APR 87 MCCP-R-87-81  
AFGL-TR-87-8258 F19628-85-C-0036

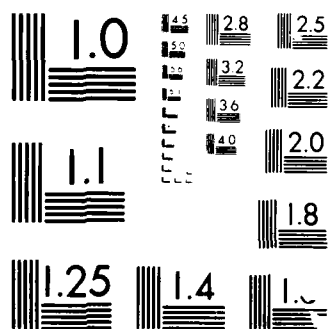
172

UNCLASSIFIED

F/G 8/11

NL





MICROCOPY RESOLUTION TEST CHART  
 NATIONAL BUREAU OF STANDARDS-1963-A

4

AFGL-TR-87-0250

FILE COPY

Forward and Inverse Modeling of Near-Field  
Seismic Waveforms From Underground Nuclear  
Explosions for Effective Source Functions  
and Structure Parameters

L.J. Burdick  
J.S. Barker

Woodward-Clyde Consultants  
566 El Dorado Street  
Suite 100  
Pasadena, CA 91101

5 April 1987

Final Report  
5 September 1986-5 March 1987

APPROVED FOR PUBLIC RELEASE; DISTRIBUTION UNLIMITED

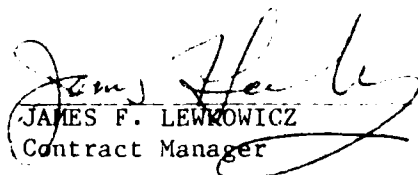
AIR FORCE GEOPHYSICS LABORATORY  
AIR FORCE SYSTEMS COMMAND  
UNITED STATES AIR FORCE  
HANSCOM AIR FORCE BASE, MASSACHUSETTS 01731-5000

DTIC  
ELECTE  
FEB 03 1988  
S D  
CH

AD-A192 212

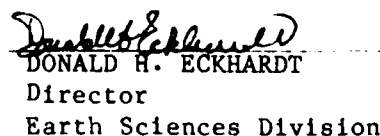
88 1 26 050

"This technical report has been reviewed and is approved for publication."

  
JAMES F. LEWKOWICZ  
Contract Manager

  
HENRY A. OSSING  
Chief, Solid Earth Geophysics Branch

FOR THE COMMANDER

  
DONALD H. ECKHARDT  
Director  
Earth Sciences Division

This report has been reviewed by the ESD Public Affairs Office (PA) and is releasable to the National Technical Information Service (NTIS).

Qualified requestors may obtain additional copies from the Defense Technical Information Center. All others should apply to the National Technical Information Service.

If your address has changed, or if you wish to be removed from the mailing list, or if the addressee is no longer employed by your organization, please notify AFGL/DAA, Hanscom AFB, MA 01731. This will assist us in maintaining a current mailing list.

Do not return copies of this report unless contractual obligations or notices on a specific document requires that it be returned.

UNCLASSIFIED

SECURITY CLASSIFICATION OF THIS PAGE

## REPORT DOCUMENTATION PAGE

1a. REPORT SECURITY CLASSIFICATION Unclassified			1b. RESTRICTIVE MARKINGS	
2a. SECURITY CLASSIFICATION AUTHORITY			3. DISTRIBUTION AVAILABILITY OF REPORT Approved for public release; distribution unlimited.	
2b. DECLASSIFICATION/DOWNGRADING SCHEDULE				
4. PERFORMING ORGANIZATION REPORT NUMBER(S) WCCP-R-87-01			5. MONITORING ORGANIZATION REPORT NUMBER(S) AFGL-TR-87-0250	
6a. NAME OF PERFORMING ORGANIZATION Woodward-Clyde Consultants		6b. OFFICE SYMBOL (If applicable)		7a. NAME OF MONITORING ORGANIZATION Air Force Geophysics Laboratory
6c. ADDRESS (City, State and ZIP Code) 566 El Dorado Street, Suite 100 Pasadena, CA 91101			7b. ADDRESS (City, State and ZIP Code) Hanscom Air Force Base Massachusetts 01731	
8a. NAME OF FUNDING/SPONSORING ORGANIZATION DARPA		8b. OFFICE SYMBOL (If applicable)		9. PROCUREMENT INSTRUMENT IDENTIFICATION NUMBER F19628-85-C-0036
8c. ADDRESS (City, State and ZIP Code) 1400 Wilson Boulevard Arlington, VA 22209			10. SOURCE OF FUNDING NOS.	
			PROGRAM ELEMENT NO 62714E	PROJECT NO. 5A10
			TASK NO. DA	WORK UNIT NO. AV
11. TITLE (Include Security Classification) See block 16; unclassified				
12. PERSONAL AUTHOR(S) L. J. Burdick and J. S. Barker				
13a. TYPE OF REPORT Final Report		13b. TIME COVERED FROM 9/5/86 TO 3/5/87		14. DATE OF REPORT (Yr., Mo., Day) 87/4/5
15. PAGE COUNT 126				
16. SUPPLEMENTARY NOTATION Forward and Inverse Modeling of Near-Field Seismic Waveforms from Underground Nuclear Explosions for Effective Source Functions and Structure Parameters				
17. COSATI CODES			18. SUBJECT TERMS (Continue on reverse if necessary and identify by block number)	
FIELD	GROUP	SUB GR	Inversion of explosion seismic waveforms, near-field observations, effective source functions, strain, non-linear material response	
19. ABSTRACT (Continue on reverse if necessary and identify by block number)  See reverse side			Accession For NTIS GRA&I <input checked="" type="checkbox"/> DTIC TAB <input type="checkbox"/> Unannounced <input type="checkbox"/> Justification By Distribution/ Availability Codes Avail and/or Special Dist A-1	
20. DISTRIBUTION AVAILABILITY OF ABSTRACT UNCLASSIFIED UNLIMITED <input type="checkbox"/> SAME AS RPT <input checked="" type="checkbox"/> DTIC USERS <input type="checkbox"/>			21. ABSTRACT SECURITY CLASSIFICATION Unclassified	
22a. NAME OF RESPONIBLE INDIVIDUAL James Lewkowicz			22b. TELEPHONE NUMBER (Include Area Code) (617) 377-3028	
			22c. OFFICE SYMBOL AFGL/LWH	

It is well established that near field records of nuclear explosions can be analyzed to obtain detailed information about the seismic source function and its dependence on yield. This information is generally formulated in terms of parameterized models for the RDP and for the test site crustal structure. In this study, review the results of forward modeling studies to obtain the source and structure parameters for Pahute Mesa. These models fit the observed near field records well, but there is some question as to how errors in crustal structure might affect seismic source parameters. Furthermore, there is a general need to be able to develop source-structure models in a consistent, unbiased fashion. To address these issues, we have developed a simultaneous inversion for source and structure parameters. In previous reports, we discussed the development of the method and applied it to Pahute Mesa data. In this report, we present an application of an improved technique for inverting for parameters in these types of problems known as the jumping method. The primary advantage of this method is that parameter constraints and error analyses are made on the parameters of the models rather than on the changes in the parameters. We show results of application of the method to artificial and real near-field data sets. Both the utility and limitations of the method have been elucidated. Tradeoffs between parameters are quantified by the error analysis inherent in any inversion method. A second problem with analysis of near-field records from explosions is that there is some question as to whether crustal materials respond in a linear anelastic or anelastic fashion or whether they have significant nonlinear response because of the high shear strain levels. Near-field data sets from several nuclear explosions and an earthquake are examined to address this question. It is shown that if nonlinear material response occurs it does not have a large enough effect to have a significant effect on data interpretation.

FORWARD AND INVERSE MODELING OF NEAR-FIELD SEISMIC WAVEFORMS

FROM UNDERGROUND NUCLEAR EXPLOSIONS

FOR EFFECTIVE SOURCE FUNCTIONS AND STRUCTURE PARAMETERS

## INTRODUCTION

Perhaps the most crucial step in the determination of effective source functions and the estimation of yields from near-field recordings of underground nuclear explosions is the development of an accurate velocity structure model. For ranges outside of the spall zone, the first peak in observed vertical velocity records is often the result of the interference between the direct, upgoing wave and energy that departs downward from the source but is turned by the velocity gradient in the upper crust. Thus the amplitude and width of the source pulse inferred from the observed waveform is quite sensitive to the velocity gradient, particularly near the source depth. Previous studies have obtained detailed velocity structure models through trial-and-error waveform modeling (e.g., Helmberger and Hadley, 1981; Hartzell, et al., 1983; Burdick, et al., 1984). We have used the model of Hartzell, et al. (1983) in a forward modeling study for the source parameters of four Pahute Mesa explosions. The resulting synthetic seismograms provide an admirable fit to the observed waveforms. There is some concern, however, regarding the adequacy of the structure model for a variety of locations within Pahute Mesa. In particular, we need to consider how potential errors in the structure model effect the values determined for the source parameters. An additional problem is that in determining source parameters from explosions in a completely different structure (e.g., Yucca Flats, Amchitka, or one of the Soviet test sites), a new velocity structure model must first be determined.



In order to address these issues, we have developed a simultaneous inversion method which solves for the parameters of both the source and velocity structure models. A report on the initial development of the method was given in Barker, et al. (1985b) and the application of this method to Pahute Mesa data was presented in Barker, et al. (1986). We have improved the inversion technique by incorporating the jumping method of Shaw and Orcutt (1985). The primary improvement in this technique is that parameter constraints and error analyses are made on the parameters of the model, rather than on the changes in the parameters. We present a test inversion of a synthetic data set. The results are quite promising, but also illustrate the limitations in the resolution of deeper structures when limited ranges of observations are considered.

The inversions of waveforms for same four Pahute Mesa explosions are presented and compared with the forward modeling results. In general, the synthetic waveforms from the inversions provide improvements over the forward modeling in amplitude, arrival time, and in some cases, in the detailed shapes of the waveforms. For BOXCAR, the structure model obtained is not significantly different than that of Hartzell, et al. (1983). This is not particularly surprising, since these data were modeled in the development of the Hartzell, et al. (1983) structure. For the other events modeled, there is very little resolution of structure parameters deeper than about 3 km. Above this, however, we will show that the velocity gradient near INLET is very similar to that near BOXCAR, but the gradient is much greater near MAST. The results from SCOTCH suggest that the water table is somewhat deeper than the

constrained value used, but that the gradient below this is similar to that of BOXCAR. The variation in velocity gradient for MAST may be related to its location on the northeast edge of Pahute Mesa.

From the parameters of the effective source functions we may develop scaling relations and estimate yields for the events studied. Barker, et al. (1985a) estimated yields from the forward modeling results. In this report, we use two new relations which are constrained to the announced yields of BOXCAR and SCOTCH. Yields are estimated for all four of the events for which the simultaneous inversion has been performed.

While the resolution of the inversion results depends on the range distribution of the observations, and the results are limited by noise or the effects of lateral structural variations in the observed data, the application to Pahute Mesa waveforms has demonstrated the usefulness of the method. Trade-offs between parameters, particularly between structure and source parameters, are quantified by the error analysis inherent in the inversion method. Finally, the inversion may be applied to near-field waveforms from any site, without any *a priori* information on the crustal velocity structure. This makes such an inversion valuable as one of many on-site verification techniques, enabling the calibration of test sites for treaty monitoring purposes.

#### NEAR-FIELD DATA SET

The near-field data discussed in this study consist of three-component surface recordings of acceleration and velocity digitized by Sandia National

Laboratories and reported by Perret (1976). The events modeled are listed in Table 1 and include BOXCAR, MAST, INLET and SCOTCH. The distribution of stations for each event is given in Table 2 and displayed in Figure 1.

Table 1 - Pahute Mesa Events Modeled

Event	Date	Depth (m)	Yield (kt)
BOXCAR	4/26/68	1160	1300 <sup>1</sup>
MAST	6/19/75	912	520 <sup>2</sup>
INLET	11/20/75	817	500 <sup>2</sup>
SCOTCH	5/23/67	970	155 <sup>1</sup>

<sup>1</sup> announced yield (Marshall, et al., 1979)

<sup>2</sup> estimated yield (Dahlman and Israelson, 1977)

Table 2 - Station Distribution and Arrival Times

BOXCAR	Range (km)	Arrival time <sup>1</sup> (sec)	Residual <sup>3</sup> (sec)	Window start <sup>4</sup> (sec)	Window end <sup>4</sup> (sec)
S-12	3.81	1.26	0.09	1.25	2.05
S-16*	4.87	1.51	0.16	1.55	2.35
S-24*	7.27	2.10	0.16	1.85	3.20
S-34*	10.37	2.92	-0.03	2.70	3.95
S-74*	22.47	4.92	0.32	4.50	6.00

MAST	Range (km)	Arrival time <sup>2</sup> (sec)	Residual <sup>3</sup> (sec)	Window start <sup>4</sup> (sec)	Window end <sup>4</sup> (sec)
S-5*	3.65	1.15	0.14	1.00	1.90
S-6	5.47	1.56	0.26	1.40	2.35
S-7	7.30	2.03	0.29	1.85	2.80

INLET	Range (km)	Arrival time <sup>2</sup> (sec)	Residual <sup>3</sup> (sec)	Window start <sup>4</sup> (sec)	Window end <sup>4</sup> (sec)
S-5	1.63	0.59	0.09	0.40	1.25
S-6*	3.27	1.03	0.15	0.90	1.75
S-7*	6.53	1.99	0.16	1.85	2.70

SCOTCH	Range (km)	Arrival time <sup>1</sup> (sec)	Residual <sup>3</sup> (sec)	Window start <sup>4</sup> (sec)	Window end <sup>4</sup> (sec)
S-3A*	4.13	1.38	0.06	1.20	2.00
S-4*	6.06	1.89	0.12	1.75	2.70

\* Station used by Hartzell, et al. (1983) to determine the structure model

\* Station located outside Silent Canyon caldera

<sup>1</sup> Arrival times from Perret (1976)

<sup>2</sup> Measured arrival times

<sup>3</sup> Time predicted by Hartzell, et al. (1983) model - observed time

<sup>4</sup> Time windows used in the waveform inversion

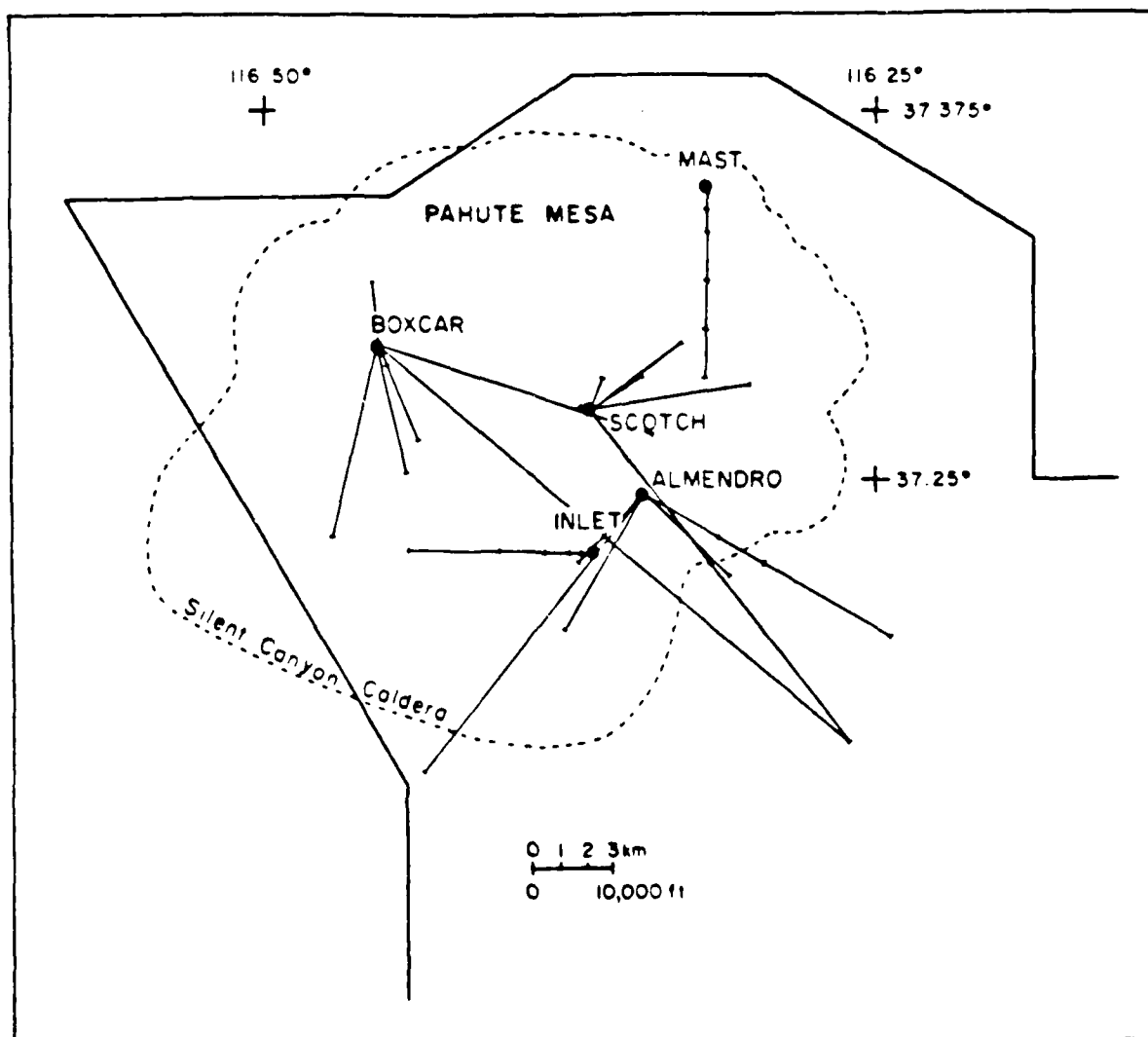


Figure 1. A map of the NTS events studied along with the station lines and locations.

## PAHUTE MESA VELOCITY STRUCTURE MODEL

The velocity structure model for Pahute Mesa was obtained by modeling the arrival times and waveforms of the surface velocity records indicated in Table 2. The model was previously presented by Hartzell, et al. (1983) and is listed in Table 3. A plot of the model as a function of depth is shown in Figure 2, along with a comparison with other models for Pahute Mesa. The P- and S-wave models of Helmberger and Hadley (1981) are shown as dotted lines and the P-wave model of Hamilton and Healy (1969) and the S-wave model of Carroll (1966) are shown as dashed lines.

The validity of the model may be evaluated based on P-wave travel times and the fit of synthetic waveforms to the data. The S-wave velocity structure is based primarily on the amplitude and arrival time of the long-period Rayleigh wave. The ratio of vertical to radial amplitudes may also be used as a criterion since it is particularly sensitive to the velocity gradient near the surface. However, the velocities of the uppermost layers may be expected to vary laterally across Pahute Mesa, so the velocity structure model determined must be considered an average, not intended to fit variations in the amplitude ratios.

The observed P-wave arrival times and the time residuals (predicted - observed) due to the velocity structure model are listed in Table 2. For the nearer receivers the residuals are all less than 0.1 s. The variation in these residuals reflects the lateral velocity variations in the uppermost layers. Only the receivers at ranges greater than 15 km have residuals greater than 0.3 s indicating that the lower layers may be slightly too fast. These

Table 3 - Pahute Mesa Velocity Structure Model\*

Layer	P Velocity (km/s)	S Velocity (km/s)	Density (g/cm <sup>3</sup> )	Thickness (km)
1	2.30	1.35	1.90	0.36
2	2.80	1.50	2.00	0.40
3	3.30	1.50	2.25	0.70
4	4.00	1.90	2.30	0.70
5	4.60	2.00	2.40	0.75
6	5.30	2.50	2.50	0.80
7	5.50	2.95	2.70	2.25
8	6.10	3.50	3.00	10.00
9	7.00	4.00	3.00	10.00

\* from Hartzell, et al. (1983)

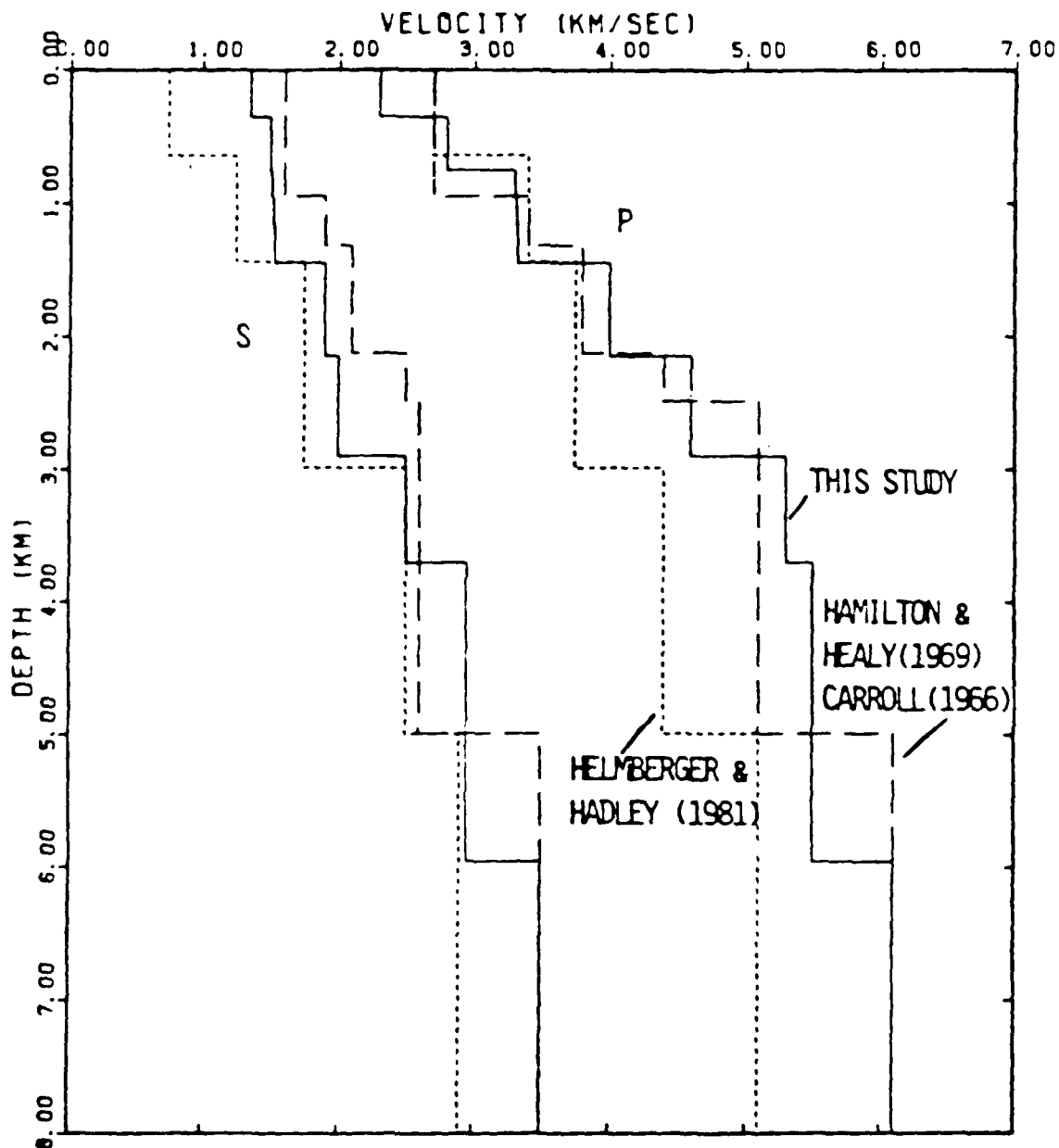


Figure 2. P and S-wave velocity structure for Pahute Mesa obtained by forward modeling (solid curve) compared with two other proposed structures for the area (dashed and dotted curves).



receivers are also located outside of the Silent Canyon Caldera. Other than two rather noisy receivers for MAST, all receivers within 10 km have residuals less than 0.2 s, indicating that the model fits arrival times exceptionally well.

The fits of the synthetic seismograms to the observed data are the subject of the following sections, but an example of the ability of the velocity structure model to account for extensive portions of the observed vertical waveforms is shown in Figure 3. Shown are the vertical velocity recordings for BOXCAR at ranges of 7.26, 7.70 and 10.36 km, along with synthetic seismograms generated using the wavenumber integration technique of Yao and Harkrider (1983). Details of the first 1.5-2.0 s after the P arrival are quite well modeled, as are the amplitude and arrival time of the Rayleigh wave (indicated by an arrow). Later P arrivals may reflect unmodeled phenomena such as spall or tectonic release. The observed P wave at 10.36 km includes frequencies higher than those computed for the synthetics, which accounts for the amplitude discrepancy in the figure. Figure 4 shows a comparison of the observed waveforms at 10.36 and 7.26 km with synthetic seismograms computed by the generalized ray method of Helmberger and Harkrider (1978). While these synthetics cannot match the entire waveform, they contain the high frequencies required to model the first several arrivals. These synthetics will be used in subsequent sections for determining source parameters.

Since the determination of source parameters will depend to a great extent on the amplitude and width of the first pulse of the observed vertical velocity waveform, it is instructive to investigate how the interaction of

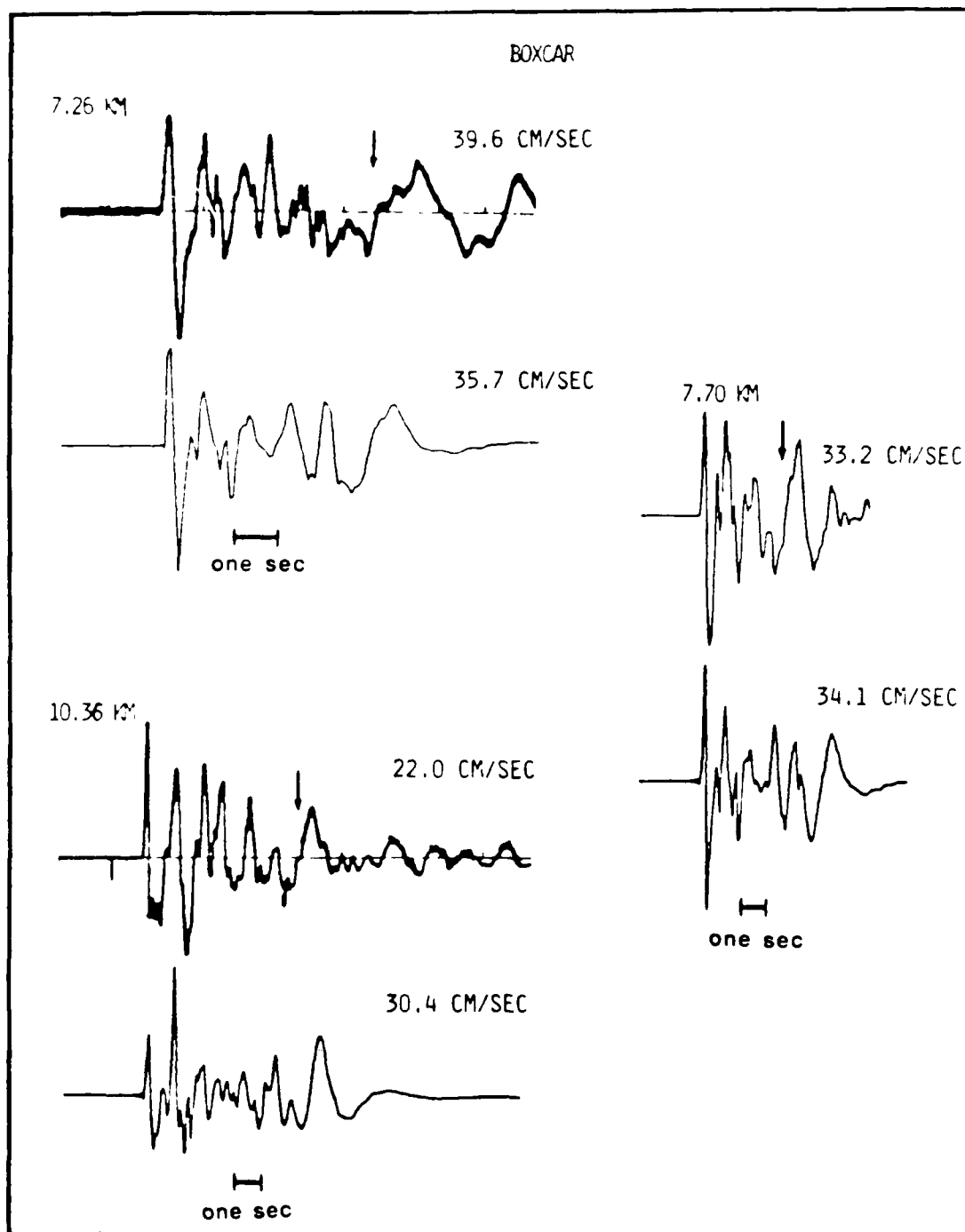


Figure 3. Comparison of the vertical velocity records at distances of 7.26, 7.70, and 10.36 km for BOXCAR (top traces) with synthetics (bottom traces) for the preferred structure in Figure 2 using the full wave theory code KB. Amplitudes in cm/sec are peak values for the entire record.

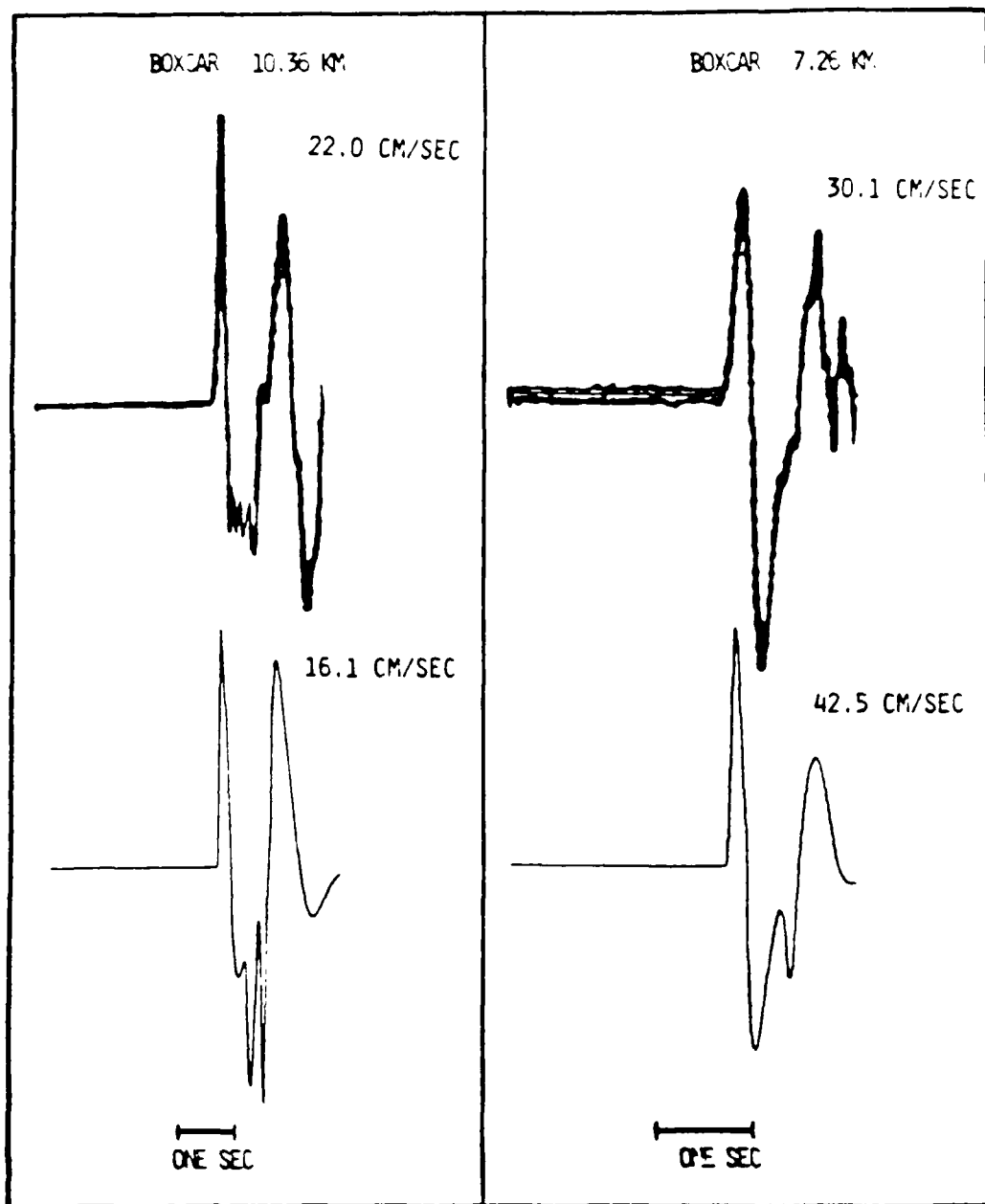


Figure 4. Comparison of the first portion of vertical velocity records for BOXCAR (above) with synthetic seismograms (below) computed using the generalized ray method of Helmberger and Harkrider (1978) for the structure model of Figure 2. The amplitudes of the first peaks (in cm/s) are printed to the right of the traces (from Hartzell, et al, 1983).

different rays through the structure affects the waveshape. Figure 5 shows the decomposition of the vertical component synthetics into various ray types for ranges of 2-12 km from a source with the parameters of BOXCAR. The source is located at a depth of 1.160 km. For each range, the top plot consists of the upgoing P wave only. The next trace is the sum of diving P waves and consists of reflections and refractions from interfaces below the source. The third trace is the sum of pP rays that reflect from the free surface and then reflect or refract from layer interfaces. Below this is the sum of P-to-S conversions at layer interfaces for direct rays, or at reflection points for turning rays. Finally, the bottom trace for each range consists of the sum of all of these rays. Each trace is scaled to the first peak amplitude of the sum trace.

At 2 km, the upgoing P wave is the first arrival and the only significant contribution to the sum. By 4 km, the diving P wave is beyond the critical angle of the first reflector below the source, its amplitude is comparable to that of the direct ray, and it appears impulsive due to the post-critical reflection phase shift. At 6 km, the diving P wave is the first arrival and consists of two post-critical reflections, direct P serves only to broaden the pulse, and pP is beginning to emerge. At 8 km, diving P is the earliest and largest phase, direct P destructively interferes with the backswing and pP is an impulsive late arrival. At 10 km and beyond, individual diving rays begin to separate in time and interfere with pP, which now consists of multiple post-critical rays. For this velocity structure model, at all ranges, P-to-S conversions contribute only negligibly to the vertical synthetics.

To summarize the effects of the velocity structure model on the synthetic waveforms, the upgoing P wave alone is sufficient only for ranges less than about 4 km. In practice, most vertical waveforms for these near ranges would be truncated by the onset of spall immediately after the first peak. For ranges of about 4-8 km, the interference of upgoing and diving P rays can greatly influence the amplitude and pulse width of the first peak. Similarly for ranges greater than 8 km, the first peak is sensitive to the interference of various post-critical diving rays, and the scale of discretization of the velocity gradient becomes important. pP contributes complications later in the P waveform for ranges beyond about 8 km, but S-to-P conversions are not significant in the vertical synthetics at any range.

An implicit assumption in this modeling approach is that the velocity structure may be parameterized as a stack of horizontal, homogeneous layers. The effects of discretizing the vertical velocity gradient have been discussed elsewhere (e.g. see Burdick, et al. 1982), but in general, as long as layer thicknesses are less than the predominant wavelength of the observations, the discretization will not adversely affect the results. While lateral variations in the velocity of the layers above the source or in the thickness of the top layer due to changes in elevation may be noticeable in arrival times and in P-to-S conversions on the radial component, these variations do not appear to have a significant effect on the vertical waveforms. On the other hand, the plane-layer assumption tends to break down as range increases beyond about 10 km, due to the sensitive interaction of head waves and post-critical reflections from deeper layers. Finally, some of the receivers modeled in this study lie outside the boundary of Silent Canyon Caldera, the geologic feature that dominates the subsurface structure of Pahute Mesa. For

these receivers (see Table 2), a plane-layered structure model is probably inappropriate, but the determination of individual, laterally-varying structure models for these receivers is outside the scope of this work.

# WAVEFORM MODELING FOR SOURCE PARAMETERS

The vertical particle velocity due to an explosion source may be written using first order asymptotic generalized ray theory as (see for example, Helmberger and Harkrider, 1978)

$$u_z(R,t) = \Psi''(t) * \frac{1}{n} \sqrt{\frac{2}{R}} \frac{d}{dt} \left( \frac{1}{\sqrt{t}} * \sum_{i=1}^{N_{\text{rays}}} R_i(p) \right) \quad (1)$$

where \* denotes convolution,  $\Psi''(t)$  is the second time derivative of the reduced displacement potential (RDP), and

$$R_i(p) = \Im m \left\{ \sqrt{\frac{p}{\eta_a}} R_{N2}(p) \Pi_i(p) \frac{dp}{dt} \right\}_c \quad (2)$$

which is evaluated along the Cagniard contour.  $p$  is the ray parameter,  $\eta_a$  is the vertical wave slowness ( $\eta_a = [\alpha^{-2} - p^2]^{1/2}$ ),  $R_{N2}(p)$  is the receiver function defined by Helmberger (1974), and  $\Pi_i(p)$  is the product of generalized reflection and transmission coefficients along the path for each ray.

The form of the RDP is generally a modification of that proposed by Haskell (1967):

$$\Psi(t) = \Psi_0 \left\{ 1 - e^{-Kt} \left[ 1 + Kt + \frac{1}{2}(Kt)^2 + \frac{1}{6}(Kt)^3 - B(Kt)^4 \right] \right\} \quad (3)$$

where  $\Psi_0$  represents the static value with dimensions of volume,  $K$  represents the rise time or corner frequency of the source and has dimensions of inverse time, and  $B$  represents the overshoot or the extent to which the spectrum is

peaked at its corner, and is dimensionless. von Seggern and Blandford (1972) truncated the polynomial to a quadratic based on the observed  $\omega^{-2}$  spectral decay of teleseismic, short-period body waves. While Haskell's source model is continuous through acceleration, that of von Seggern and Blandford is continuous only to displacement, is discontinuous to velocity and singular to acceleration. This is obviously insufficient for modeling local velocities and accelerations.

As a compromise, we will use the cubic source function of Helmberger and Hadley (1981):

$$\psi(t) = \psi_{\infty} \left\{ 1 - e^{-Kt} \left[ 1 + Kt + \frac{1}{2}(Kt)^2 - B(Kt)^3 \right] \right\} \quad (4)$$

which is continuous through velocity. The parameters have the same meaning between source models, and in fact,  $\psi_{\infty}$  is the same for all three of the models discussed, but the values of  $K$  and  $B$  will vary between source models. Barker, et al. (1985b) demonstrated that this cubic form of the RDP, when convolved with elastic Green's functions, can explain near-field observations. A quadratic RDP can explain the observations as long as the Green's functions include the effects of depth-dependent attenuation. Rather than attempting to solve for the  $Q$  structure of Pahute Mesa, we have chosen the Helmberger-Hadley RDP and elastic propagation as the simpler model. One disadvantage is that while the von Seggern-Blandford source may be scaled to the empirical RDP of Mueller and Murphy (1971), we must derive scaling relations for the Helmberger-Hadley source. This is done in a following section. As discussed by Burdick, et al. (1982) and Hartzell, et al. (1983), the short durations of locally recorded ground motion provide poor resolution of frequencies well



below the source corner, so  $B$  trades off with  $\Psi_0$ . We therefore fix  $B = 1.0$ , and solve for  $K$  and  $\Psi_0$ . Since the scaling relations are derived within this constraint, errors in the assumption of  $B$  will not adversely affect yield estimates, but should be taken into account when applied to lower frequency data.

The results of forward modeling of the events listed in Table 1 were presented in detail in Barker, et al. (1985a) and are summarized in Table 4. The fits of the synthetic waveforms to the observed vertical velocity records from outside of the spall zone will be compared with the results of the inversion to follow. Barker, et al. (1985a) determined a scaling relation using the model parameters  $\Psi_0$  and  $K$  to estimate the yields shown in Table 4, as well as yields for four additional Pahute Mesa events.

Table 4 - Source Parameters from Forward Modeling

Event	K (s <sup>-1</sup> )	$\Psi_{\infty}$ (x10 <sup>10</sup> cm <sup>3</sup> )	Yield (kt)	published Yield (kt)
BOXCAR	6.5	12.0	1300	1300 <sup>1</sup>
MAST	7.5	4.7	443	520 <sup>2</sup>
INLET	8.0	3.2	286	500 <sup>2</sup>
SCOTCH	12.0	1.3	127	155 <sup>2</sup>

<sup>1</sup> Marshall, et al. (1979)

<sup>2</sup> Dahlman and Israelson (1977)

## WAVEFORM INVERSION METHOD

The layered structure models required for generalized ray synthetics may be considered discretizations of one or more velocity gradients separated by first- or second-order discontinuities. In order to minimize the number of free parameters in the inversion, we will utilize this fact and solve not for the velocities and thicknesses of individual layers, but for the velocity gradient and the velocity at the top of the gradient. As shown in Figure 6, the discretized model follows this gradient, with layer thicknesses determined by the wavelength of the predominant period in the data. Shear velocity and density may be free parameters, or may be related to the compressional velocity by predefined constants. In general, the free parameters are the gradient within each layer, the velocity at the top of the layer, and the depth to the top of the layer. Thus, for an  $n$ -layered structure in which shear velocity and density are not free parameters, the number of structure parameters in the inversion is  $3n-1$ . The number of gradients to be considered will be fixed for each inversion, so the optimal number will have to be determined by test inversions proceeding from simpler to more complex models. Constraints such as the depth to the water table, or that a particular interface may have only a second-order discontinuity, reduce the number of free parameters while increasing non-linearity of the inversion.

Since the discretized velocity model will vary from iteration to iteration as well as with the model perturbations required to compute the numerical partials, the ray set from which the synthetics are computed will

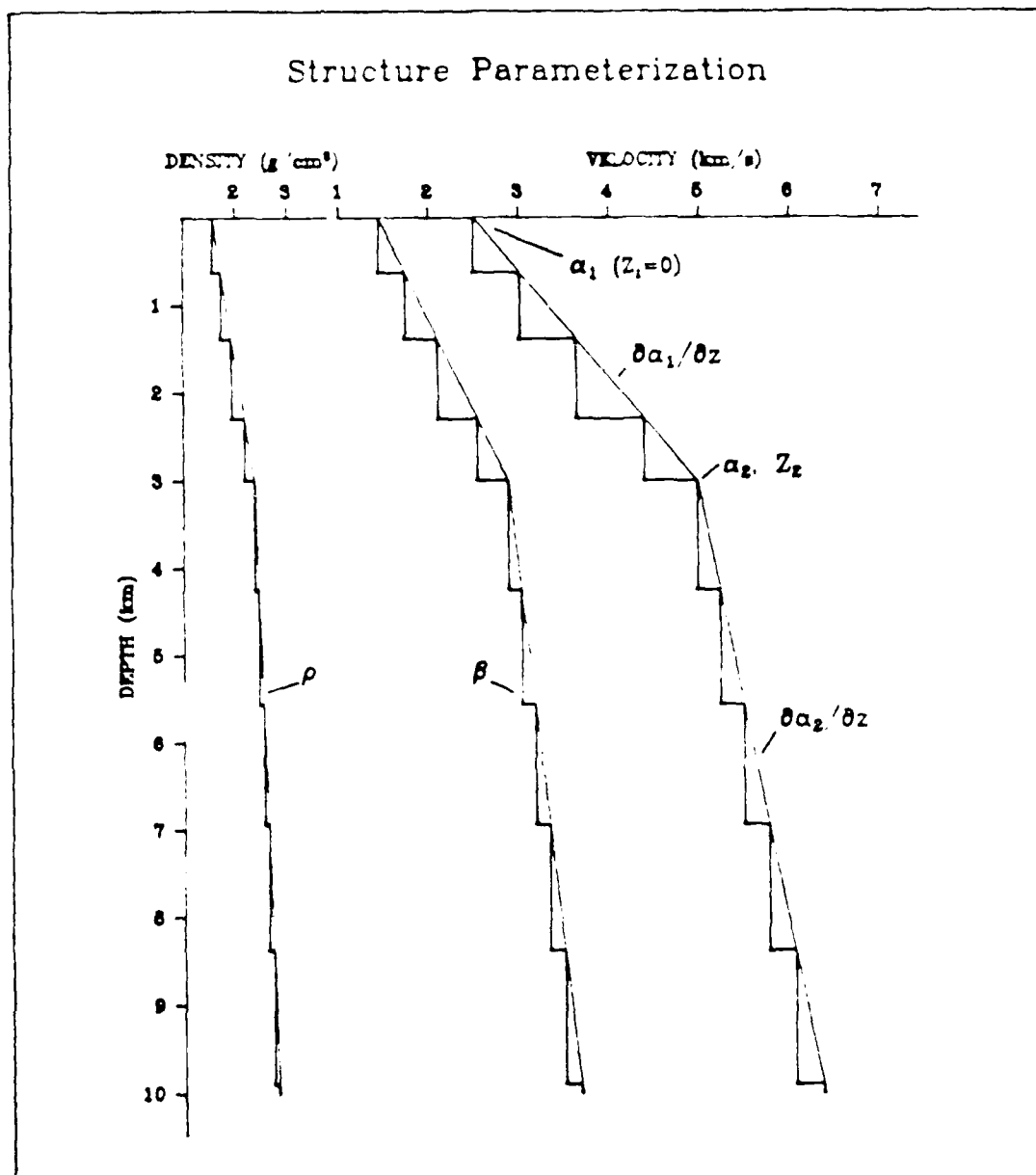


Figure 6. Structure model parameterization. The layered structure model is discretized from one or more velocity gradients defined by the values of the gradient, the velocity at the top of the gradient and the depth to the top of the gradient. The depth increment is defined as the product of the P-wave velocity and the predominant period of the data (typically 0.25 sec). S-wave velocity and density are linearly related to the P-wave velocity. The case shown consists of two gradients separated by a second-order discontinuity.

also vary. Barker, et al. (1985a) found that the first one or two cycles of vertical velocity observations at near-field ranges were well modeled by including the upgoing direct ray, a sum of diving rays that constitute turning, reflecting and critically refracting energy, and a sum of rays that depart upward, reflect from the free surface and follow diving ray paths. If radial observations are to be modeled, or if later portions of the waveform are considered, P-to-S conversions at the free surface and at discontinuities should be included. An algorithm to generate this ray set for each new layered structure is simple to implement, and computational time is saved by culling rays which arrive outside the inversion time window, or whose amplitude will be below some predefined cutoff level.

The linearized least-squares inverse may be obtained by solving

$$\Delta c' = A' \Delta p' \quad (5)$$

in which  $\Delta c'$  is the residual vector, containing the differences between observed and synthetic data,  $A'$  is the matrix of partial derivatives, and  $\Delta p'$  is the desired vector of parameter changes. In this method, we solve for the changes in the model parameters from those of the starting or the previous iteration model. The resulting error analysis gives not the variances of the model parameters, but the variances of the parameter changes. In order to determine error estimates of the final model parameters we must propagate these variances from iteration to iteration in some manner.

Shaw and Orcutt (1985) use a different approach to solve the linearized inverse (which they attribute to Parker, unpublished manuscript, 1985). Rather than inverting equation (5), they add  $\underline{A}'\underline{p}_0'$  (where  $\underline{p}_0'$  contains the starting model) to both sides and invert

$$\underline{J}' = \underline{Jc}' + \underline{A}'\underline{p}_0' = \underline{A}'\underline{p}_0 + \underline{Jp}' = \underline{A}'\underline{p}' \quad (6)$$

to solve directly for the new model parameters,  $\underline{p}'$ . The benefit of (6), which they term the "jumping" method, is that rather than minimizing the parameter changes and obtaining a model dependent on the starting model, one minimizes (by some appropriate norm) the resulting model itself. An additional benefit is that while *a priori* constraints on the model parameters (after Jackson, 1979) may be desired, it is often difficult to transform these into constraints on the parameter changes. While we desire the ability to constrain parameters and to determine error estimates of the parameters rather than the parameter changes, we have a certain level of confidence that our starting model (obtained from forward modeling) is reasonably close to the correct solution. We therefore append a smoothing constraint onto equation (6) such that

$$\underline{p}_0' = \underline{\lambda}\underline{p}' \quad (7)$$

where  $\underline{\lambda}$  is a diagonal matrix of Lagrange multipliers. Thus the inversion attempts to solve one equation for a new set of parameters while simultaneously attempting to equate those parameters to the starting (or previous iteration) model. The relative weights of these conflicting equations are adjusted via the Lagrange multipliers. In practice, we use a single Lagrange multiplier, so  $\underline{\lambda}$  is a constant.

Perhaps the simplest determination of the residual vector is a point-by-point difference of observed and synthetic seismograms within the time window. This implies, however, that neighboring points in a seismogram represent independent observations, which is generally not the case. On the other hand, since each seismogram reflects a lagged sum of rays which sample different portions of the structure, the resolution of parameters varies through the time window, and a single observation for each seismogram underestimates the information contained in the waveform. Burdick and Mellman (1976) utilized an error, or residual, function based on the normalized cross-correlation coefficient between observed and synthetic waveforms. That is,

$$e_i = 1 - \max \hat{o}_i \otimes \hat{s}_i \quad (8)$$

where

$$\hat{o}_i(t) = \frac{o_i(t)}{\sqrt{\int o_i^2(t) dt}} \quad (9)$$

and

$$\hat{s}_i(t) = \frac{s_i(t)}{\sqrt{\int s_i^2(t) dt}} \quad (10)$$

$o_i(t)$  is the  $i^{\text{th}}$  observed seismogram,  $s_i(t)$  is the  $i^{\text{th}}$  synthetic seismogram and  $\otimes$  denotes cross-correlation. This error function has become popular because it is sensitive to the shapes of the waveforms, while the normalization makes it insensitive to absolute amplitude, and measuring the maximum of the cross-correlation makes it insensitive to absolute time. In the near-field

problem, however, absolute amplitude and time are well calibrated, and should be fit by the resultant model. Therefore, in addition to (8), our residual will include for each seismogram the relative difference in the normalization factors,

$$a_i = \frac{\sqrt{\int o_i^2(t)dt} - \sqrt{\int s_i^2(t)dt}}{\sqrt{\int o_i^2(t)dt}} \quad (11)$$

which is a measure of absolute amplitude residual, and the time lag to the maximum of the cross-correlation,  $t_i$ , which is a measure of absolute time residual. The residual vector is now defined as

$$\underline{Jc} = [e_1, a_1, t_1, e_2, a_2, t_2, \dots, e_m, a_m, t_m]^T \quad (12)$$

for  $m$  seismograms. The objective function to be minimized by the inverse is

$$r = \sum_{i=1}^m (e_i^2 + a_i^2 + t_i^2) \quad (13)$$

and the RMS measure of the fit of the synthetics to the data is defined as

$$RMS\ fit = \sqrt{\frac{r}{3 \cdot m}} \quad (14)$$

For the inversion, we must compute the partial derivatives of the residual functions with respect to the individual parameters of the source and velocity structure models. For a particular residual, say  $e_i$ , and parameter, say  $p_j$ , the partial derivative is



$$\frac{\partial e_i}{\partial p_i} = \frac{\partial e_i}{\partial u} \frac{\partial u}{\partial p_i} \quad (15)$$

where  $w'$  is the velocity response of equation (2). If the parameter is  $\psi_*$  or  $B$ , the RDP is linear in these parameters and the partial is easily determined analytically. However, as seen in equation (4), the RDP is nonlinear in  $K$ . Similarly, the partial derivative with respect to a structure parameter, say  $v_j$ , reduces to the evaluation of

$$\frac{\partial R_i(p)}{\partial v_j} = \frac{\partial R_i(p)}{\partial p} \frac{\partial p}{\partial v_j} \quad (16)$$

where  $R_i(t)$  is defined in equation (1). In this case, the partial consists of evaluating the partials of the various factors in  $R_i(p)$  with respect to the complex ray parameter along the Cagniard contour, while the contour itself varies with changes in the velocity parameter. This evaluation must be made for each ray, then summed to obtain the partial derivative.

Previous structure inversions based on waveform modeling have invoked a number of approximations in order to simplify equation (16). For example, Mellman (1980) utilized a modified first-motion approximation, such that rapidly varying terms in  $R_i(p)$  are evaluated only at the geometric ray parameter. Similarly, Brown (1982), Shaw (1983) and Chapman and Orcutt (1985) invoke the WKBJ approximation, but this breaks down in the presence of large velocity gradients or where discontinuities are encountered near the turning depth. For the current application, the logic required to evaluate the validity of these approximations for each ray would outweigh the effort at computing the response itself. We have therefore opted to calculate the

partial derivatives numerically. For simpler problems, this computation would certainly be quite inefficient. However, given the complexity of the near-field wave propagation problem, the computational cost is offset by the improved accuracy of the current approach. For a particular residual, say  $e_i$ , and parameter, say  $p_j$ , the numerical partial derivative is computed by, rather than (15),

$$\frac{\partial e_i}{\partial p_j} = \frac{e_i(p_j + \Delta p_j) - e_i(p_j)}{\Delta p_j} \quad (17)$$

where  $\Delta p_j$  is the perturbation to the starting model parameter,  $p_j$ . The partials  $\partial a_i / \partial p_j$  and  $\partial t_i / \partial p_j$  have similar form.

Now that we have defined the form of the residual and parameter vectors and the partial derivative matrix, we may redefine the matrices in (6) as

$$\begin{aligned} \underline{A} &= \underline{S}^{-\frac{1}{2}} \underline{J} \\ \underline{P} &= \underline{W}^{-\frac{1}{2}} \underline{P} \\ \underline{A} &= \underline{S}^{-\frac{1}{2}} \underline{A} \underline{W}^{\frac{1}{2}} \end{aligned} \quad (18)$$

in which  $\underline{S}$  is the covariance matrix of the residuals and  $\underline{W}$  is a weighting matrix of the parameter changes. For simplicity, we assume that errors are uncorrelated, so  $\underline{S}$  is diagonal. If an estimate of the residual variance is known (e.g., timing errors), that value is used in  $\underline{S}$ . Otherwise, the residual variances are inversely related to the relative confidence in the residuals. The basic purpose of the diagonal matrix  $\underline{W}$  is to counter the dimensionality of the parameterization of source and structure. Obviously velocity gradient (with values on the order of 1 km/s/km) and  $\Psi_z$  (values of  $10^{15}$  cm<sup>3</sup>) should not

be weighted equally. Due to nonlinearity, the weighting factors are also used to stabilize the parameter changes. For example, if a parameter changes to an unreasonable value or oscillates about some value, the weight of that parameter is decreased and the inversion is repeated. This introduces a certain degree of uncertainty in interpreting the variances of the parameters, since these now include the effects of the somewhat arbitrary weights necessary due to nonlinearity. Although convergence criteria may be utilized to determine when to stop an inversion, we have not implemented such an approach, but simply allow additional sets of five iterations until convergence is deemed complete or unattainable. Finally, following Jackson (1979), *a priori* constraints may be placed on the parameter changes so that, for example, the velocity cannot be negative, or so that source parameters must fall within a range of reasonable values.

The weighted version of (6) may be solved by a linearized generalized inverse (Wiggins, 1972) such that

$$p = U \Lambda^{-1} U^T J \quad (19)$$

in which  $\underline{\Lambda}$  is the diagonal matrix of non-zero singular values of  $\underline{A}$ ,  $\underline{V}$  is the corresponding matrix of eigenvectors which spans the parameter space, and  $\underline{U}$  is the matrix of eigenvectors that spans the residual space. Since the problem is non-linear, the inversion is iterative and minimizes both the least-squares error,  $|\underline{A} \underline{p} - \underline{\Delta}|^2$ , and the length of the parameter vector,  $|\underline{p}|^2$ . Since small singular values result in large parameter variances, an a priori cut-off is specified, below which the singular value is assumed to be zero, and the dimension of the parameter space is truncated. The variances of the parameters are given by

$$\sigma_i^2 = \sum_{j=1}^K \frac{1}{\lambda_j^2} \quad (20)$$

and include the effects of the parameter weighting matrix. The parameter trade-offs that result from singular value truncation may be determined by an inspection of the parameter resolution matrix,

$$\underline{R} = \underline{L} \underline{L}^T \quad (21)$$

which reduces to the identity matrix in the case of perfect resolution. If during test inversions, the parameter resolution is deemed unacceptable, adjustments may be made in the parameter weights or the singular value cut-off, and the inversion may be repeated. The importance of particular observations or residuals in the inversion may be determined from the information density matrix,

$$\underline{S} = \underline{U} \underline{U}^T \quad (22)$$

or its diagonal, the data importance vector. This may indicate, for example, that the new parameters are most sensitive to the absolute amplitude residual at nearer receivers, and to the absolute time residual at more distant receivers. It also illustrates the importance of the parameter smoothing constraint via the Lagrange multipliers. Thus the data importance vector from test inversions may suggest modifications to the observation weights or to the Lagrange multiplier.

One distinct disadvantage of our implementation of the jumping method for the parameters rather than the usual generalized inverse for the parameter changes is in the treatment of parameters when eigenvalues are truncated. In

the generalized inverse. if an eigenvalue is truncated, the contribution to the parameter changes due to that eigenvalue is zero. Thus, if the eigenvector corresponding to a truncated eigenvalue is in the direction of a particular parameter change, that parameter change is set to zero and the parameter is unchanged in that iteration. In the jumping method, this situation would result in the new parameter value being set to zero. This is obviously undesirable for parameters such as  $\Psi_0$ , K and the velocity at the top of a layer.

In general, the new parameter value at a given iteration is a linear combination of contributions from each of the eigenvalues not truncated during that iteration. The extent to which the new parameter results from resolved eigenvalues is therefore given by the total of the lengths of the resolved eigenvectors in the direction of that parameter. That length is the square root of the diagonal of the resolution matrix corresponding to the parameter. To avoid the undesirable zeroing of parameters described above, we have implemented a smoothing procedure implemented at the end of each iteration. If the value of a parameter at the start of an iteration is given by  $p_{oi}$  and the new parameter value at the end of that iteration is  $p_i$ , the smoothed parameter value is given by

$$p_i^{(s)} = \sqrt{R_{ii}} p_i + \sqrt{1 - R_{ii}} p_{oi} \quad (23)$$

where  $R_{ii}$  is the value of the diagonal of the parameter resolution matrix for parameter  $i$ . This is obviously a nonlinear constraint imposed upon the inversion, and has the effect of somewhat duplicating the parameter smoothing

with the Lagrange multipliers. As such it slows convergence to a solution, but has the desired effect that the parameters of that solution retain reasonable values.

## TEST OF THE INVERSION METHOD

A number of tests of the generalized inverse for structure parameters or the simultaneous inverse for structure and source parameters were presented and discussed in Barker, et al. (1985b, 1986). In particular, those reports illustrated the shapes of the residual functions in the parameter space (i.e., the locations of local and global residual minima), and discussed the parameter trade-offs in this non-linear problem. Since we have now implemented the jumping method of inversion (Shaw and Orcutt, 1985), we have repeated one of the test inversions of Barker, et al. (1986) using this technique.

A synthetic data set was generated using a Helmberger-Hadley (1981) RDP and a two-layer gradient structure. The velocity structure was based on the model Hartzell, et al. (1983) obtained for Pahute Mesa, and consists of a surface velocity of 2.5 km/s and gradient of 0.83 km/s/km in the top layer. The second layer is separated from the first by a second-order discontinuity at a depth of 3.0 km and has a gradient of 0.20 km/s/km below that. For the source function, we set  $\Psi_0 = 1.0 \times 10^{10} \text{ cm}^3$ ,  $k=7.0 \text{ s}^{-1}$  and  $B=1$ . Vertical component velocity synthetics were computed for a source at 1.0 km depth and for ranges from 2 to 12 km. In Test # 4 of Barker, et al. (1986), this data set was first inverted for the parameters of the source and of the upper layer. Synthetic data at greater ranges were then added in order to resolve the lower layer parameters.

For the current test, we apply the jumping method inversion to the original data set and solve for the parameters of both layers as well as the

source. There are six parameters in the inversion:  $\Psi_0$ ,  $K$ , the upper layer gradient, the velocity at the surface, the lower layer gradient, and the depth to the top of the lower layer. The parameter weighting matrix is  $\text{diag}(1.0, 1.0, 0.1, 0.1, 0.1, 1.0)$  for these parameters, respectively. The covariance matrix of the observations is specified as  $\text{diag}(0.1, 1.0, 0.01)$  for the waveform, amplitude and time residuals, respectively, at each range. The Lagrange multiplier for parameter smoothing was set to 1.0, and the eigenvalue truncation parameter was chosen to allow full resolution. Since no eigenvalues are truncated, the solution smoothing applied at the end of each iteration has no effect for this test. An arbitrary starting model was specified and five iterations were performed. The resulting parameters and their standard errors (square root of the variance) are listed in Table 5 for each iteration. A comparison of the synthetic waveforms for each iteration with the synthetic data set is shown in Figure 7. In the figure, the data and synthetics are plotted on the same scales, the peak absolute amplitude is written to the right of each trace, and the inversion time window is indicated by arrows. The data importance vectors, including the relative importance of the parameter smoothing equations, are plotted in Figure 8. The parameter resolution matrix for each iteration is simply the identity matrix, and is not plotted.

It is clear from an inspection of the waveforms (Figure 7) that the amplitude and timing errors of the starting model are almost entirely corrected in the first iteration. The following iterations simply fine tune the model for amplitudes and times, while attempting to fit the details of the waveforms. This may be seen in the data importance vectors (Figure 8). During the first iteration, the amplitude and time residuals are most



Table 5 - Test Inversion Results

Iteration	$\psi_z$ ( $\times 10^{12}$ cm <sup>3</sup> )	k (s <sup>-1</sup> )	$\partial\alpha_1/\partial z$ (km/s/km)	$\alpha_1$ (km/s)	$\partial\alpha_2/\partial z$ (km/s/km)	$z_2$ (km)	RMS fit	LSE
Start	2.00	9.00	0.50	2.00	0.50	2.00	1.089	
1	0.37 (.42)	8.10 (.89)	0.54 (.07)	2.54 (.12)	0.99 (.25)	1.35 (.28)	.330	30.0
2	0.71 (.31)	7.89 (.89)	0.63 (.25)	2.60 (.28)	0.96 (.28)	1.42 (.57)	.121	1.74
3	0.80 (.34)	7.57 (.88)	0.68 (.29)	2.57 (.24)	0.98 (.40)	1.42 (.35)	.152	0.90
4	0.78 (.38)	7.53 (.94)	0.76 (.23)	2.52 (.18)	0.98 (.27)	1.41 (.36)	.110	0.39
5	0.84 (.36)	7.52 (.94)	0.77 (.34)	2.51 (.26)	0.94 (.34)	1.36 (.40)	.068	0.37
"Data"	1.00	7.00	0.83	2.50	0.20	3.00		

LSE is the least-squares error.

Numbers in parentheses are the standard errors of the parameters.

## TEST Inversion Results

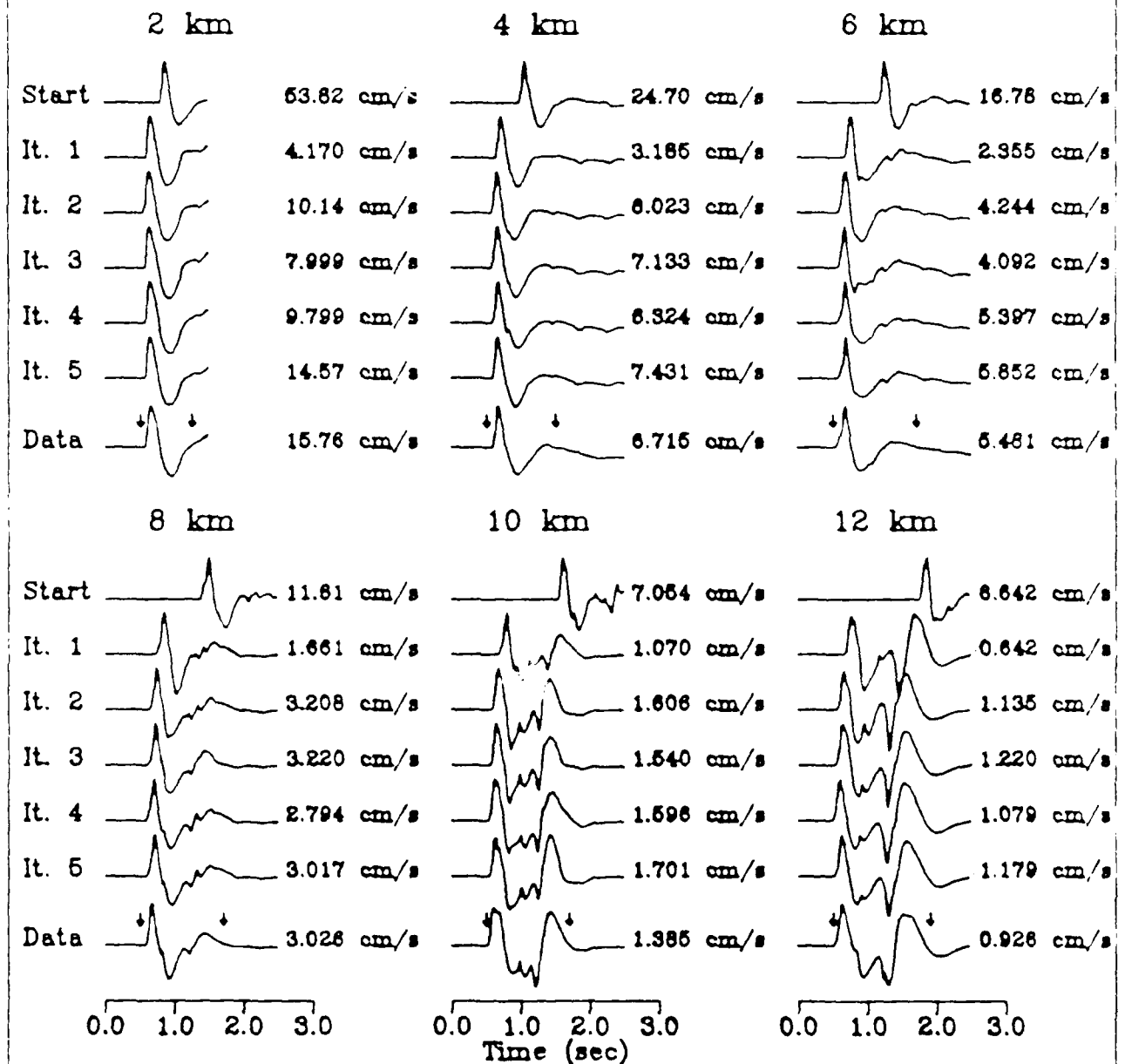


Figure 7. Results of the test inversion for velocity structure. Synthetic seismograms are shown for the starting model and five iterations at each receiver. The data seismograms (also synthetic) are plotted below. Arrows above the data waveforms indicate the inversion time windows and numbers to the right are the peak trace amplitudes.

## TEST Data Importance Vectors

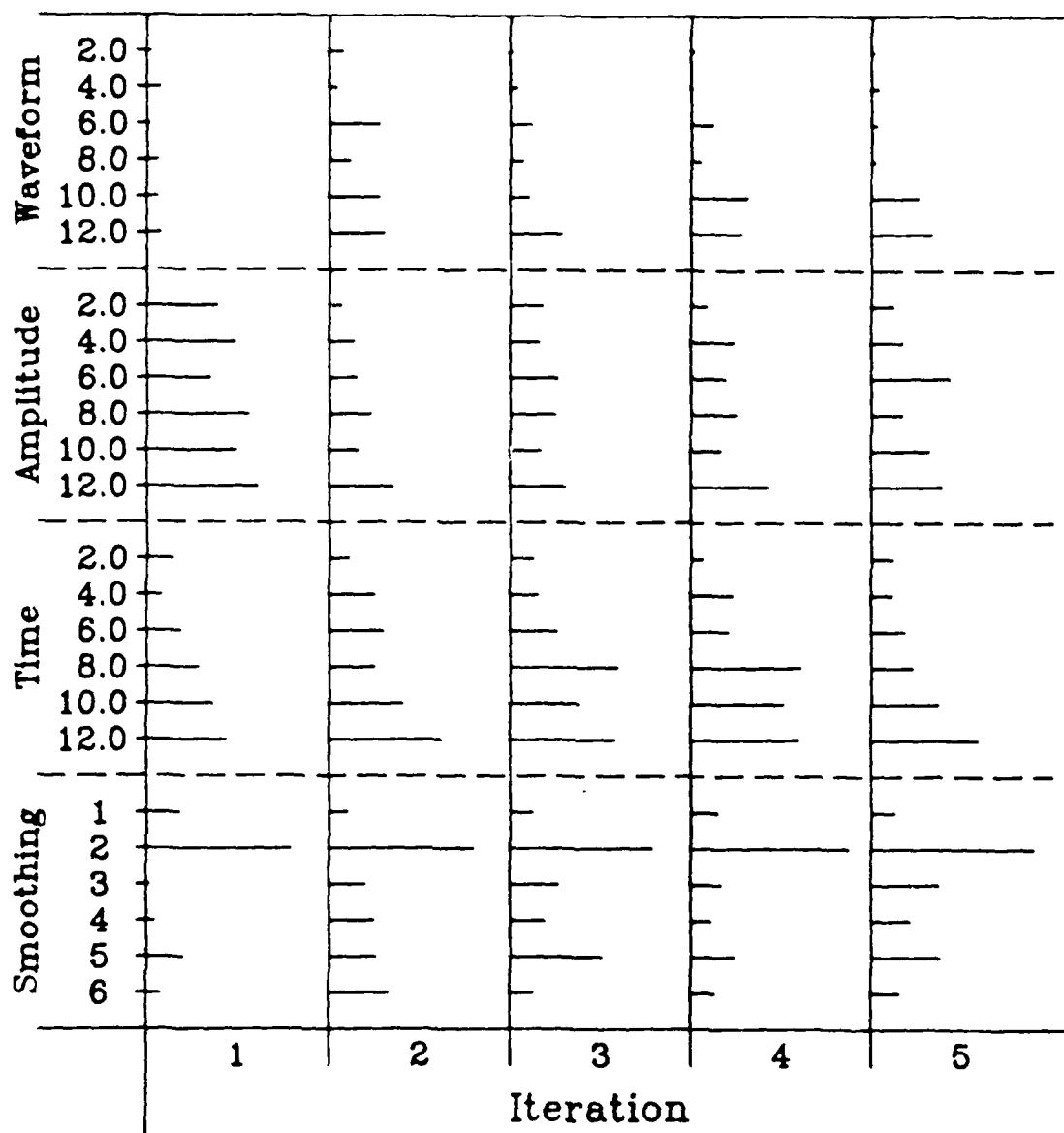


Figure 8. The data importance vectors for the test inversion. Shown are the diagonals of the information density matrix for each iteration including the relative importance of the parameter smoothing equations. The length of the ticks indicate the relative importance of the residuals at each receiver in the determination of the solution.

important in constraining the solution. In the second iteration, the importance of the waveform residuals increases while that of the amplitude residuals decreases. In the third through fifth iterations, the more distant waveforms are important as deeper structural parameters are adjusted. The importance of the time residuals remains high for all iterations, constraining the parameters to remain near the correct solution. The parameter smoothing via the Lagrange multiplier has its largest effect in constraining the second parameter,  $K$ . This is because although we have specified full resolution, the value of  $K$  trades off with  $\Psi_0$  and may vary substantially. The parameter smoothing prevents radical changes in  $K$ , allowing uniform convergence.

The convergence of the inversion parameters listed in Table 5 to the correct model parameters (listed at the bottom of the table) indicates the relative resolution of the parameters. The velocity at the surface has nearly reached its correct value after only one iteration. This is because, for the ranges considered, the time residual is most sensitive to this parameter. The gradient of the top layer converges more slowly.  $\Psi_0$  is reduced in the first iteration to smaller than the correct value, rebounds in the second iteration, then converges to a value somewhat below the correct value.  $K$  decreases monotonically due to the parameter smoothing constraint, but because of its trade-off with  $\Psi_0$ , converges to a value somewhat too high. For these ranges, the residuals are not very sensitive to the gradient in the lower layer. In fact, it appears that the lower gradient and depth parameters are given values that compensate for the upper gradient being slightly too low. As in Barker et al. (1986), the inclusion of data from greater ranges would improve the resolution of the lower layer parameters. Given the inherent trade-offs

between parameters and the limited range coverage of the synthetic data set. it appears that the jumping inversion method performs as well or better than the standard generalized inverse of Barker, et al. (1986).

## INVERSION RESULTS

### BOXCAR

We begin the inversions of observed data with the Pahute Mesa event, BOXCAR (4/26/68, 1300 kt announced, 1.160 km depth). Hartzell, et al. (1983) developed their Pahute Mesa structure model primarily by modeling the waveforms of receivers S-24 and S-34 from BOXCAR, although travel times from several other events were quite well predicted. We will use an approximation of the Hartzell, et al. (1983) model as our starting model. In addition, however, we wish to include a high velocity gradient above the water table as suggested by the velocity log published in Stump and Johnson (1984). This dry tuff layer is adequately approximated by a gradient of 0.92 km/s/km starting from a surface velocity of 2.4 km/s and reaching the water table at a depth of 0.65 km. These parameters are held fixed through the inversion. In the inversion, we allow only second-order discontinuities below the water table, so the free parameters consist of  $\Psi_0$ , K, the gradient in the second layer, the gradient in the third layer, and the depth to the top of the third layer. The parameter weighting matrix is specified as diag(10., 10., 1.0, 0.1, 0.1) for these parameters, respectively. The starting model source parameters are the forward modeling results listed in Table 4.

The stations used in the inversion are listed in Table 2, and include a broad distribution of ranges. The closest receivers (S-12 at 3.81 km and S-16 at 4.87 km) are only marginally outside the spall zone and appear to include arrivals attributable to spall opening or slap-down. Since these effects will not be included in our modeling, we must increase the covariance of the waveform residuals, effectively down-weighting the importance of fitting the

waveform, at these receivers. The covariance matrix is  $\text{diag}(10.0, 10.0, 0.01)$  for waveform, amplitude and travel time, respectively. Similarly, the farthest station (S-74 at 22.47 km) is located outside the Silent Canyon Caldera of Pahute Mesa, and we could expect the plane-layered structure approximation to break down for this receiver. We have therefore increased the covariance of the waveform and travel-time residuals at this receiver. The resulting covariance is  $\text{diag}(10.0, 10.0, 10.0)$ . This leaves two receivers (S-24 at 7.27 km and S-34 at 10.37 km) with reasonable covariance in waveform and amplitude residuals. Unfortunately, preliminary inversions indicate that these stations have unmodeled travel-time residuals which may result from topography or laterally varying near-surface velocities. Accounting for timing errors, the covariance for these receivers is  $\text{diag}(0.1, 0.1, 1.0)$ . Five iterations were allowed, with the Lagrange multiplier specified as 1.0 and the eigenvalue cutoff set for full resolution.

The inversion results are listed in Table 6 and the waveforms for the final inversion model are plotted in Figure 9. Also shown are waveforms that resulted from the forward modeling study of Barker, et al. (1985a) using the structure model in Table 3 and the source parameters in Table 4. For each station, the waveforms are plotted on the same time and amplitude scales, and the peak absolute amplitude is written to the right of each trace. Arrows above the observed records indicate the inversion time window used. In both the forward and inverse synthetics, the waveforms at S-12 and S-16 are simple and impulsive, while the observed waveforms are broad, and include significant late arrivals. These may be attributed to unmodeled processes of spall and slap-down. The first peak at S-24 and S-34 includes the constructive interference of upgoing and diving rays, while the trough includes the

Table 6 - BOXCAR Inversion Results

Iteration	$\Psi_{\infty}$ ( $\times 10^{10}$ cm <sup>3</sup> )	k (s <sup>-1</sup> )	$\partial\alpha_2/\partial z$ (km/s/km)	$\partial\alpha_3/\partial z$ (km/s/km)	$z_3$ (km)	RMS fit	LSE
Start	12.0	6.50	0.83	0.20	3.00	.247	
1	12.3 (1.7)	6.56 (1.16)	0.80 (.26)	0.21 (.36)	2.99 (.55)	.299	0.90
2	12.6 (1.7)	6.62 (1.13)	0.83 (.29)	0.18 (.29)	2.99 (.56)	.253	0.98
3	12.8 (1.7)	6.62 (1.10)	0.82 (.34)	0.18 (.37)	2.99 (.56)	.286	0.91
4	13.0 (1.7)	6.81 (1.18)	0.77 (.27)	0.15 (.30)	2.99 (.55)	.290	0.84
5	13.2 (1.7)	6.53 (1.06)	0.81 (.25)	0.14 (.51)	2.99 (.56)	.237	1.00

LSE is the least-squares error.

Numbers in parentheses are the standard errors of the parameters.

Fixed structure parameters include  $\alpha_1=2.4$  km/s,  $\partial\alpha_1=0.92$  km/s/km and  $z_2=0.65$  km.



## Modeling Results for BOXCAR

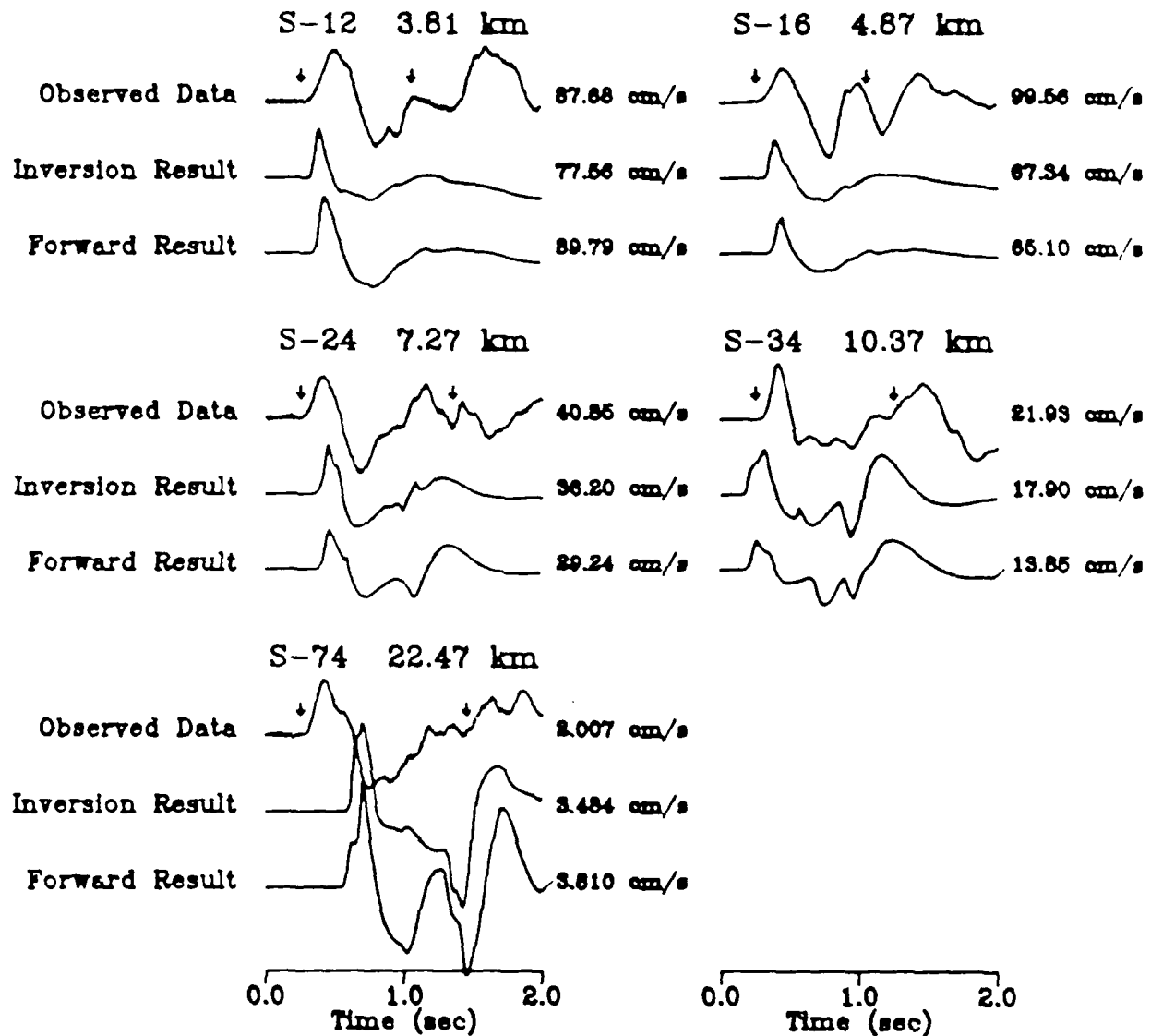


Figure 9. Inversion results for Pahute Mesa event BOXCAR. Shown are the observed records (top), the results from the numerical inversion (center) and from forward modeling (bottom). The peak trace amplitude is shown to the right and the inversion time window is denoted by arrows.

interaction of the surface reflection phases. Although the synthetic arrival times at these stations is somewhat off (S-24 is late by 0.02 s while S-34 is early by 0.09 s), the details of the waveforms are quite well modeled both in the inversion and in the forward modeling, indicating that the velocity gradient near the source depth is well determined. Since S-74 is outside of Pahute Mesa, we expect the arrival time to be poorly modeled. The amplitudes of the synthetics are also somewhat too large, but the general shape of the waveforms is adequately modeled within the inversion time window.

Table 6 indicates that in the inversion, the model parameters vary only slightly from the starting model.  $K$  increases, but then returns to its starting value.  $\Psi_0$  increases slowly. The second layer gradient varies about its starting value, while the third layer gradient decreases slowly and the depth to the third layer remains constant. This is reflected in the data importance vectors (Figure 10). Throughout the inversion the amplitude residuals (particularly at the more distant stations) are most important in determining the solution, while the parameter smoothing constraint on  $\Psi_0$  and the third layer depth force these parameters to vary slowly. Although full resolution was specified, the problem is non-linear and the parameters trade off. The parameter smoothing inhibits the parameters from assuming unrealistic values. A side effect of full resolution is that the parameter variances can be large. Shown in parentheses in Table 6 are the standard errors (square root of the variances) for the parameters. Although the errors are large (particularly for the third layer gradient), the solution is convergent.

# BOXCAR Data Importance Vectors

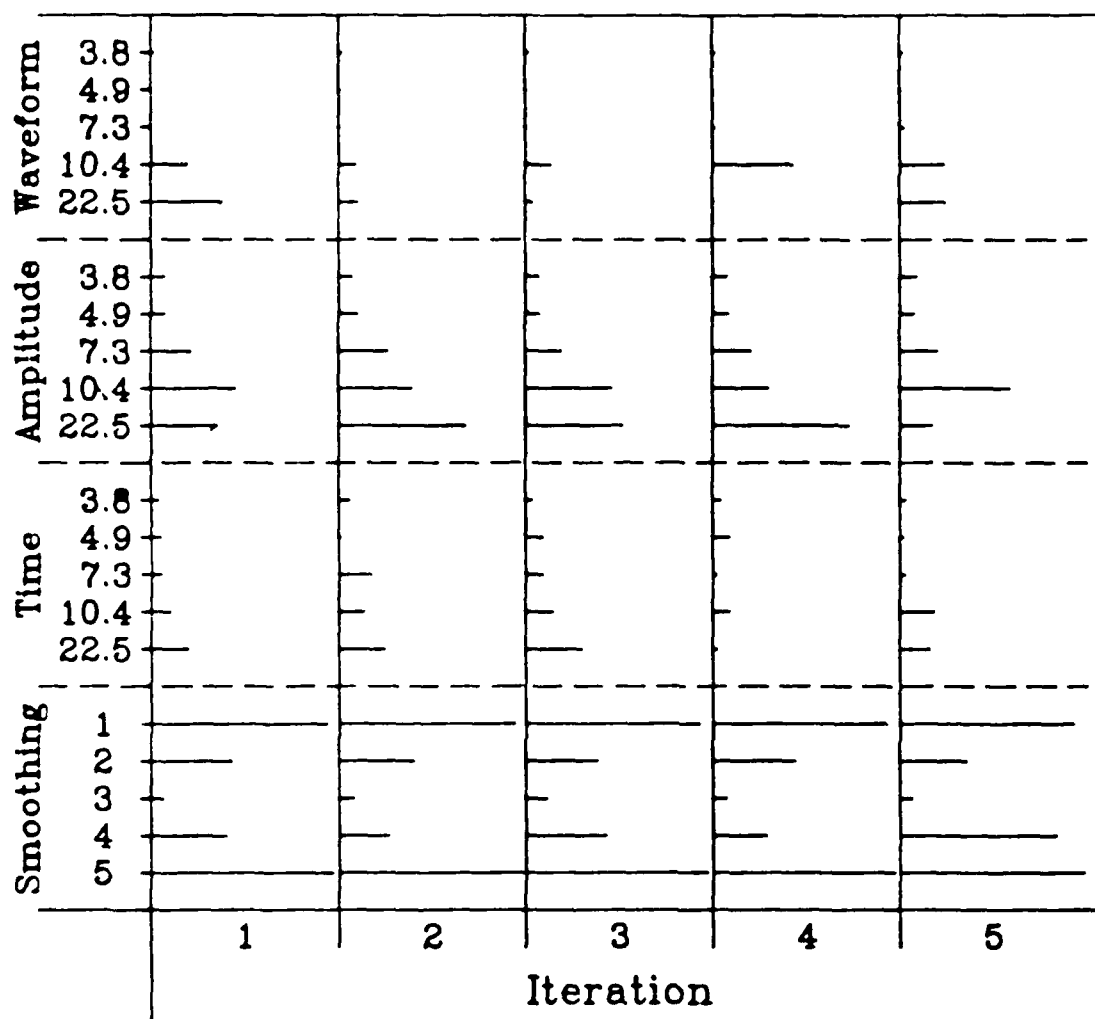


Figure 10. Parameter resolution matrices for each iteration of the BOXCAR inversion. Plotted from top to bottom are the rows of the matrices corresponding to the source parameters,  $v_s$  and  $k$ , and the structure parameters, upper gradient, lower gradient and interface depth. For perfect resolution, the resolution matrix would be the identity matrix.

It should, perhaps, be no surprise that the inversion results do not depart significantly from the starting model. The starting structure model is based on the velocity structure determined by Hartzell, et al. (1983) largely from modeling the details of the S-24 and S-34 records from BOXCAR. This has been shown in Figures 3 and 4, and is reinforced by the agreement between forward and inverse synthetics in Figure 9. The conclusion is that this structure model is very good for BOXCAR. The starting model source parameters were determined by forward modeling using this structure model. One problem with the forward modeling study was the need to assume the same structure model for all Pahute Mesa events. By performing the simultaneous inversion on the waveforms of these events, we will determine if significant modifications to the structure model are demanded for slightly different locations within Pahute Mesa. By comparing the source parameters from forward and inverse modeling, we may determine to what extent these structure variations effect our estimates of source parameters.

## MAST

In inverting the vertical velocity observations for the event MAST (6/19/75, 520 kt estimated, 0.912 km depth), we use a starting model with the same structure parameters as in the BOXCAR inversion and source parameters determined by forward modeling of MAST (Table 4). Three observed records are available outside the spill zone (Table 2). The covariance matrix of the observations is specified as  $\text{diag}(0.01, 0.1, 0.01)$  for waveform, amplitude and time residuals, respectively, except that because of noise at the most distant receiver, its waveform residual variance is set to 0.1. The parameter weighting matrix is  $\text{diag}(1.0, 1.0, 0.1, 0.1, 0.1)$  for  $\Psi_0$ ,  $K$ , the gradients in the second and third layers, and the depth to the top of the third layer, respectively. The Lagrange multiplier is 1.0 and the resolution is such that three or four of the five parameters are resolved each iteration.

The results of the inversion are listed in Table 7. The synthetic waveforms from the fourth iteration are plotted in Figure 11, along with the observed records and the synthetics from the forward modeling study of Barker, et al. (1985a). Arrows above the observed data record indicate the inversion time window, and the peak absolute amplitude of each trace is written to the right. The parameter resolution matrices for each iteration are plotted in Figure 12. Because some eigenvalues are truncated, the gradient in the third layer is not resolved and other parameters trade off with each other (in the case of perfect resolution, the parameter resolution matrix would be the identity matrix).  $K$  and the second layer gradient are well resolved.  $\Psi_0$  is initially well resolved, but begins to trade off with the third layer parameters beginning with the third iteration. The inversion reaches a

Table 7 - MAST Inversion Results

Iteration	$\Psi_e$ ( $\times 10^{10}$ cm <sup>3</sup> )	k (s <sup>-1</sup> )	$\partial\alpha_2/\partial z$ (km/s/km)	$\partial\alpha_1/\partial z$ (km/s/km)	$z_2$ (km)	RMS fit	LSE
Start	4.70	7.50	0.83	0.20	3.00	.149	
1	5.44 (.78)	7.74 (.78)	0.96 (.33)	0.20 (.01)	2.64 (.05)	.197	78.5
2	5.35 (.79)	6.65 (.70)	1.05 (.32)	0.20 (.04)	2.66 (.49)	.106	7.26
3	7.50 (.76)	5.43 (.66)	1.46 (.24)	0.20 (.07)	1.89 (.22)	.105	46.5
4	6.22 (.78)	6.39 (.59)	1.58 (.36)	0.66 (.30)	1.85 (.39)	.095	11.0
5	5.84 (.74)	6.47 (.69)	1.66 (.28)	0.81 (.32)	1.81 (.40)	.112	2.25

LSE is the least-squares error.

Numbers in parentheses are the standard errors of the parameters.

Fixed structure parameters include  $\alpha_1=2.4$  km/s,  $\partial\alpha_1=0.92$  km/s/km and  $z_2=0.65$  km.

## Modeling Results for MAST

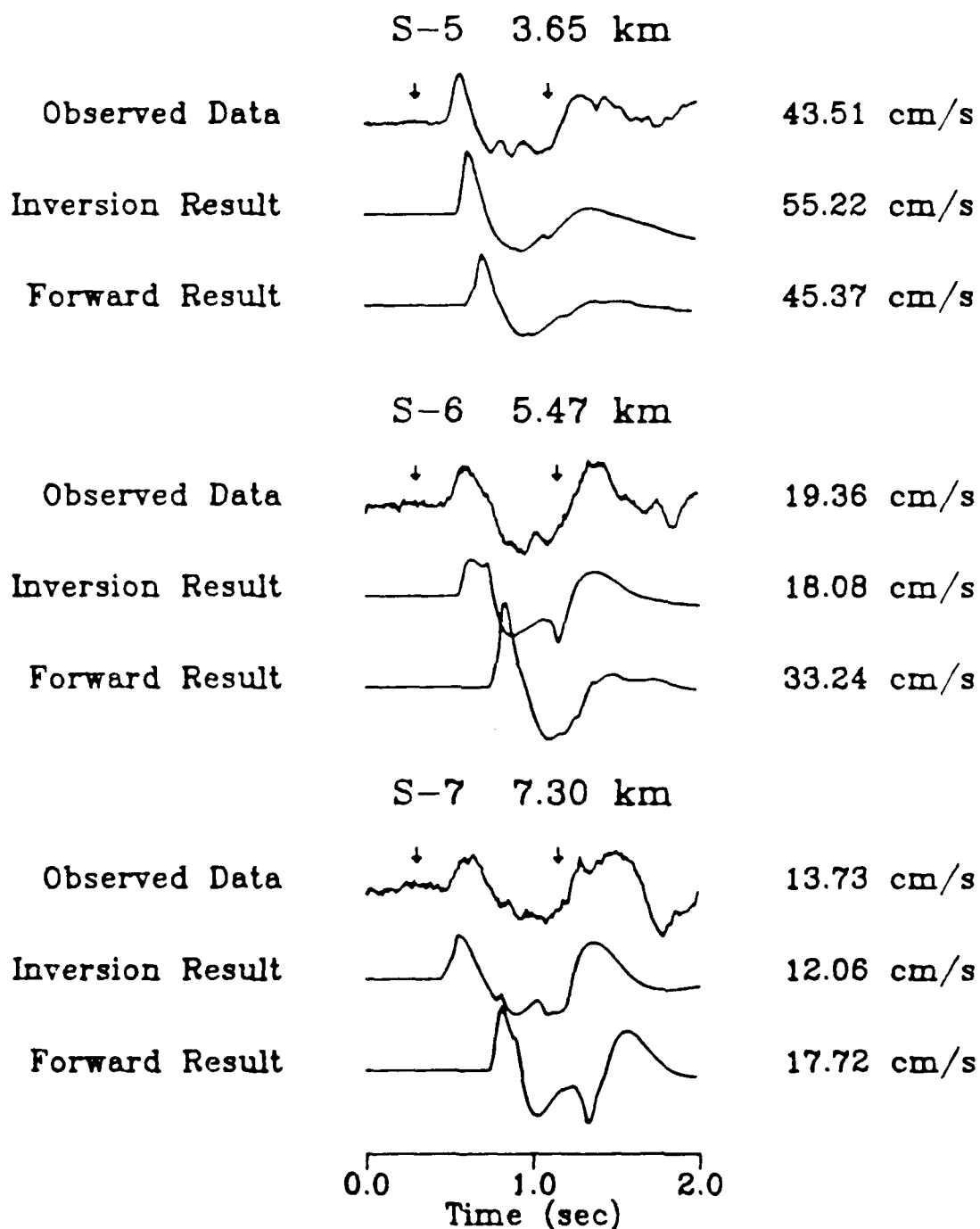


Figure 11 Inversion results for Pahute Mesa event MAST. Shown are the observed records (top), the results from the numerical inversion (center) and from forward modeling (bottom). The peak trace amplitude is shown to the right and the inversion time window is denoted by arrows.

## MAST Resolution Matrices

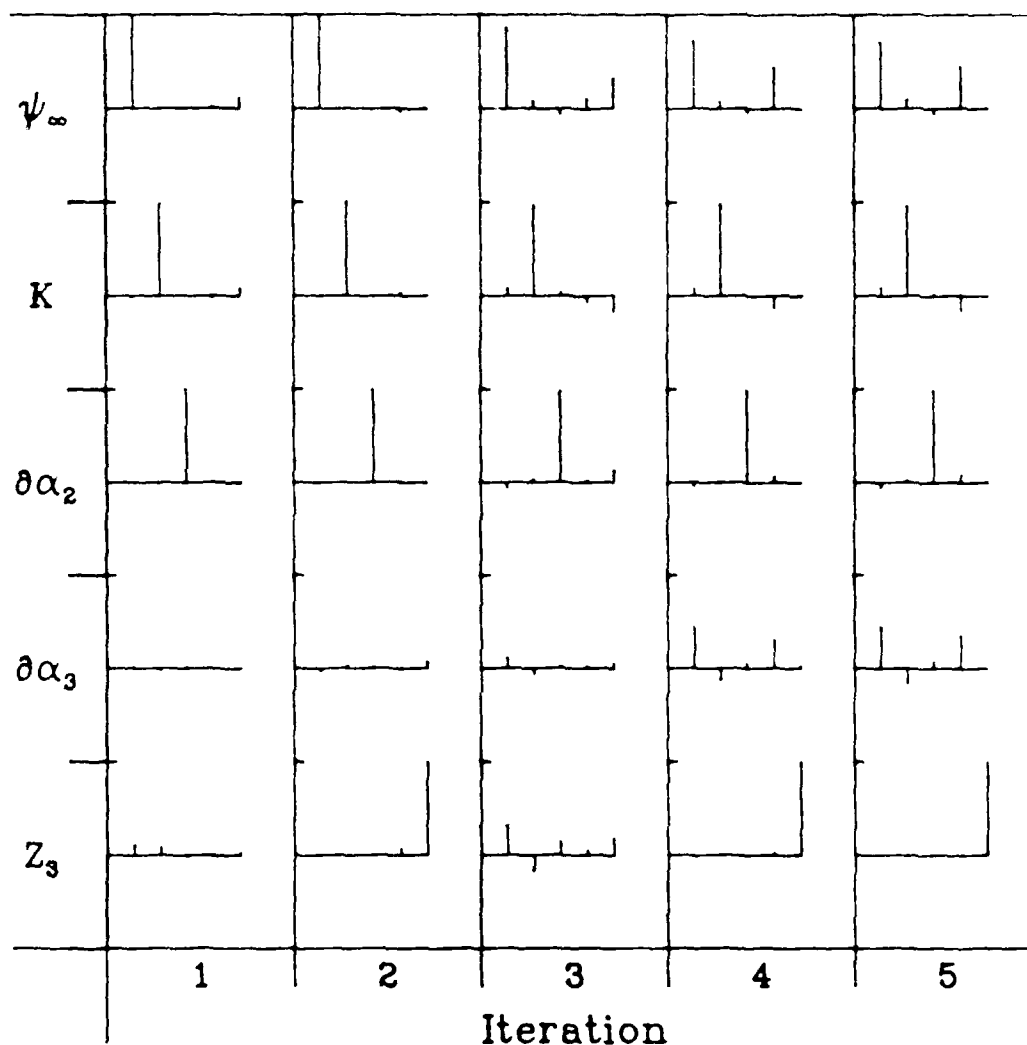


Figure 12. Parameter resolution matrices for each iteration of the MAST inversion. Plotted from top to bottom are the rows of the matrices corresponding to the source parameters,  $\psi$ , and  $k$ , and the structure parameters, upper gradient, lower gradient and interface depth. For perfect resolution, the resolution matrix would be the identity matrix.



minimum in RMS fit at the fourth iteration (the divergence at the fifth iteration is due primarily to the change in  $\Psi_0$ ), so the synthetics plotted in Figure 11 represent this solution. Presumably, if more iterations were allowed, the inversion would return toward these parameters. Because eigenvalue truncation was allowed, the standard errors in Table 7 are reasonably small. The parameter variance has improved at the expense of parameter resolution.

The first peak at S-5 is simple and is well modeled by both the forward and inverse models. The trough of this record, however, reflects the interference of the pP phase with the upgoing and diving P waves. The details of this interference are slightly better fit by the inversion waveform, but the first peak amplitude is better matched by the forward model. The features of the first peak at S-6 and S-7 are sensitive to the interference of upgoing and diving P, and are significantly better modeled by the inversion waveforms. Further, the details within the troughs for these stations, the amplitudes of the first peaks, and the travel times are all improved by the inversion. It would appear that the higher velocity gradient in the second layer resolved by the inversion is demanded by the data. This results in a source model in which  $\Psi_0$  is somewhat higher and  $K$  is somewhat lower than the forward modeling results of Barker, et al. (1985a).

## INLET

The same starting structure model is used to invert the observed vertical velocity waveforms for the INLET (11/20/75, 500 Kt estimated, 0.817km depth), and starting source parameters appropriate for this event are obtained from the forward modeling results (Table 4). Three observed records are available outside the spall zone (Table 2). Although the spall zone for INLET was quite limited, the record at 1.63 km may contain some unmodeled effects due to spall or slap-down, so its covariance matrix reflects uncertainties in waveform and amplitude and is specified as  $\text{diag}(10., 10., 0.01)$  for waveform, amplitude and time residuals, respectively. The covariance matrix of the other two observations is  $\text{diag}(0.1, 0.1, 0.01)$ . The parameter weighting matrix is  $\text{diag}(1.0, 1.0, 0.1, 0.1, 1.0)$  for  $\psi_0$ ,  $K$ , the gradients in the second and third layers, and the depth to the top of the third layer, respectively. The Lagrange multiplier is 1.0 and the resolution is such that three or four of the five parameters are resolved each iteration.

The results of the inversion are listed in Table 8. The synthetic waveforms are plotted in Figure 13, along with the observed records and the synthetics from the forward modeling study of Barker, et al. (1985a). Arrows above the observed data indicate the inversion time window, and the peak absolute amplitude of each trace is written to the right. The synthetic waveforms from forward and inverse modeling are quite similar in shape.

Table 8 - INLET Inversion Results

Iteration	$W_s$ ( $\times 10^{12}$ cm <sup>3</sup> )	k (s <sup>-1</sup> )	$Za_2/Zz$ (km/s/km)	$Za_3/Zz$ (km/s/km)	$z_3$ (km)	RMS fit	LSE
Start	3.20	8.00	0.83	0.20	3.00	.242	
1	4.05 (.84)	7.93 (.92)	0.88 (.31)	0.20 (.00)	2.61 (.11)	.164	13.8
2	4.30 (.87)	8.03 (.90)	0.91 (.28)	0.15 (.10)	2.37 (.95)	.149	1.44
3	4.15 (.69)	8.14 (.69)	0.89 (.33)	0.15 (.02)	2.12 (.59)	.151	1.19
4	4.40 (.84)	8.13 (.87)	0.86 (.40)	0.13 (.06)	2.18 (.86)	.140	1.18
5	4.48 (.80)	8.12 (.83)	0.83 (.31)	0.12 (.01)	1.88 (.08)	.135	5.27

LSE is the least-squares error.

Numbers in parentheses are the standard errors of the parameters.

Fixed structure parameters include  $a_1=2.4$  km/s,  $Za_1=0.92$  km/s/km and  $z_2=0.65$  km.

## Modeling Results for INLET

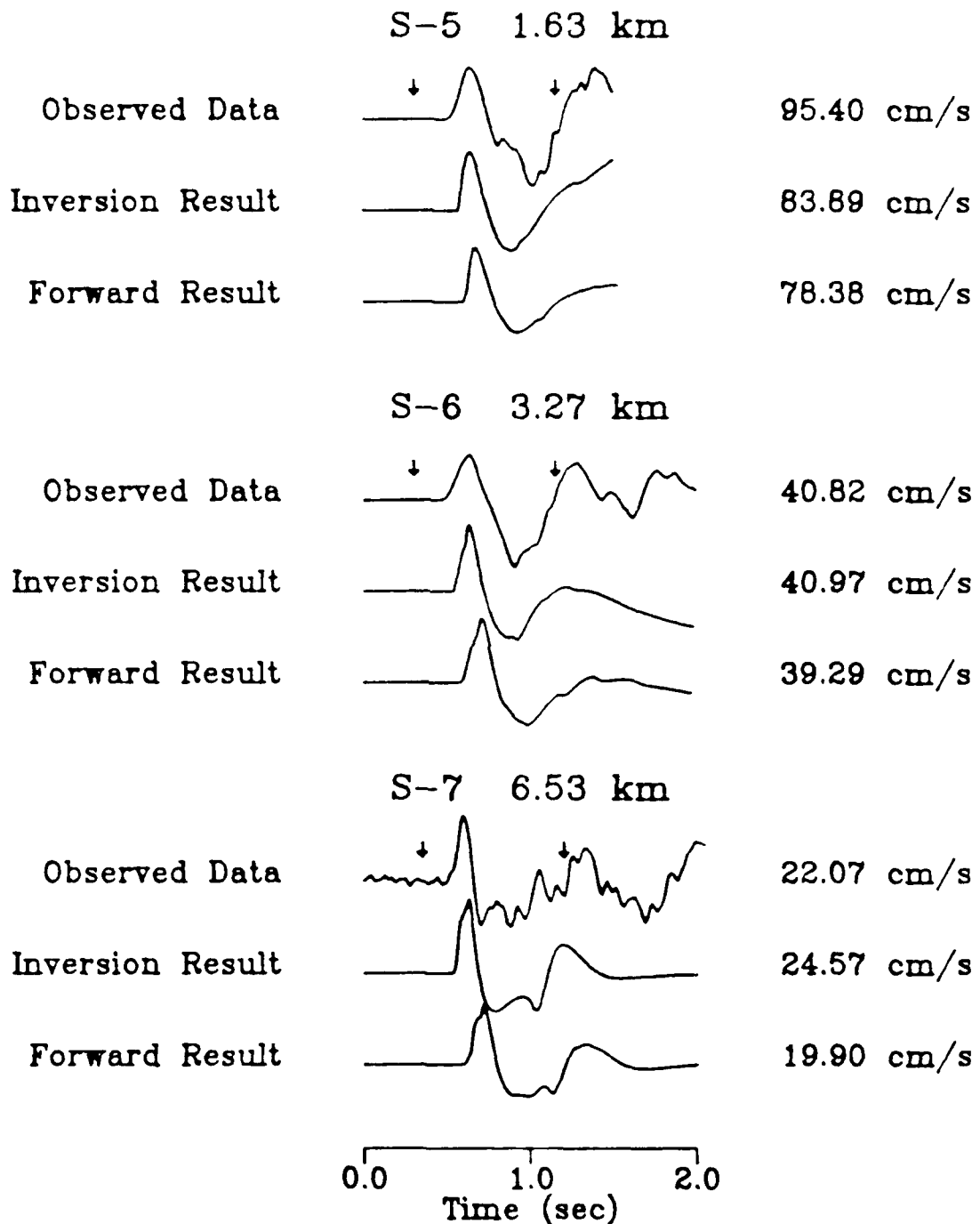


Figure 13. Inversion results for Pahute Mesa event INLET. Shown are the observed records (top), the results from the numerical inversion (center) and from forward modeling (bottom). The peak trace amplitude is shown to the right and the inversion time window is denoted by arrows.

although the absolute amplitudes and travel times are slightly improved by the inversion. The S-5 observed record contains late arrivals in the trough that are not modeled by either approach and may reflect spall processes. The observed first pulse at S-6 is significantly wider than either of the synthetics, although the pulsewidth at S-7 is well modeled and that at S-5 is nearly fit. Apparently, allowing the structure model to vary cannot improve the fit at S-6 while still fitting S-5 and S-7. The observed waveform at S-7 is rather noisy, but both the forward and inverse synthetics include the multiple arrivals apparent in the trough.

The parameter resolution matrix for INLET is plotted in Figure 14. The gradient in the third layer is never resolved. The slight variations in this parameter from the starting value (Table 8) are not resolved, but result from slight trade-offs with other parameters. The gradient in the second layer is well resolved in each iteration, but its value departs only slightly from that of the starting model. This indicates that the velocity gradient near the source depth from the Hartzell, et al. (1983) model is appropriate for INLET as well as for BOXCAR. In the inversion,  $K$  is well resolved, but remains close to the forward modeling value determined by Barker, et al. (1985a).  $\psi_\alpha$ , however, increases by about 35% over the forward modeling value. This results in the improved fits to the peak amplitudes.

## INLET Resolution Matrices

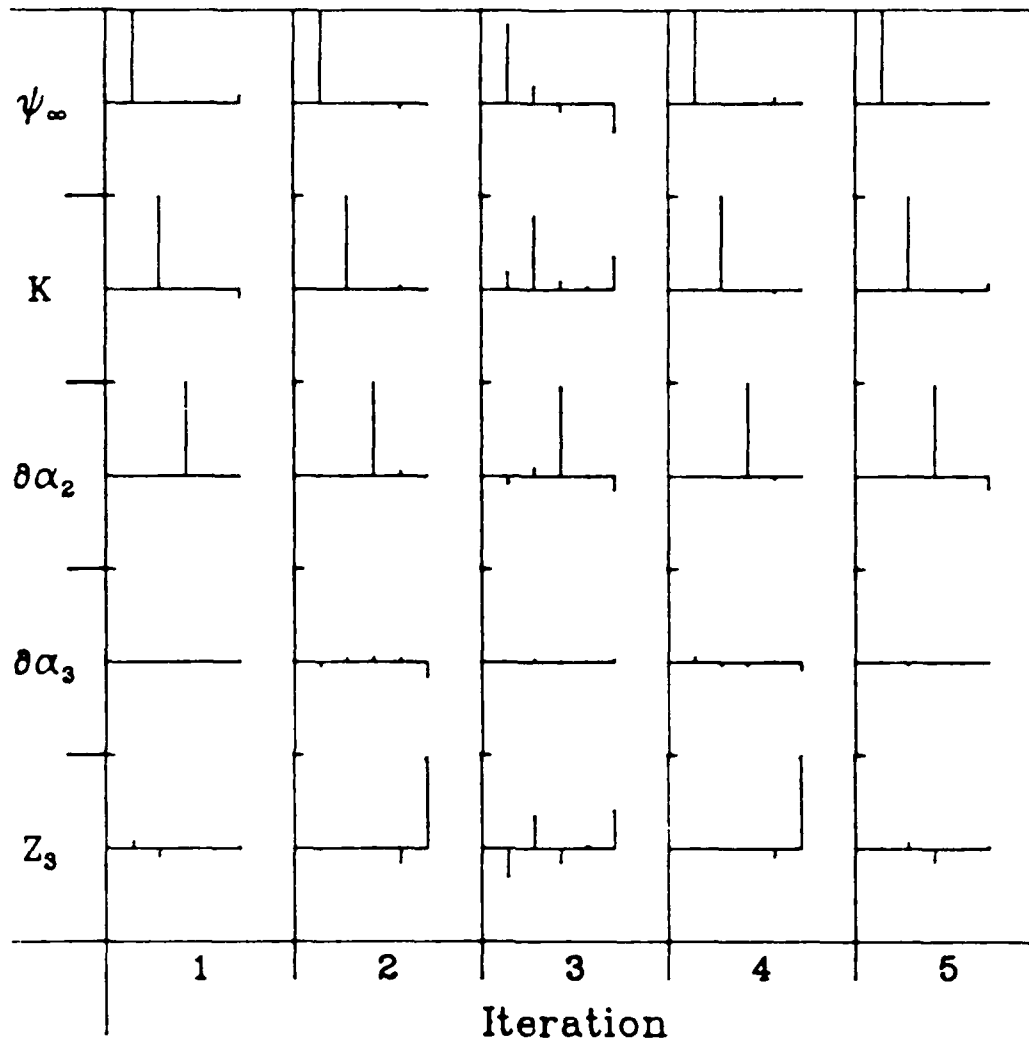


Figure 14. Parameter resolution matrices for each iteration of the INLET inversion. Plotted from top to bottom are the rows of the matrices corresponding to the source parameters,  $\psi_\infty$  and  $K$ , and the structure parameters, upper gradient, lower gradient and interface depth. For perfect resolution, the resolution matrix would be the identity matrix.

## SCOTCH

For the Pahute Mesa event SCOTCH (5/23/67, 155 Kt announced, 0.970 km depth), only two vertical velocity recordings are available outside the spill zone but within Pahute Mesa (see Table 2). Since the more distant of these is at a range of only 6.06 km, and from our experience in inverting MAST and INLET data, we suspect that the parameters of the lower structure will be poorly resolved. We therefore use the same starting model as in the other events, but raise the interface at the top of the third layer from 3.0 km to 1.5 km. In addition, we decrease the weights of these parameters. The starting source model is obtained from the forward modeling results (Table 4). The parameter weighting matrix is  $\text{diag}(1.0, 1.0, 0.1, 0.01, 0.01)$  for  $\Psi_0$ ,  $K$ , the gradients of the second and third layers, and the depth to the third layer, respectively. The covariance matrix of the observations is  $\text{diag}(0.01, 0.1, 0.001)$  for waveform, amplitude and time residuals, respectively, for both stations. The Lagrange multiplier is, once again, 1.0, and the resolution is such that four of the five eigenvalues are resolved.

The results of the inversion are listed in Table 9, and the final iteration synthetic seismograms are plotted in Figure 15 along with the observed waveforms and the synthetics from forward modeling. The parameter resolution matrices for each iteration are plotted in Figure 16. As expected, the gradient in the third layer is not resolved in the early iterations, but because the eigenvector corresponding to the truncated eigenvalue is not entirely in the direction of this parameter, its value is decreased in spite of the parameter smoothing. An interesting effect occurs at the fourth iteration, however. At this point, the depth to the top of the third layer

Table 9 - SCOTCH Inversion Results

Iteratio n	$\Psi_{\infty}$ ( $\times 10^{12}$ cm <sup>3</sup> )	k (s <sup>-1</sup> )	$\partial\alpha_2/\partial z$ (km/s/km )	$\partial\alpha_1/\partial z$ (km/s/km )	$z_3$ (km)	RMS fit	LSE
Start	1.30	12.00	0.83	0.20	1.50	.283	
1	1.82 (.42)	10.90 (.87)	0.54 (.28)	0.04 (.08)	1.42 (.30)	.241	59.3
2	1.11 (.45)	12.98 (.88)	0.65 (.21)	0.04 (.01)	1.24 (.04)	.348	182.
3	1.76 (.46)	12.52 (.88)	0.39 (.24)	0.09 (.05)	1.41 (.26)	.272	24.8
4	3.35 (.44)	11.55 (.87)	1.10 (.20)	0.63 (.28)	0.92 (.15)	.451	162.
5	2.02 (.62)	10.50 (.88)	1.00 (.12)	0.63 (.24)	0.76 (.28)	.229	20.0

LSE is the least-squares error.

Numbers in parentheses are the standard errors of the parameters.

Fixed structure parameters include  $\alpha_1=2.4$  km/s,  $\partial\alpha_1=0.92$  km/s/km and  $z_2=0.65$  km.



## Modeling Results for SCOTCH

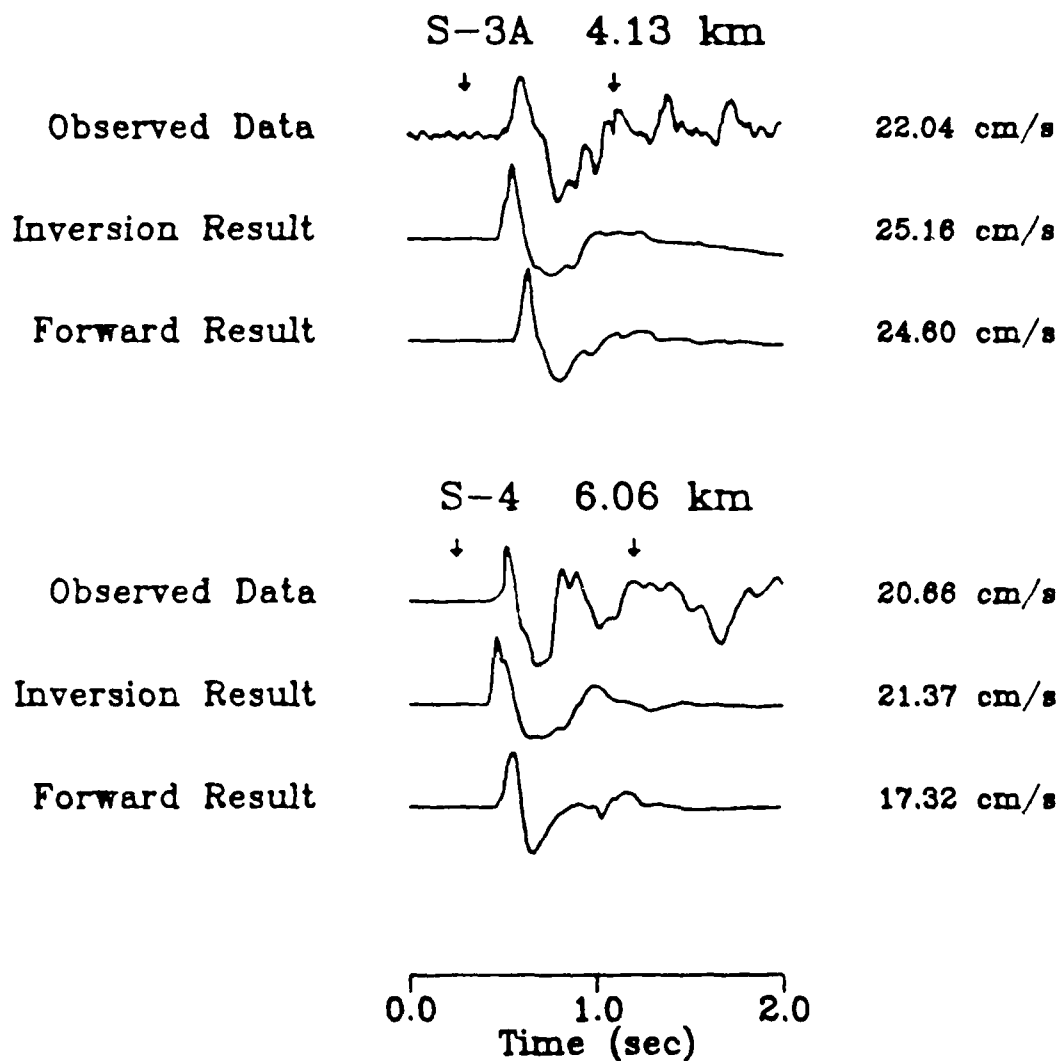


Figure 15. Inversion results for Pahute Mesa event SCOTCH. Shown are the observed records (top), the results from the numerical inversion (center) and from forward modeling (bottom). The peak trace amplitude is shown to the right and the inversion time window is denoted by arrows.

## SCOTCH Resolution Matrices

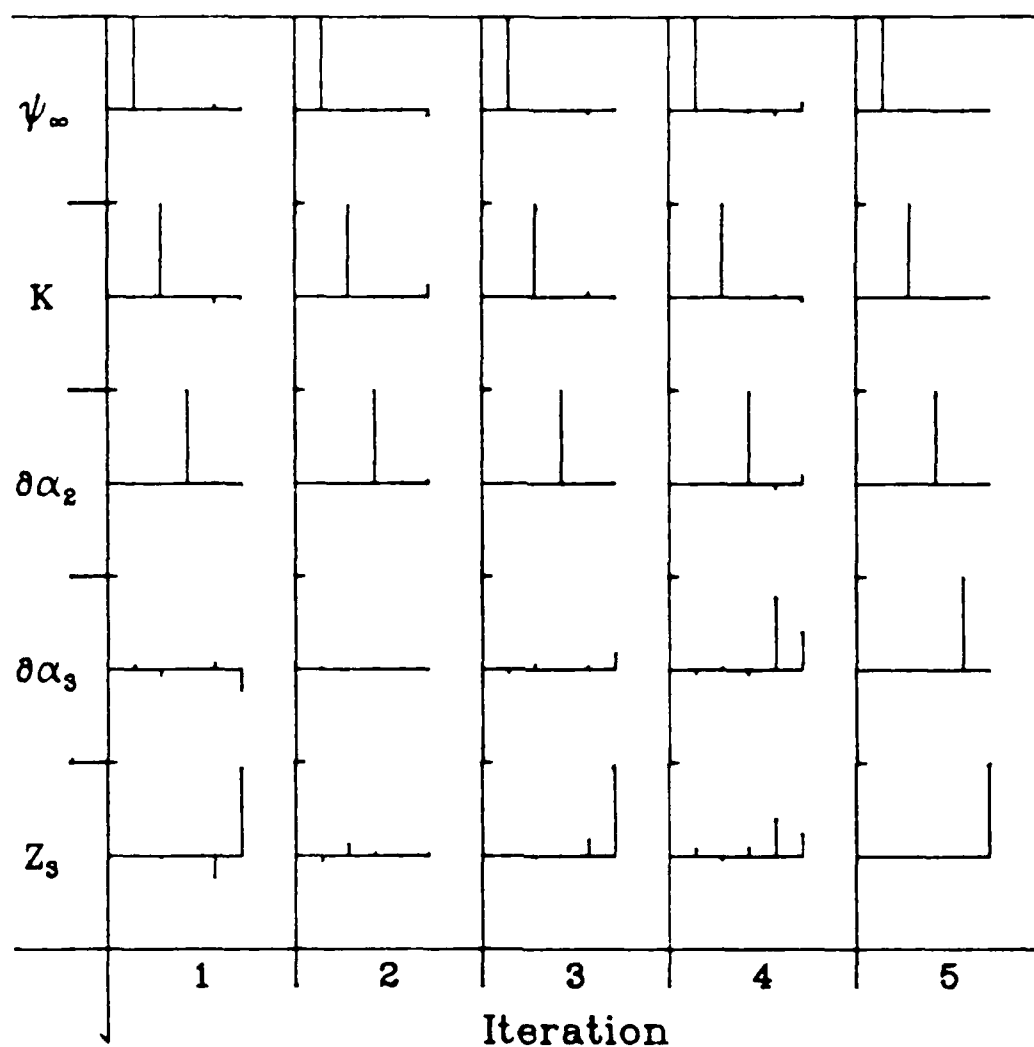


Figure 16. Parameter resolution matrices for each iteration of the SCOTCH inversion. Plotted from top to bottom are the rows of the matrices corresponding to the source parameters,  $\psi_{\infty}$  and  $K$ , and the structure parameters, upper gradient, lower gradient and interface depth. For perfect resolution, the resolution matrix would be the identity matrix.

becomes shallower (0.915 km) than the source depth (0.970 km), so the source is located within the third layer. Now the gradient in the third layer is well resolved, and approaches the value previously obtained for the second layer (about 0.6 km/s/km), while the second layer gradient approaches the value of the fixed gradient in the top layer (about 0.9 km/s/km). By the fifth iteration, the depth to the top of the third layer has decreased to 0.77 km. The result of all of these changes is that the velocity structure approximates a two-gradient model with a second order discontinuity at a depth of 0.77 km, rather than at the presumed water table depth of 0.65 km (we do not have specific information on the water table depth near SCOTCH).

The observed waveforms (Figure 15) include an impulsive first arrival. A second phase arrives at a time between the first peak and the trough. These features are well modeled by the forward synthetic seismogram at S-3A, but the two arrivals form a single peak in the synthetic for S-4, which is broader than the observed pulse. Because the gradient continues below the source in the inversion model, the diving ray arrives before the direct ray for both ranges in the inversion synthetics. This causes a somewhat early and double-peaked first pulse. Forcing the structure below the source to have a lower gradient would improve the fit of the synthetics to the data.

# SCALING RELATION FOR YIELD ESTIMATION

The source parameters determined through waveform inversion for the four Pahute Mesa events studied are summarized in Table 10. Since we have chosen an analytic form of the RDP (the Helmberger-Hadley, 1981, form), we must derive scaling relations in order to estimate the yields of these events. Burdick, et al. (1982) and Hartzell, et al. (1983) determined scaling relations for the Helmberger-Hadley RDP appropriate for Amchitka and Pahute Mesa, respectively. However, each derived separate relations for  $\Psi_0$  and  $K$  as functions of yield and source depth. Since the determinations of  $\Psi_0$  and  $K$  are not independent, we follow Barker, et al. (1985a) and equate the relations by solving for the common parameter of depth, to obtain a single scaling relation giving yield as a function of  $\Psi_0$  and  $K$ . Specifically, the general form of the relation between yield,  $\Psi_0$  and depth is

$$Y = C_1 \Psi_0^{\frac{1}{3a}} h^b \quad (24)$$

where  $C_1$  is a proportionality constant, and  $a$  and  $b$  are exponents of yield and depth, respectively, by which cavity radius is related. Similarly, the relation between yield,  $K$  and depth has the form

$$Y = C_2 \frac{h^{\frac{3}{n}}}{K^{\frac{1}{3}}} \quad (25)$$

where  $C_2$  is another proportionality constant, and  $n$  is an empirically derived constant. Solving these equations for depth and equating the two, we obtain

$$Y = C_3 \Psi_0^{\frac{1}{3a}} K^{\frac{1}{3a}} \quad (26)$$

Murphy and Mueller (1971) argue that it is reasonable for the cavity radius to depend on the cube root of yield, so  $a = 1/3$ . Using Orphal's (1970) equation for cavity radius, we obtain  $b = 0.09$ . Finally, Mueller and Murphy (1971) determined empirically that  $n = 2.4$ , so that equation (26) becomes

$$Y = C_3 \psi_x^{1.276} K^{0.826} \quad (27)$$

Of the four events modeled, BOXCAR and SCOTCH have announced yields, and so may be used to determine the proportionality constant,  $C_3$ . Using the parameters of the RDP determined for BOXCAR (Table 10) and a yield of 1300 kt (Marshall, et al., 1979), we obtain  $C_3 = 1.779 \times 10^{-12}$ . This value predicts a yield of 175 kt for SCOTCH, which is greater than the announced yield of 155 kt (Marshall, et al., 1979). If, on the other hand, we use the yield and RDP parameters for SCOTCH (Table 10), we obtain  $C_3 = 1.575 \times 10^{-12}$ , which underpredicts the yield of BOXCAR (1150 kt). Predicted yields using both proportionality constants are given in Table 10, but since SCOTCH is a small, overburied event, we prefer the predictions based on the BOXCAR constant.

Table 10 - Source Parameters from Waveform Inversion

Event	K (s <sup>-1</sup> )	$\Psi_w$ (x10 <sup>10</sup> cm <sup>3</sup> )	Yield <sup>1</sup> (kt)	Yield <sup>2</sup> (kt)	published Yield (kt)
BOXCAR	6.53	13.22	1300*	1150	1300 <sup>3</sup>
MAST	6.39	6.22	497	432	520 <sup>4</sup>
INLET	8.12	4.48	391	346	500 <sup>4</sup>
SCOTCH	10.50	2.02	175	155*	155 <sup>3</sup>

\* Constrained to announced yield.

<sup>1</sup> From equation (27) calibrated to BOXCAR ( $C_2 = 1.779 \times 10^{-12}$ ).

<sup>2</sup> From equation (27) calibrated to SCOTCH ( $C_2 = 1.575 \times 10^{-12}$ ).

<sup>3</sup> Marshall, et al. (1979)

<sup>4</sup> Dahlman and Israelson (1977)

## CONCLUSIONS

Perhaps the most crucial step in the determination of effective source functions and the estimation of yields from near-field recordings of underground nuclear explosions is the development of an accurate velocity structure model. Previous studies have obtained these models through laborious trial-and-error waveform modeling. We have reviewed the results of forward modeling for source parameters at Pahute Mesa using the velocity structure model of Hartzell, et al. (1983). The resulting synthetic seismograms provide an admirable fit to the observed waveforms, particularly for FOXCAR and SCOTCH. There is some concern, however, regarding the adequacy of the structure model for other locations within Pahute Mesa, and in how errors in the structure model effect the determination of source parameters. An additional problem is that in determining source parameters from explosions in a different structure (whether Yucca Flats, Amchitka, or one of the Soviet test sites), a new velocity structure model must first be determined.

In order to address these issues, we have developed a simultaneous inversion method which solves for the parameters of both the source and velocity structure models. A report on the initial development of the method was given in Barker, et al. (1985b) and the application of this method to Pahute Mesa data was presented in Barker, et al. (1986). We have improved the inversion technique by incorporating the jumping method of Shaw and Orcutt (1985). The primary improvement in this technique is that parameter constraints and error analyses are made on the parameters of the model, rather than on the changes in the parameters. We have presented a test inversion of

a synthetic data set. The results were quite promising, but also illustrated the limitations in the resolution of deeper structures when limited ranges are considered.

The inversions of waveforms for four Pahute Mesa explosions were presented and discussed in some detail. In general, the synthetic waveform from the inversions provided improvements over the forward modeling results in amplitude, arrival time (except SCOTCH), and in some cases, in the detailed shapes of the waveforms. For BOXCAR, the structure model obtained was not significantly different than that of Hartzell, et al. (1983). This is not particularly surprising, since these data were modeled in the development of the Hartzell, et al. (1983) structure. For the other events modeled, there was very little resolution of structure parameters deeper than about 3 km. Above this, however, the velocity gradient near INLET is very similar to that near BOXCAR, but the gradient is much greater near MAST. The results from SCOTCH suggest that the water table is somewhat deeper than the constrained value used, but that the gradient below this is similar to that of BOXCAR. Referring to Figure 1, we see that BOXCAR, INLET and SCOTCH are all located well within the Silent Canyon Caldera, the structural feature that defines Pahute Mesa. However, MAST is located on the northeast edge of the mesa where one might expect variations in velocity structure.

The parameters of the effective source functions were used to develop scaling relations and to estimate yields for the events studied. Barker, et al. (1985a) estimated yields from the forward modeling results. These values are given in Table 4. We have obtained two estimates of yield from the



inversion results, using relations determined for the announced yields of either BOXCAR or SCOTCH. We prefer the estimates from BOXCAR, which give yields of 497 kt for MAST, 391 kt for INLET and 175 kt for SCOTCH.

While the resolution of the inversion results depends on the range distribution of the observations, and the results are limited by noise or the effects of lateral structural variations in the observed data, the application to Elabute Mesa waveforms has demonstrated the usefulness of the method. Trade-offs between parameters, particularly between structure and source parameters, are quantified by the error analysis inherent in the inversion method. Finally, the inversion may be applied to near-field waveforms from any site, without any *a priori* information on the crustal velocity structure. This makes such an inversion valuable as one of many on-site verification techniques, enabling the calibration of test sites for treaty monitoring purposes.

EVIDENCE FOR LINEAR MATERIAL RESPONSE

AT HIGH STRAIN IN THE NEAR FIELD

## INTRODUCTION

Some of the most successful applications of synthetic seismogram techniques have occurred in modeling studies of near field records from explosions and earthquakes. Evidently, the crust in many situations can be reasonably approximated by a layered elastic model containing no more than ten to twenty layers. As long as sources of negligible spatial extent are considered, observed records are generally simple and can be matched in close detail from the body waves through the surface waves. Some examples of such studies are those of Helmberger and Hadley (1981), Burdick et al. (1984) and Stump and Johnson (1984), who modeled records from nuclear explosions and those of Liu and Helmberger (1985), Hartzell and Brune (1979) and Langston and Franco-Spera (1985), who studied small earthquakes. Because many crucial properties of seismic sources can be constrained from such studies, there is a continuing effort to improve their resolving power. In order to increase the accuracy of near-field source-crust models further, it is becoming necessary to consider propagation in linear anelastic media rather than just linear elastic media.

Unfortunately, developing accurate models for the distribution and frequency dependence of  $Q$  in the shallow crust is just as difficult as determining accurate  $Q$  models for the asthenosphere and mantle. Many different types of physical phenomena are believed to contribute a component to near field absorption including scattering (Menke, 1984), bulk losses due to absorbed water (Tittman et al., 1972) and losses due to frictional sliding on cracks at high strain (Stewart et al., 1983; Mavko, 1979; Day and Minster,

1986). The last of these presents a problem unique to interpretation of near field data because it is only in such data that shear strains are large enough to induce the effect. Figure 17, which is redrawn from Mavko (1979), summarizes the laboratory data which indicates that absorption begins to increase significantly in some geologic materials when shear strain exceeds  $10^{-6}$ . Two points that are illustrated by Figure 17 which will be significant in the the following discussion are that, in general, the increase in absorption is more pronounced in softer material, and that the effect should become very apparent in such materials as shear strain ranges from 1 to 100 microstrain.

In a previous report (Burdick and Barker, 1986), a method was presented for estimating shear strain fields from observed near-field velocity records. It was utilized to measure shear strain levels for a set of observations from nuclear explosions at Pahute Mesa and from a small earthquake in Imperial Valley, California. Here we present an extended analysis of that data set in which we have made a more thorough attempt to detect a reduction in apparent  $Q$  due to high shear strain levels. We begin with a brief review of the methods developed in the preceding study. Then we discuss the various types of evidence which might indicate reduction of apparent  $Q$  due to high strain in the Pahute Mesa data set. This data was recorded in a region with a dominantly sandstone lithology. Figure 17 shows that reduction of apparent  $Q$  by high strain should be most easily observed in just such an area. An improved method for measuring apparent  $Q$  is presented and utilized to measure the observed differences in  $Q$  between various combinations of P and S waves. Correlations are sought between the observed apparent  $Q$ 's and the peak shear strains induced by the P and S pulses.

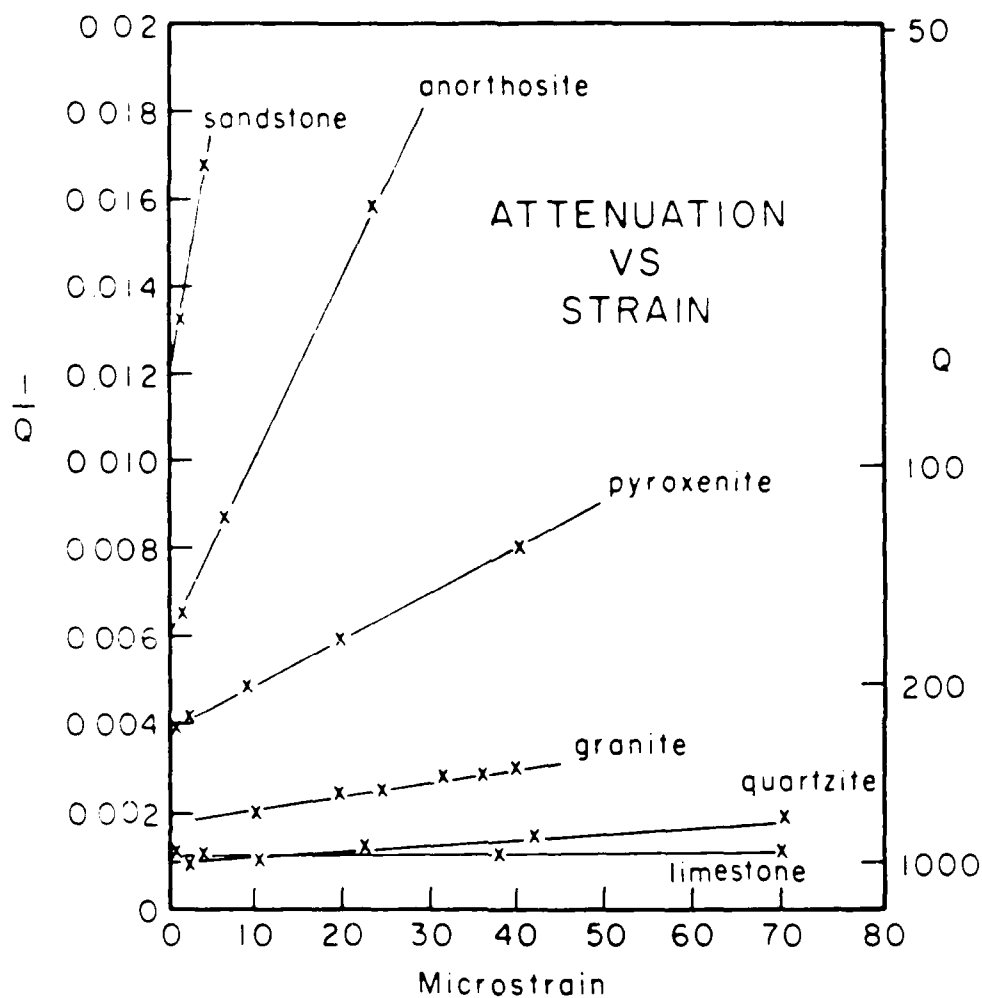


Figure 17. Linear plot of attenuation versus strain amplitude for six different dry rocks (redrawn from Mavko (1979)).

## PREVIOUS WORK

In a whole space, the strain pulse due to a point source is just the velocity pulse multiplied by the medium's slowness. In a layered half space, the velocity and strain time histories differ to some degree. The extent of the difference can be determined through synthetic seismogram computation. The nonzero components of the stress tensor are computed automatically in standard wavenumber integration calculations. Unfortunately, the technique used most often in modeling studies of near field data is summation of generalized rays because it provides high frequency synthetics in much less time. Some slight modifications of the approach are required to generate synthetic strain-time histories rather than motion-time histories. Following Helmberger (1974), we can express a single generalized ray at high frequency in the far field as

$$ray(t) = \sqrt{\frac{2}{\pi r}} \frac{d}{dt} \left[ \frac{1}{\sqrt{t}} * \Im m \left( \sqrt{\frac{p}{\eta}} \frac{dp}{dt} \prod A R \right) \right] \quad (28)$$

evaluated along the Cagniard contour in the complex  $p$  plane. The factor  $\prod$  is the product of the reflection and transmission coefficients along the raypath.  $A$  is the source radiation pattern term and  $R$  is called the receiver function. The only difference between a strain generalized ray and a seismic motion generalized ray is a change in the expression for the receiver function. These functions for either motion or strain are given in Table 11. The factors  $p$  and  $\eta$  are horizontal and vertical slownesses,  $\alpha$  and  $\beta$  are the P and S velocities and  $\pm$  is plus or minus one depending on whether the ray is up or downgoing at the receiver. The functions on the left are for receiver points in the medium and those on the right are for points on the free surface.

Table 11

## Receiver Functions

Seismic MotionsIn the Medium

$$R_{PZ} = -\epsilon' \eta_a$$

$$R_{PR} = -p$$

$$R_{SZ} = p$$

$$R_{SR} = -\epsilon' \eta_\beta$$

$$R_{S\theta} = p$$

At the Free Surface

$$R_{PZ} = 2\eta_a(\eta_\beta^2 - p^2)/\beta^2 R(p)$$

$$\text{with } R(p) = (\eta_\beta^2 - p^2)^2 + 4p^2\eta_a\eta_\beta$$

$$R_{PR} = -4\eta_a\eta_\beta/\beta^2 R(p)$$

$$R_{SZ} = 4p\eta_a\eta_\beta/\beta^2 R(p)$$

$$R_{SR} = 2\eta_\beta(\eta_\beta^2 - p^2)/\beta^2 R(p)$$

$$R_{S\theta} = 2p$$

Strains

$$R_{PZZ} = -\epsilon' \eta_a R_{PZ}$$

$$R_{PZR} = -p R_{PZ}$$

$$R_{PRZ} = -\epsilon' \eta_a R_{PR}$$

$$R_{PRR} = -p R_{PR}$$

$$R_{SZZ} = -\epsilon' \eta_\beta R_{SZ}$$

$$R_{SZR} = -p R_{SZ}$$

$$R_{SRZ} = -\epsilon' \eta_\beta R_{SR}$$

$$R_{SRR} = -p R_{SR}$$

$$R_{S\theta Z} = -\epsilon' \eta_\beta R_{S\theta}$$

$$R_{S\theta R} = -p R_{S\theta}$$

$$R_{PZZ} = -cp R_{SZ}$$

$$\text{with } c = (\alpha^2 - 2\beta^2)/\alpha^2$$

$$R_{PZR} = -p R_{PZ}$$

$$R_{PRZ} = p R_{PZ}$$

$$R_{PRR} = -p R_{PR}$$

$$R_{SZZ} = cp R_{SR}$$

$$R_{SZR} = -p R_{SZ}$$

$$R_{SRZ} = p R_{SZ}$$

$$R_{SRR} = -p R_{SR}$$

$$R_{S\theta Z} = 0$$

$$R_{S\theta R} = -p R_{S\theta}$$

The above formalism was used to compute synthetic velocity and strain pulses for several relevant test cases. Definite differences existed in the velocity and strain time histories, but they were small in most cases. This suggested that a method analogous to the one that works in a whole space could be devised for the layered half space case; a procedure that transforms observed velocity records to estimated strain records. Whereas in the former case velocity is multiplied by slowness to obtain strain, in the latter velocity can be transformed to strain by convolving the velocity pulse with frequency dependent transfer operators. These operators can be generated by deconvolving synthetic velocity from synthetic strain records of any given source-receiver geometry. In most cases, these operators turn out to be very delta-like functions with amplitude controlled by the velocity at the receiver site, just as one might expect. The first data base processed using the transfer operators was a suite of near-field velocity records from 6 Pahute Mesa nuclear explosions. They were SCOTCH, INLET, MAST, HALFBEAK, ALMENDRO and BOXCAR. The recording instruments were L7 velocity meters, so the signals recorded on them were essentially velocity versus time. In order to compute transfer functions, it was necessary to select a layered velocity model for Pahute Mesa. The one chosen was presented by Barker et al. (1985) who developed it specifically to give accurate near field synthetics. An example of the computation of a transfer operator for a 1000 kt event located at 1 km depth in the Pahute Mesa structure is shown in Figure 18. The synthetic vertical and radial velocity traces are shown on the left, the four nonzero partial derivatives of displacement with respect to spatial coordinates in the center and the transfer functions on the right. The top strain is  $E_{zz}$ , the bottom is  $E_{rr}$  and the average of the center two is  $E_{rz}$ . Note that the center two traces sum to zero, so the free surface condition is maintained. The



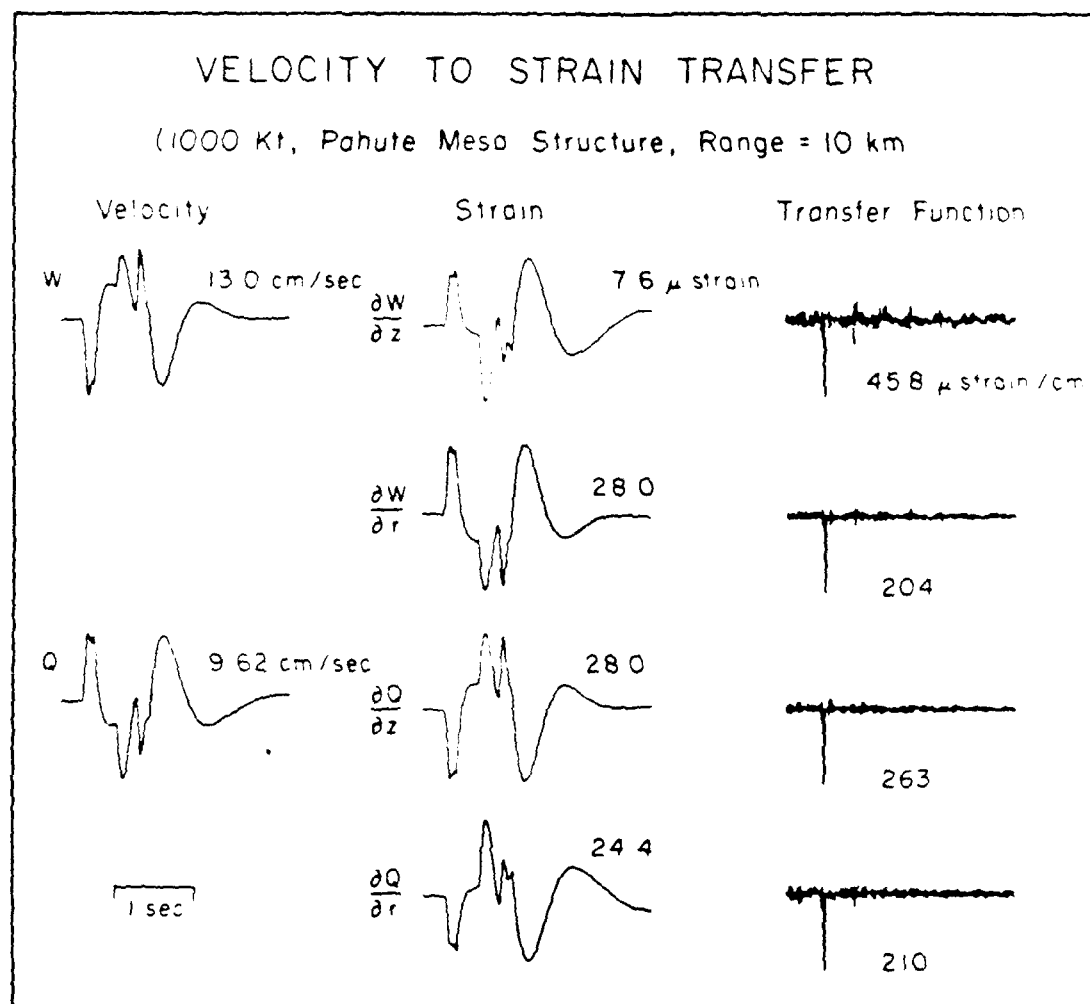


Figure 18. An example of the computation of the velocity to strain transfer functions for the Pahute Mesa structure. The velocity traces on the left are deconvolved from the strain traces in the center to produce the transfer operators on the right.

transfer functions are computed by transforming the velocity pulse and the corresponding partial derivative pulse into the frequency domain using a fast fourier transform algorithm. The latter is divided by the former and the inverse transform taken. The signal to noise ratio of the impulses in Figure 18 is about 5 to 1. To suppress the noise, a gaussian filter with a cutoff of 5 hz is applied to the transfer operator before it is applied to the data. In principle, both the vertical and radial records could be used along with the appropriate transfer operators to estimate strain. In practise, it is difficult to do so because the synthetics are never really exact, and generally the vertical is predicted better than the radial. It is difficult to achieve the delicate cancellations required to maintain the free surface condition. Therefore, the vertical component is used to generate one of the two nonzero strain components for an explosive source, and the free surface condition is used to generate the other from it.

The next records to which the velocity to strain transfer operators were applied were from an aftershock of the 15 October 1979 Imperial Valley earthquake. The aftershock was studied in some detail by Liu and Helmberger (1985) who provided a mechanism, moment and time function for it. They reported the event depth as 9.5 km. The predominant arrival at all stations was a strong, unusually simple S wave, so in this case we computed S rather than P operators. The polarity information in the data set was very clear, and it allowed Liu and Helmberger (1985) to constrain the mechanism to be almost pure vertical strike slip. They reported a moment of  $1.0 \times 10^{24}$  dyne-cm and a triangular time function with a rise of 0.1 and a fall of 0.1 s.

From our modeling studies, however, we conclude that a moment value of  $0.6 \times 10^{27}$  dyne-cm and a time function with a rise of 0.3 and a fall of 0.1 s are more accurate.

The nonzero strains generated by incident SV are  $E_{zz}$  and  $E_{RR}$ . As before, we wished to insure that the free surface condition would be satisfied, so we used only the radial component of motion and generated both strains from it. The transverse records were used to generate the third nonzero component of strain. Another important difference between the Pahute Mesa and Imperial Valley data sets is that, in the latter, Liu and Helmberger (1985) found evidence for a very low shear Q in the form of a strong frequency shift between P and S waves. The values they used for shear Q in the top half km of their crustal model were of the order of 10. This resulted in a relatively distance independent  $t^*$  of .132 s. Values of shear Q this low are atypical and could easily be interpreted as an indication that nonlinear reduction of Q due to high strain is taking place. The peak shear strain values for 16 observing stations ranged from 5 to  $65 \times 10^{-6}$ . We here report on our additional attempts to detect in the Imperial Valley and Pahute Mesa data sets, any evidence of nonlinear material response.

### EXPLOSIONS

Devising means for detecting nonlinear reduction in apparent Q from near-field or teleseismic observations of nuclear explosions is difficult because there are always tradeoffs between the effects of attenuation and other processes. In the near field, the decay rate of wave fields is dependent on both the elastic and the anelastic crustal structure. At teleseismic distances, estimated values for total attenuation (embodied in an

estimate of  $t^*$  are dependent on both the yield scaling of the explosion

source function and the average value of  $Q$  along the raypath. If, in the former case, the elastic crustal structure were independently known a nonlinear reduction in  $Q$  could be observed as an anomalously high rate of decay of amplitude with distance. In the latter, it could be observed as a yield dependent measurement of  $t^*$  providing the source function yield scaling is in fact accurately accounted for. In this section, we compare crustal structures and  $t^*$  values estimated from high strain explosion data to structures and  $t^*$ 's estimated by other means.

In the near field modeling studies of Burdick et al. (1984) and Hartzell et al. (1983), elastic crustal structures were developed for Amchitka and Pahute Mesa by forward modeling of observed velocity pulse amplitudes and wave shapes. The question is whether nonlinear effects were inadvertently mapped into details of the crustal model. Figure 19 shows the estimated peak shear strain for the Pahute Mesa data as a function of range. Theoretical strain-distance curves computed assuming the Hartzell et al. (1983) structure and elastic material response for the largest (BOXCAR, 1300 kt) and smallest (SCOTCH, 155 kt) events are also shown. The theoretical strain for the smallest event does not fall below one microstrain until 25 km. Thus, the entire Pahute Mesa near-field data set is within the strain regime in which the laboratory data indicates that nonlinear processes might be significant. The Amchitka event, MILROW, was comparable to BOXCAR in size so it probably generated shear strains of the same order. The other Amchitka event, GAMMIFIN, was three or four times as large, but the velocity pulses it generated were very nearly the same size as those from MILROW. The two events therefore probably generated comparable shear strains at the free surface.

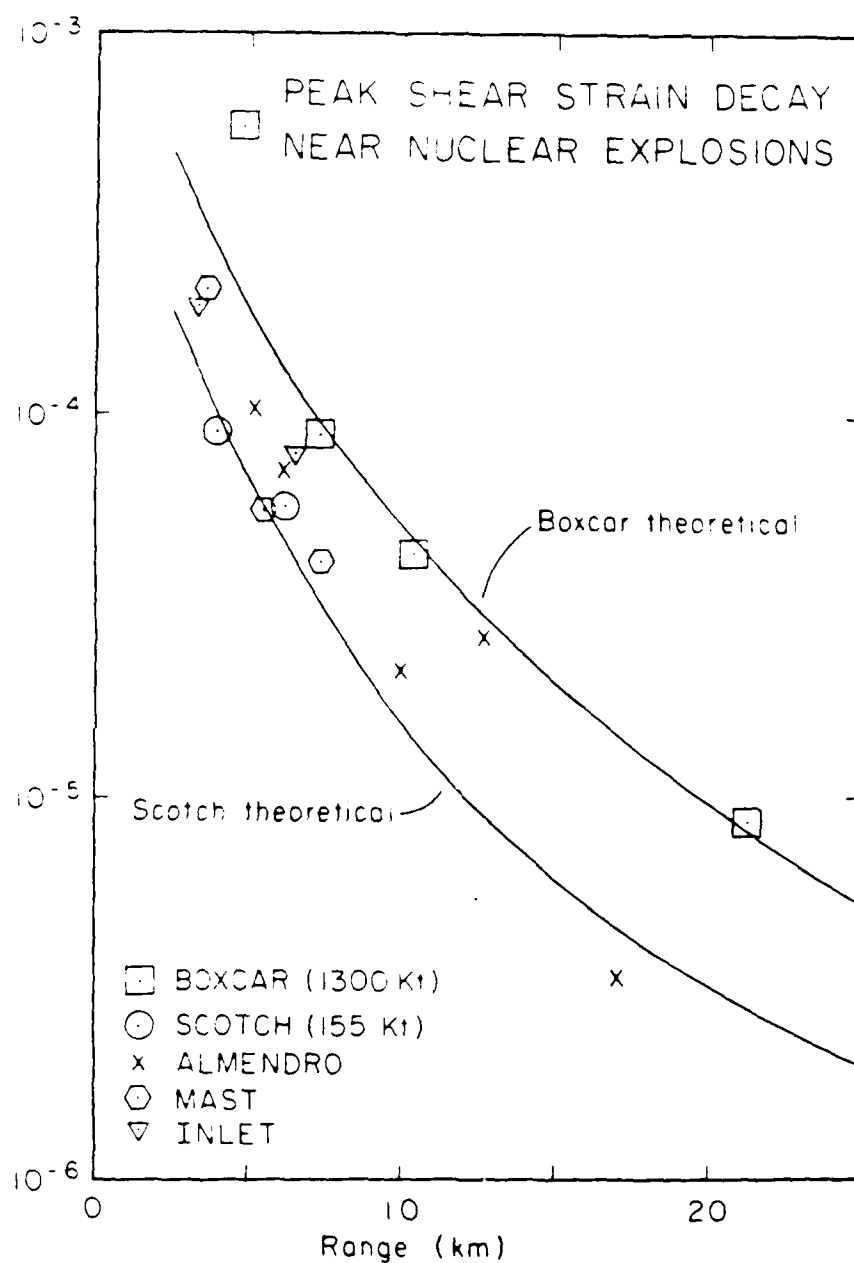


Figure 19. The decay of peak shear strain near to nuclear explosions. The largest observed value of shear strain is  $10^{-3}$ . Theoretical curves are shown for the largest and smallest events studied. The observations appear to follow the theoretical predictions.

Over the years, both US nuclear test sites have been characterized in close geophysical detail. Velocity profiles based on low strain types of observations at Pahute Mesa have been made by Hamilton and Healy (1969) and Carroll (1966) among others. The high strain and low strain crust models are compared in Figure 2 of the previous section. There is certainly no evidence to suggest that any biasing has occurred. The observed and predicted amplitude decay with distance is given in figures 9, 11 and 13 for both the forward and inverted crust models. There is no indication that the wave field is being anomalously attenuated with distance. Crustal structure models for Amchitka based on high strain versus low strain data are compared in Figure 10. The MILROW and CANNIKIN models are based on near field observations, and the Engdahl (1972) model is based on low strain refraction information. Again, there appears to be no bias. Figures 21 and 22 show the observed versus predicted peak velocity value as a function of range for MILROW and CANNIKIN respectively. There is no evidence for a high rate of attenuation that is not accounted for in the linear elastic model. Note that, for the vertical component, the theoretical curve continues to predict the observations even inside the spall zone (less than 3 km) though this is not true for the radial. In any event, there is no evidence in the comparisons of high strain versus low strain crustal models that any biasing due to high strain effects has occurred. Likewise, there is no evidence of low apparent  $Q$  in the peak amplitude-distance data.

It is difficult to assess how a substantial unaccounted for reduction in effective  $Q$  in the near field would affect an estimate of  $t^*$  based on teleseismic amplitudes. The usual assumption in such measurements is that the explosive source is effectively spherical. If this assumption remains true,

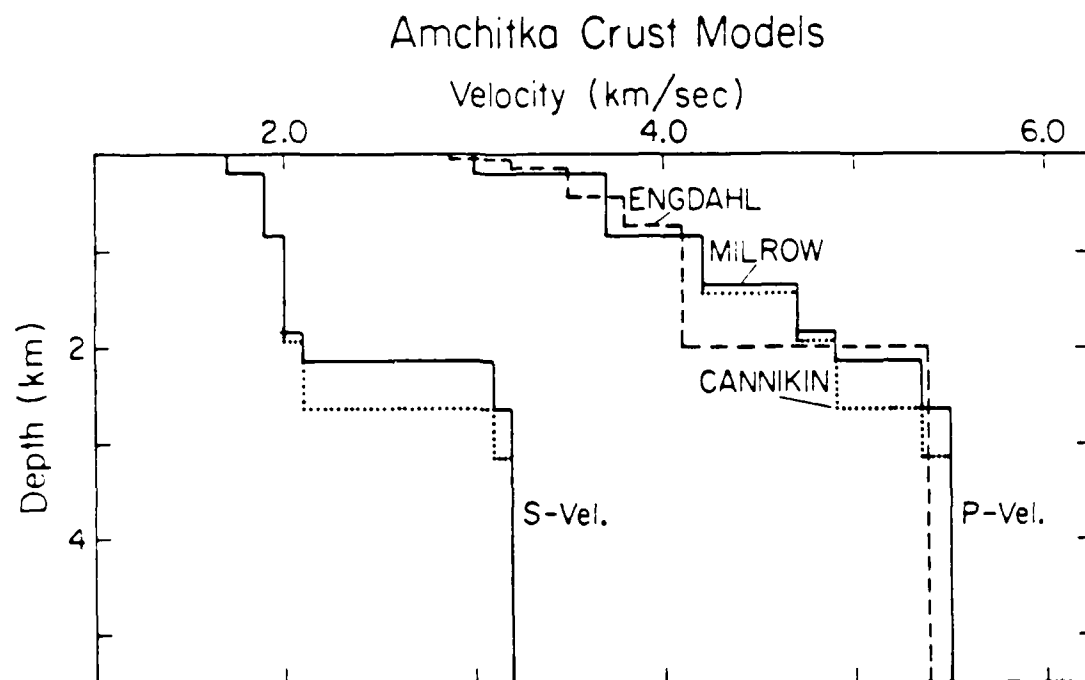


Figure 20. The three models for the Amchitka crust are compared. All three models predict essentially the same P-wave times. The CANNIKIN and MILROW models also fit the near field waveforms.

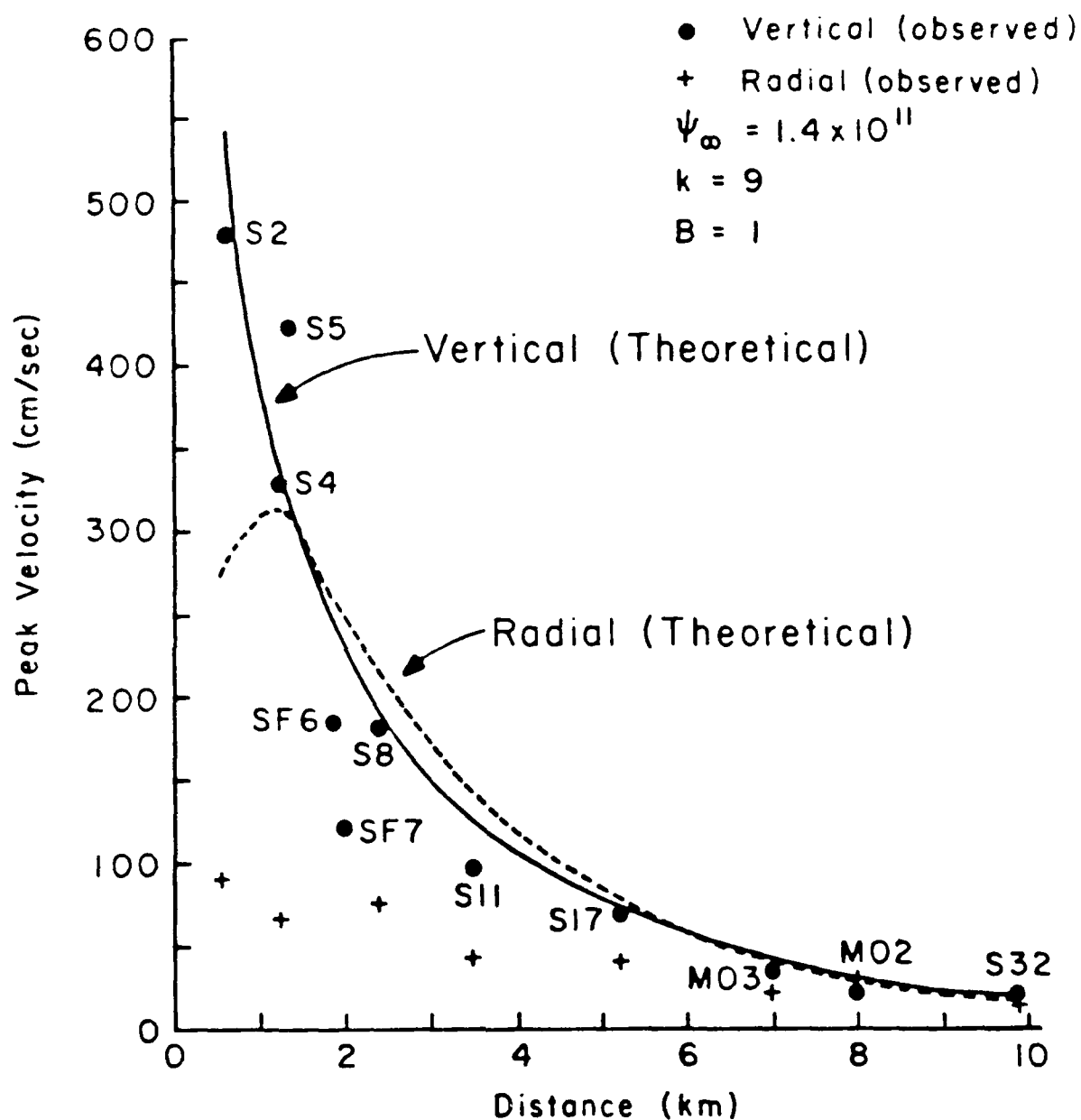


Figure 21. A comparison of the observed velocity data and elastic model predictions for MILROW. Observed peak vertical (circles) and radial (squares) velocities and elastic model predictions (solid and dashed lines) plotted as a function of epicentral distance.



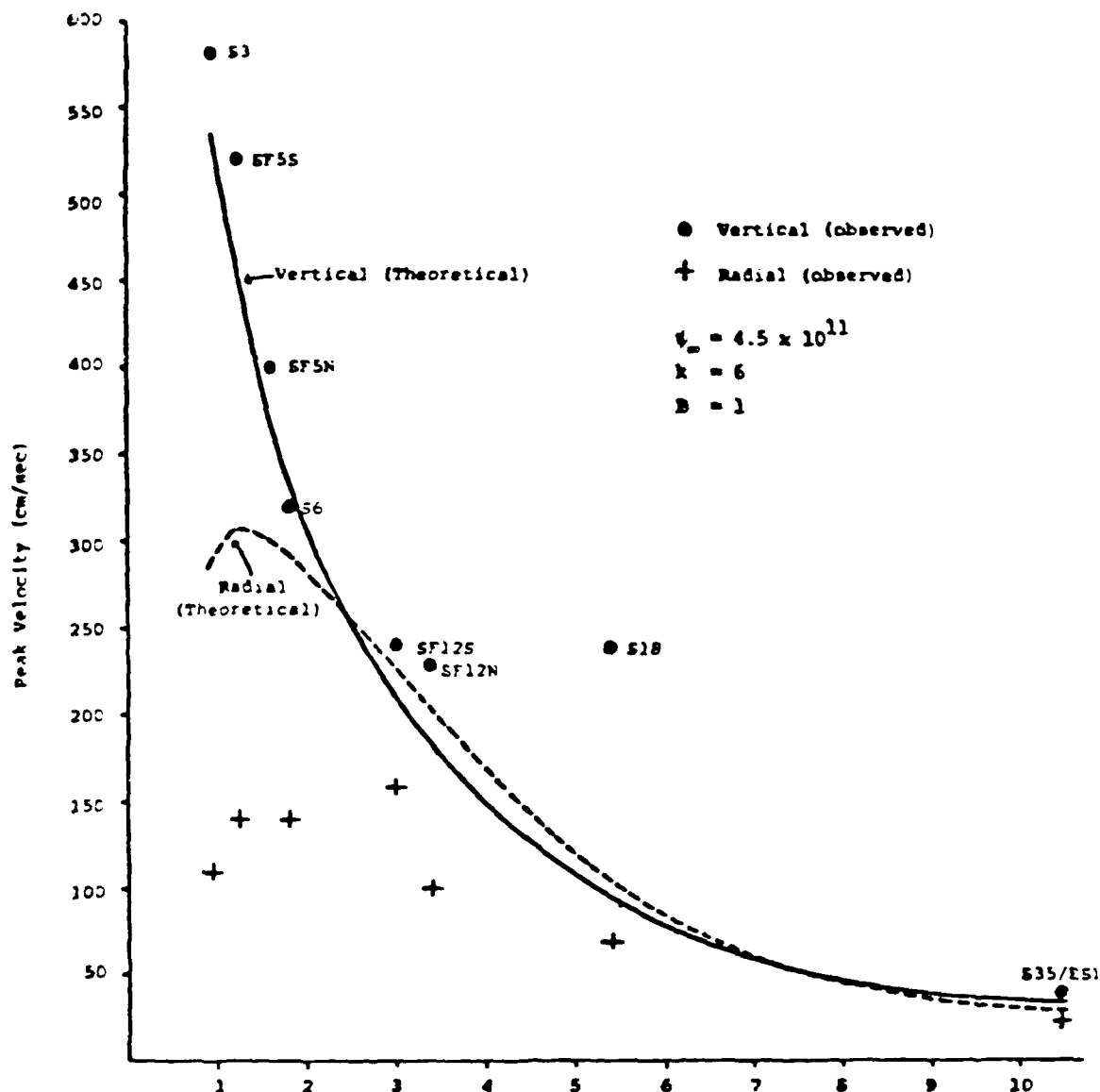
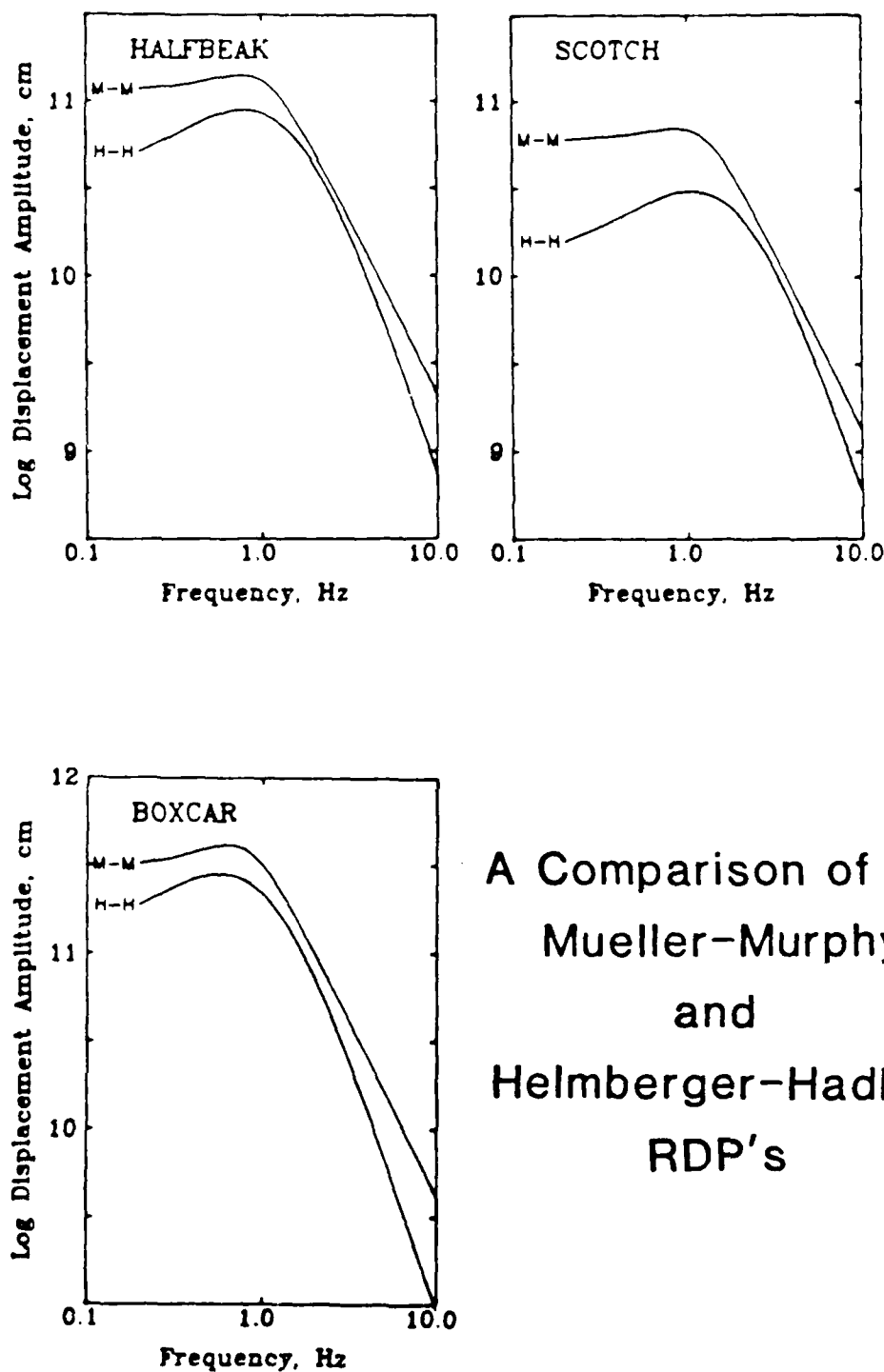


Figure 22. A comparison of observed velocity data from within the spall zone of CANNIKIN with elastic predictions based on data from the elastic region. Observed peak vertical (circles) and radial (squares) velocities and elastic model predictions (solid and dashed lines) plotted as a function of epicentral distance.

but the reduction in  $Q$  extends beyond the near field data, the initial strength of the far field elastic wave field as measured from that data would be overestimated. The average value of  $t^*$  for the whole raypath would be overestimated. If the zone in which effective  $Q$  is reduced is very aspherical and confined to the surface layers, the initial field strength would be underestimated and  $t^*$  for the whole path underestimated. The only effect which should be present in either case would be a yield (peak shear strain) dependence of the phenomenon.

As noted above, the important tradeoff in such measurements is between uncertainties in the yield scaling of the RDP and  $t^*$ . The apparent yield scaling for the Amchitka test site based on near-field modeling was given by Burdick et al. (1984), and for Pahute Mesa by Burger et al. (1987). In both cases, the RDP formalism used was the one proposed by Helmberger and Hadley (1981). Another widely recognized RDP and yield scaling model for Pahute Mesa is the one presented by Mueller and Murphy (1971). This model was also based to some extent on near field field data but primarily on near regional data where strains are much lower. The RDP spectra are compared in Figure 23 for a large (BOXCAR), intermediate (HALFBEAK) and small (SCOTCH) event. The differences at long period are not significant since the near field data contained no long period information. The corner frequencies and spectral falloff rates near the peak track very well over the entire range of yields. As explained by Burger et al. (1987), the absolute offset of the two spectra results in the Mueller-Murphy source giving consistently higher  $t^*$  estimates, but that is not important to this discussion. The point is that the yield scaling of the RDP indicated by the near field data does not appear to be biased in any significant way. The average earth  $t^*$  values determined by



# A Comparison of the Mueller-Murphy and Helmberger-Hadley RDP's

Figure 23. Predicted far-field source displacement spectra for BOXCAR, HALFBEAK, and SCOTCH. The Mueller-Murphy (1971) source models are based on the announced yields. The Helmberger-Hadley (1981) source models are based on the near-field modeling results of Barker et al, (1985).

comparisons of near field to teleseismic short period P waves are listed in Table 13. At Anchitka, the estimated values for MILROW and CANNIKIN differed by only 10% even though the yields varied by a factor of four or five. At Pahute Mesa, there is a total variation of about 30% in estimated  $t^*$  with a variation in yield of an order of magnitude. The extremal values were for the largest and smallest events, but other than that there are no convincing systematics. There is certainly no strong evidence for reduction of effective Q in the near field having a large effect.

### EARTHQUAKES

The aftershock of the Imperial Earthquake occurred much deeper than the typical depth of explosions. In fact, it was so deep that the body wave propagation to the near field stations remained very simple. The arrivals are well represented by a single upgoing generalized ray. The rays to all stations depart nearly horizontally from the source and then turn sharply upward under the stations because of the strong velocity gradient. The observed S wave pulses are very simple in character, and easy to model as shown in Figure 24. The SH and SV waveshapes are very similar because the rays emerge nearly vertically at the receiver. The absence of ringing indicates that reverberations at the stations are not significant. As noted above, the peak shear strains generated by the 16 S waves shown were estimated in previous work, and our purpose here is to determine whether there is significant evidence of reduction of effective Q due to these strains.

The observed decay of peak shear with distance for the aftershock is shown in Figure 25. The theoretical curves for a large and small explosion from Figure 19 are shown for reference. The levels of shear strain generated

Table 12 - Measured Values of  $t^*$  versus Yield

Test Site	Event	Yield (kt)	$t^*$ (sec)
AMCHITKA	CANNIKIN	< 5000	.94
	MILROW	1000	.85
NTS	BOXCAR	1300	.92
	ALMENDRO	570	.69
	MAST	520	.80
	INLET	500	.72
	HALFBEAK	365	.74
	SCOTCH	155	.61

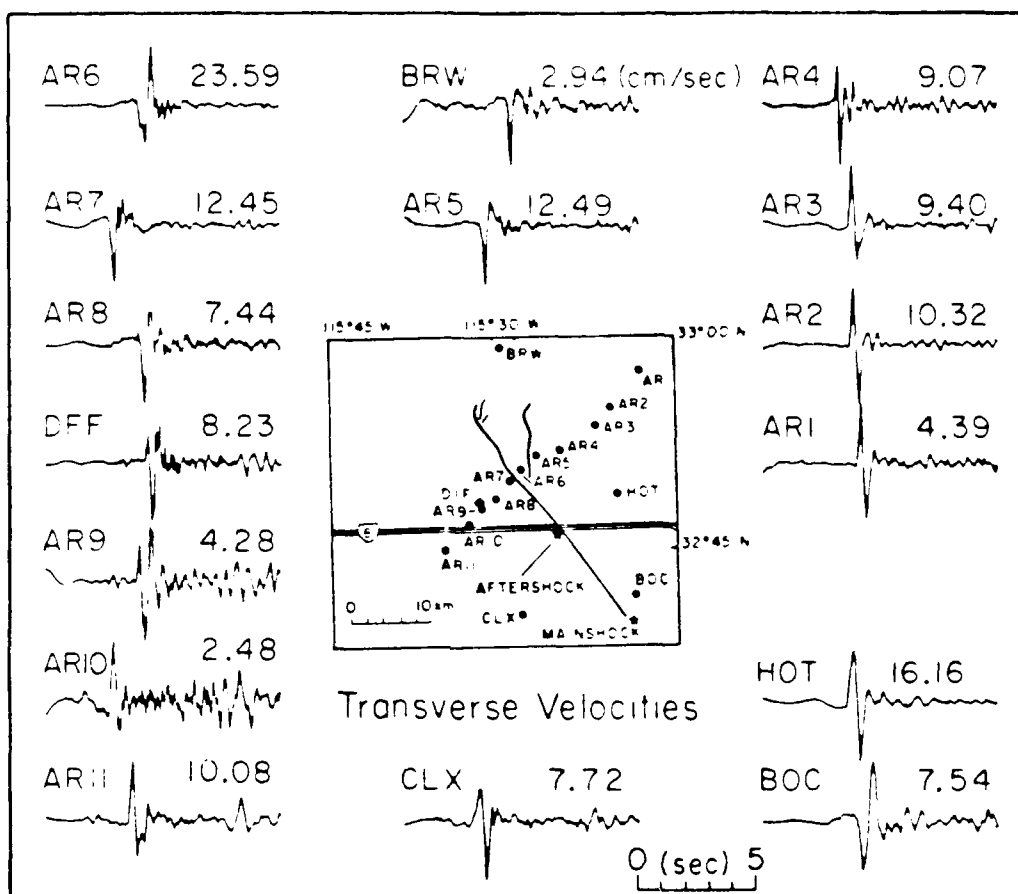


Figure 24a. The transverse ground velocities from the 23:19, 15 October 1979 Imperial Valley aftershock.

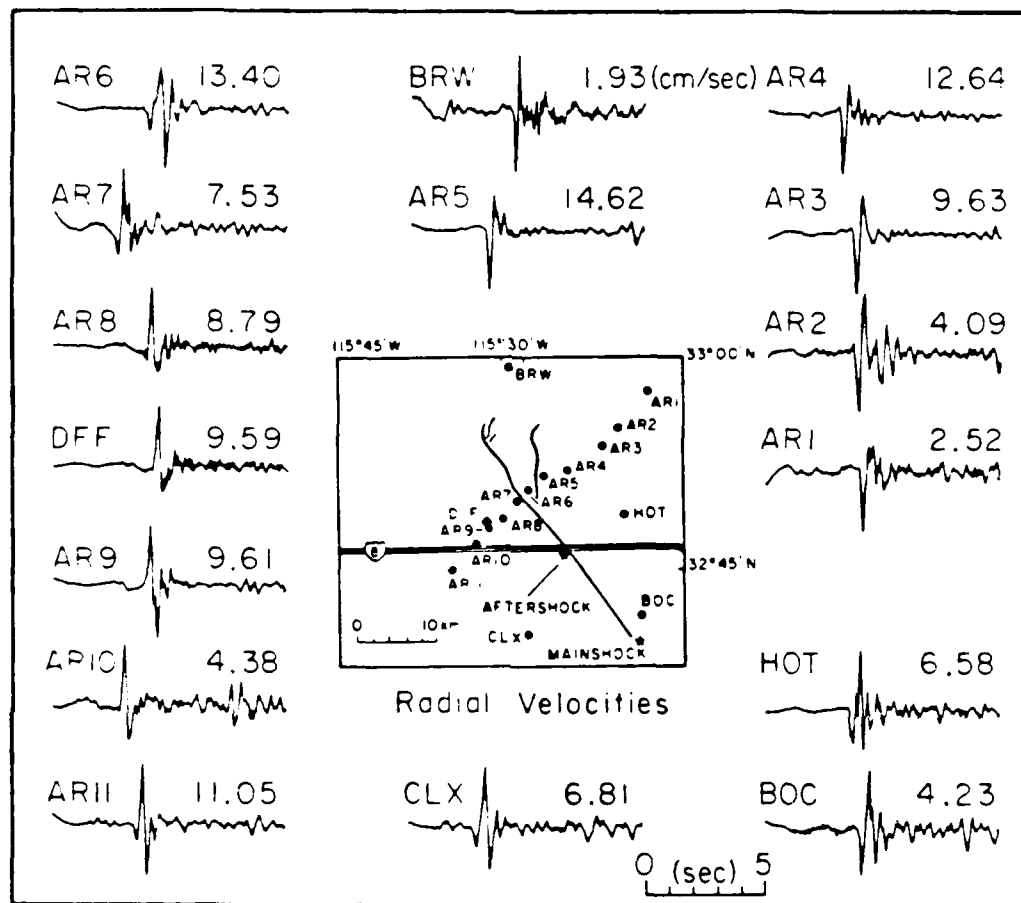


Figure 24b. The radial ground velocities from the 23:19, 15 October 1979 Imperial Valley aftershock.

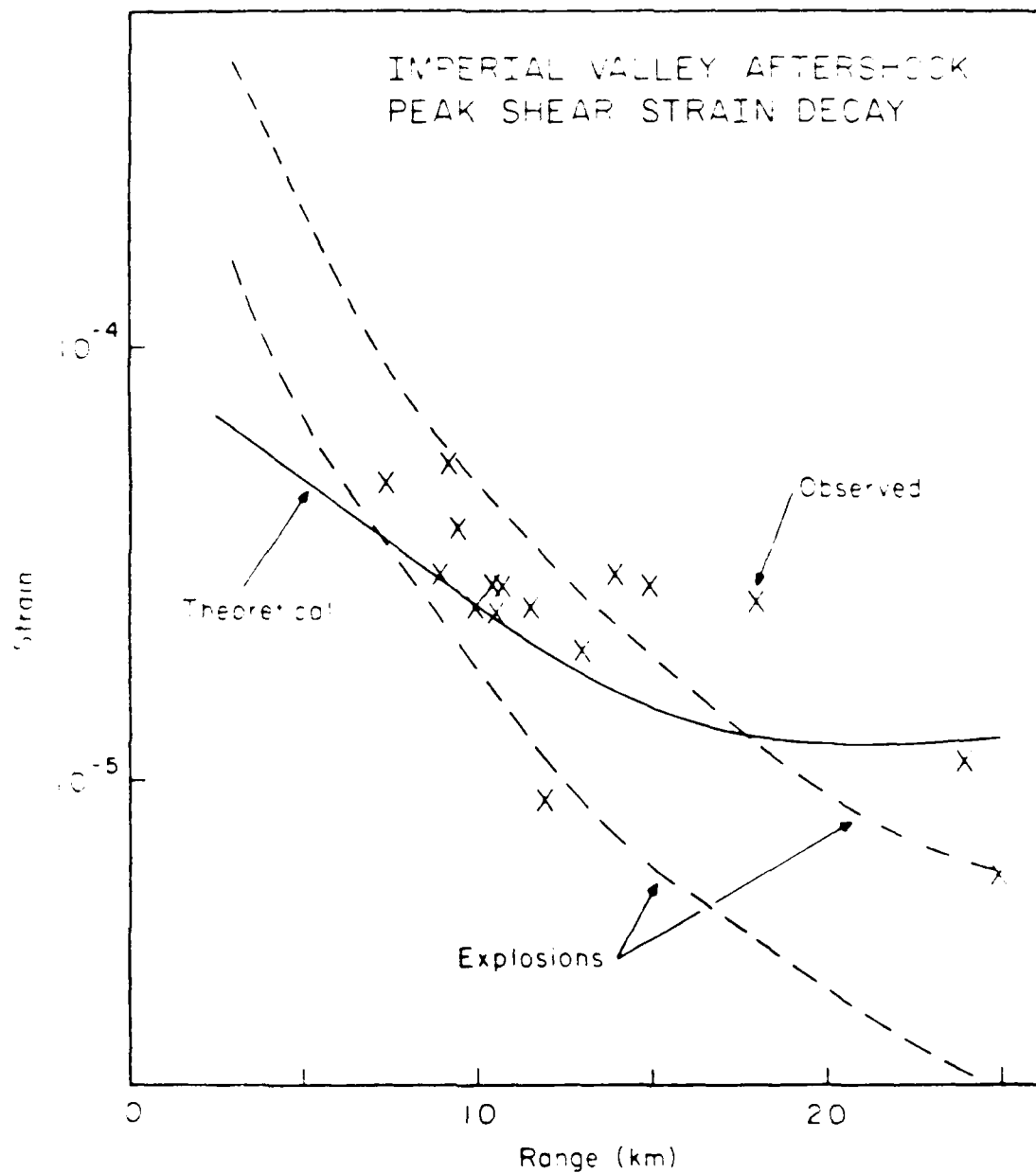


Figure 25. The decay of peak shear strain near the Imperial Valley aftershock. The curves for decay of stress near nuclear explosions from Figure 19 are shown for reference. Note that the levels of strain are similar



by the aftershock are quite comparable to those generated by the nuclear events although the shear modulus of the Imperial Valley sediments is lower than those at the surface of Pahute Mesa. The decay of strain with distance is different for the explosion and earthquake cases, but this is primarily due to the greater depth of the aftershock. There is more scatter in the earthquake data, but this is at least in part caused by the azimuthal radiation pattern of the double couple which has not been corrected for in this Figure. Given the evidence for the high peak shear strains in Imperial Valley and the susceptibility of sandstone lithologies to reduction in apparent  $Q$  by strain, the Imperial Valley aftershock data set appears to be ideal for searching for evidence of this phenomenon.

Liu and Helmberger (1985) initially concluded that the effective  $Q$  in the Imperial Valley had to be relatively low because of the strong shift in frequency content between P and S waves. Such a shift has, of course, several possible origins. These include elastic propagation differences for P versus S waves and directivity differences at the source as well as strong differential attenuation. The elastic propagation is so simple in its geometry, however, that it is not a likely candidate. Source directivity effects can be damped by averaging over azimuth, so it should be possible to isolate the effects of differential attenuation to some degree. If it correlates with the difference in peak shear strain carried by P and S, we would have some evidence of nonlinear material response. Figure 26 shows some examples of the strong P to S frequency shift. Three examples of observed P waves are shown in the left column. Even though they are very high in frequency content, they are relatively simple for near-field S waves just as the S waves in Figure 25 are. In the center column are Futterman attenuation

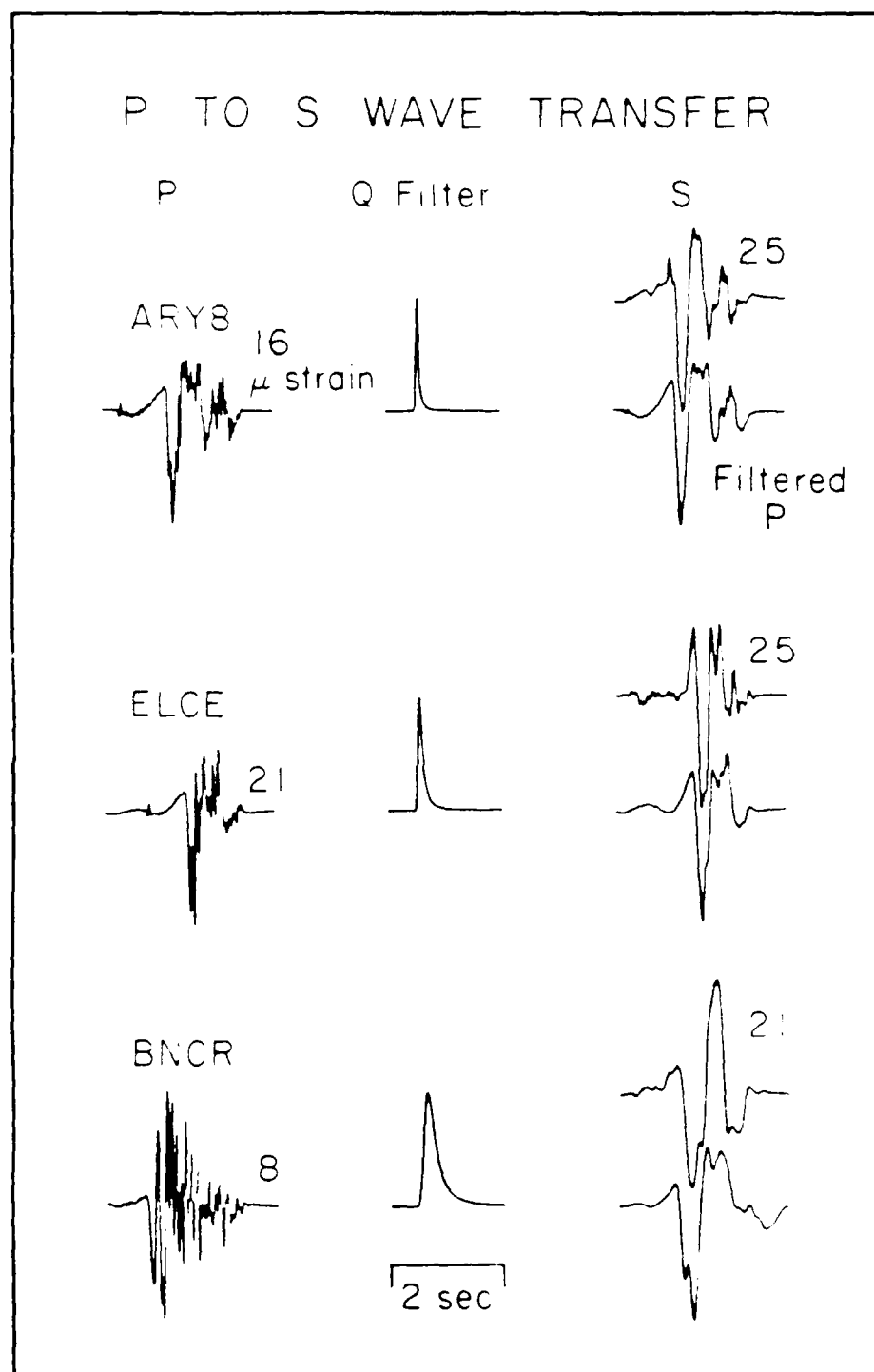


Figure 26. Transformation of P into S-waves with a  $Q$  filter. The observed P-waves are shown on the left; the  $Q$  filter response in the center column and the filtered P is compared to the original P on the right. The variability of the apparent relative attenuation

AD-A192 212

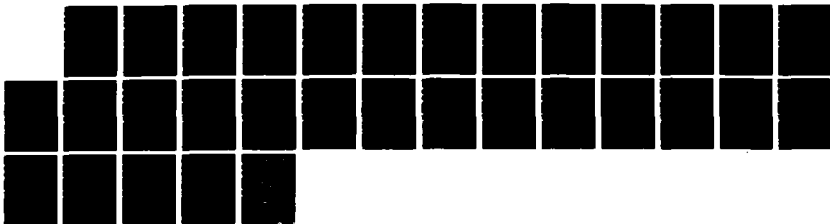
FORWARD AND INVERSE MODELING OF NEAR-FIELD SEISMIC  
WAVEFORMS FROM UNDERGR (U) HOODWARD-CLYDE CONSULTANTS  
PASADENA CA L J BURDICK ET AL 05 APR 87 WCCP-R-87-01  
AFGL-TR-87-0250 F19628-85-C-0036

2/2

UNCLASSIFIED

F/G 8/11

NL





operators that transfer the P pulses into pulses that most resemble the S waves. The criterion for selecting these operators is discussed in the following section. The filtered P is compared to the associated S pulse in the right column. The peak shear strain carried by each pulse is also indicated. The amount of relative attenuation is quite variable, and in these examples it appears as if it may be related to the difference in P and S strain. Also, the filtered P and S waves match each other in close detail indicating that a difference in attenuation might be the most significant difference between them.

It must be acknowledged at this point that representing the effects of nonlinear material response with simple attenuation operator may turn out to be a very poor approximation. As discussed in Day and Minster (1986), it is necessary to consider propagation in media with generalized constitutive laws to treat the problem in its entirety. However, solutions to such problems are much more complex than those commonly used in seismology, and it is appropriate to first search for the types of correlations in observations that might be expected if nonlinear effects are important. If such patterns begin to emerge, they can be modeled more exactly at a later time.

#### An Improved Method of Measuring $t^*$

Measuring the value of  $t^*$  from the relative frequency content of P and S waves is a commonly used technique. Kanamori (1967), who used the method to measure mantle  $t^*$  from ScP and ScS phases, discusses the theory and assumptions behind the approach. For reasons of mathematical convenience, he suggests choosing an optimal value for  $t^*$  by taking the natural log of the

spectral ratio of S to P and fitting a straight line to the results. In this discussion, we will refer to this as measuring  $t^*$  by minimizing the Ln Least Squares or LLS norm. That is,

$$LLS = \min \int \left[ \ln(S/P) - \frac{\omega t^*}{2} \right]^2 d\omega \quad (29)$$

where S and P are the amplitude spectra. Using the definition for a frequency independent attenuation operator A,

$$A(t^*) = \exp\left(\frac{\omega t^*}{2}\right) \quad (30)$$

the LLS norm can be recognized as

$$LLS = \min \int [\ln(S) - \ln(A(t^*)P)]^2 d\omega \quad (31)$$

Note that because only the amplitude spectra are used the phase information is neglected.

An alternate norm that is frequently used to analytically compare pulses is the one suggested by Burdick and Mellman (1974). Because they express their norm in terms of cross correlation operators, many fail to realize that it is just a standard least squares (LS) norm. It could be expressed in this case as

$$LS = \min \int [S - A(t^*)P]^2 dt \quad (32)$$

where the S and P are aligned in time at max correlation and where each pulse is normalized to unit squared area. The squared difference function in the brackets is just a function of time, so an immediate application of Parseval's theorem to it gives

$$LS = \min \int [S - A(t^*)P]^2 d\omega \quad (33)$$

where obviously P, S and A are to be in the time domain in the first of these two equations and in the frequency domain in the second. Thus the LLS and the LS norms differ only in that one minimizes the difference between natural logs of spectra and the other the spectra themselves, and that the former ignores phase information while the other utilizes it. While the LLS norm is easier to apply, it does have some undesirable numerical properties as we show in the following.

To illustrate the difference in the two norms, we consider a sample record from the Imperial Valley data set (ELCE Radial S and Vertical P). The LLS norm indicates that  $t^*$  is .03 s and the LS norm indicates .09 s. The LLS line was fit over the frequency range of 1 to 10 hz since this is the range where signal to background noise is larger than 1. The fit of the LLS line to the  $\ln(\text{spectral ratio})$  is compared to the fit of the LS line in Figure 27. The LS line has been arbitrarily given the same value at 1 hz as the LLS line. It is clear that the LLS norm fits the 5 to 10 hz information better than the LS norm presumably because it is more sensitive to it. However, one would wish for a norm to be most sensitive to the data that is most reliable, and in general that is not the highest frequency information. To further establish the strong sensitivity of the LLS norm to the higher frequencies, it was

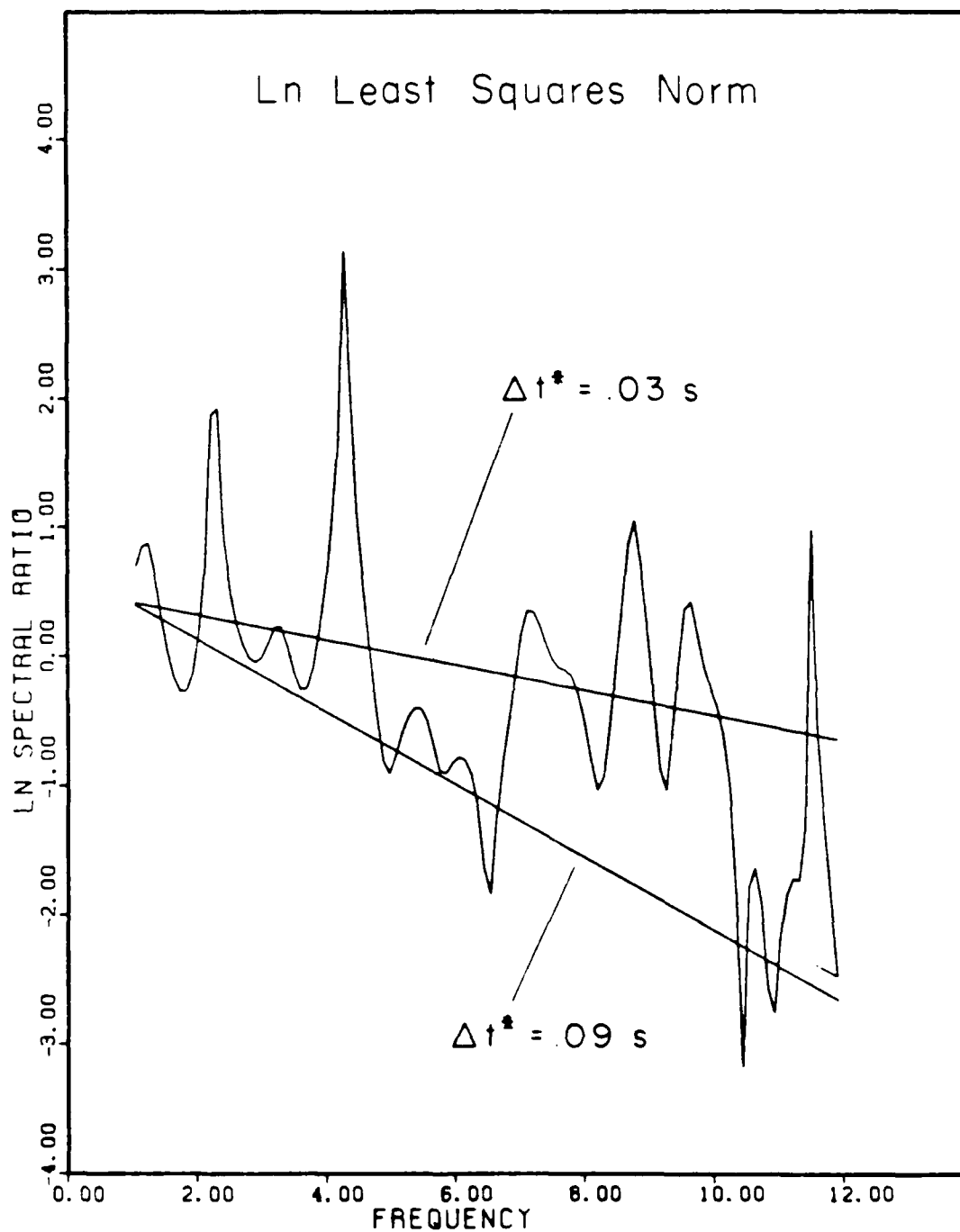


Figure 27. A comparison of the straight line fit to the spectral ratio obtained from the Ln least squares norm (0.3s) versus that prescribed by the least squares norm (0.9s). The former fits the high frequency data better.



applied to a suite of 12 Imperial Valley aftershock record pairs; first fitting 1 to 10 hz and then 1 to 15 hz data. On average, including the extra high frequency information changed the estimated value of  $t^*$  by a factor of 3. The estimated value for the spectral slope is very unstable and controlled by high frequencies. The average estimated value was about the same in the two cases since as many slopes were perturbed up as down. Spectra and spectral ratios are always noisy, so many have become accustomed to poor fits between theory and data, but it is worthwhile to note that the spectral ratio in Figure 27 does not really look very much like a straight line.

Figure 28 compares the fits of the two norms in the time and linear spectral domains. The S, filtered P and difference functions are shown in time and the spectra of the two difference functions are plotted with frequency. The solid curve ( $t^* = .09$  s) clearly has less area under it. The LS norm minimizes the squared area under the difference function curves in either domain. The norm is most sensitive to those frequencies with largest spectral amplitude. Unless the fit between the two time functions is extraordinary, the difference function generally has high amplitude at the same frequencies the signals do. The largest amplitudes in this case are between 1 and 5 hz. It can be seen in the time domain that this is where most of the signal energy is. At frequencies higher than this, the norm only requires that the spectra be small. Considering the logarithms of functions takes information down in amplitude by orders of magnitude and gives it equal or in this instance even more weight than higher amplitude information. Based on these tests we conclude that the LS norm is superior for estimating  $t^*$ .

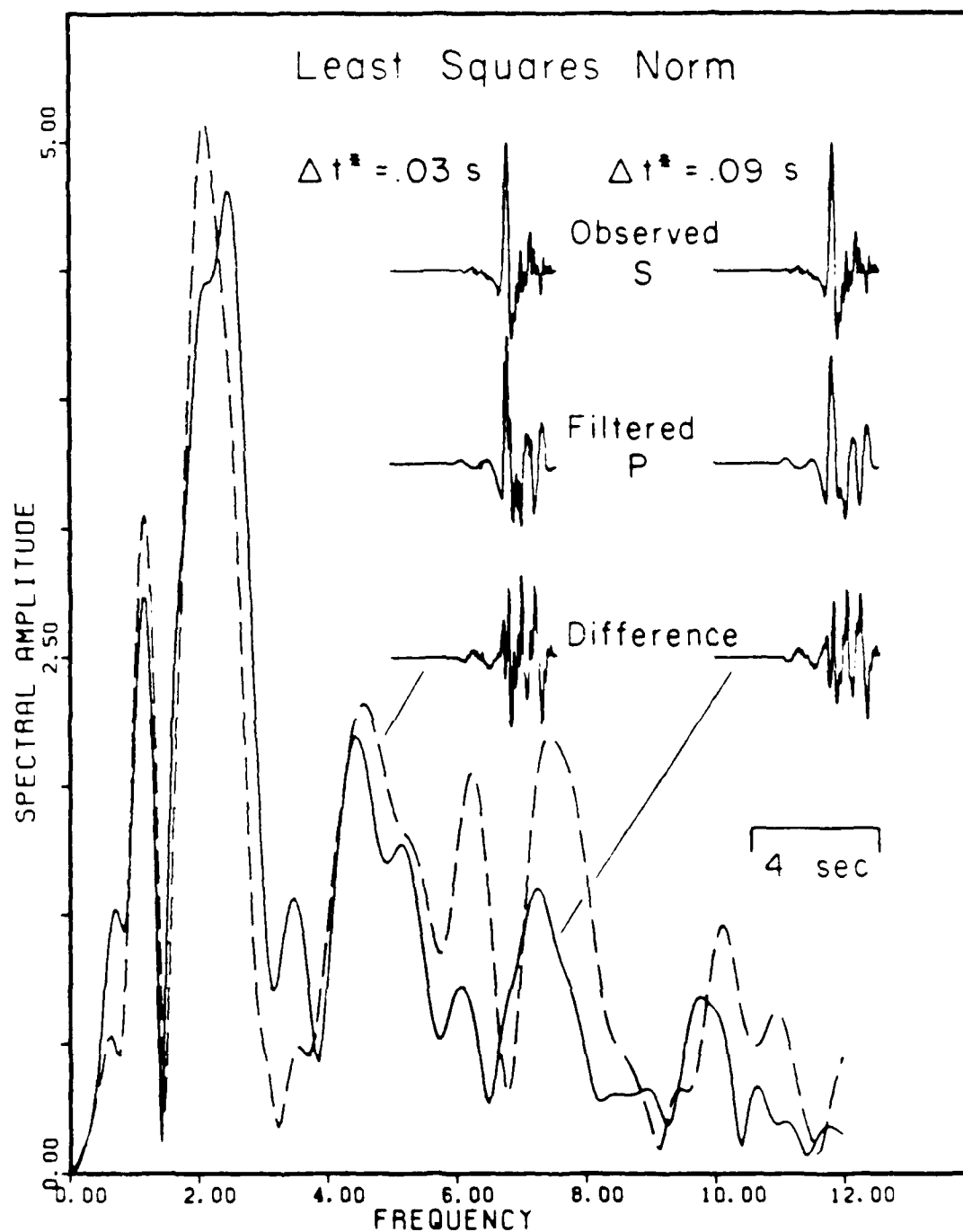


Figure 28. A comparison of the difference functions obtained by the least squares norm (.09s) versus that prescribed by the Ln least squares norm (.09s). The top time trace is observed radial S at ELCE, the next is filtered P and the third is the time domain difference function. The solid line is the spectrum of the difference function for least squares and the dashed line for Ln least squares.

### The Relation Between Relative Strain and Attenuation at Imperial Valley

As discussed above, there are two strong difficulties with trying to detect nonlinear reduction in  $Q$  by correlating relative attenuation of P and S waves with the relative shear strains that they induce. The first is that source directivity causes frequency shifts between P and S which can not be easily distinguished from the effects of relative attenuation. In order to suppress this effect, it is necessary to average observations from many azimuths. The second is that the relationship between effective  $Q$  and relative shear is likely to be a very complex one. All that can be attempted is to find correlations between the two variables by considering large data sets. The Imperial Valley aftershock data set contains 6 good P wave and 32 S wave observations. Given the need for strong averaging, we elected to measure the relative attenuation of each P wave with every S. This yielded 192 separate observations. The LS norm defined above yields an estimate of relative  $t^*$  rather than a direct estimate of shear  $Q$ . However, we can determine the latter because we have a reliable crustal velocity model for Imperial Valley. The elastic compressional and shear wave travel times are computed from this model and shear  $Q$  is determined from

$$Q_p = [T_s - cT_p] / \Delta t^* \quad (34)$$

where

$$c = \frac{4\beta^2}{3\alpha^2} \quad (35)$$

The value of  $c$  varies through the crust, but we repeated our calculations for the minimum and maximum values and found that it does not have a significant effect.

The results of the measurements are shown in Figure 29. As might be expected in situations in which there are many uncontrolled variables, the data shows a large amount of scatter. On the other hand, most types of  $Q$  measurements show significant scatter. It should be noted that the vertical scale is linear and not logarithmic and that virtually all values are confined between 0.0 and 0.05. The trend of  $Q^{-1}$  with shear strain measured in the laboratory as shown in Figure 17 is drawn in for reference. A regression line which was fit to the data is also shown. It shows a slight positive slope, but that slope has a low level of statistical significance. In other words, there is certainly not strong evidence that effective  $Q$  is being reduced due to high shear strains though there is perhaps some suggestion of it. It is worth noting that the value of shear  $Q^{-1}$  at low strain in Figure 17 is .012 which is very near to the average of this suite of measurements which lends some additional confidence as to the validity of the measurement technique.

One final type of information in the earthquake data set which might be looked at to detect anomalous reduction in shear  $Q$  is the observed amplitudes of wave fields with respect to the elastic predictions. This is somewhat more difficult for a double couple than an explosion source because of the azimuthal radiation pattern. More distant points may undergo stronger shear strains than nearer ones if the nearer ones are on nodes. The final Figure, Figure 30, shows the ratio of the observed peak shear strain over the values predicted from elastic theory versus observed peak shear strain. Again, there

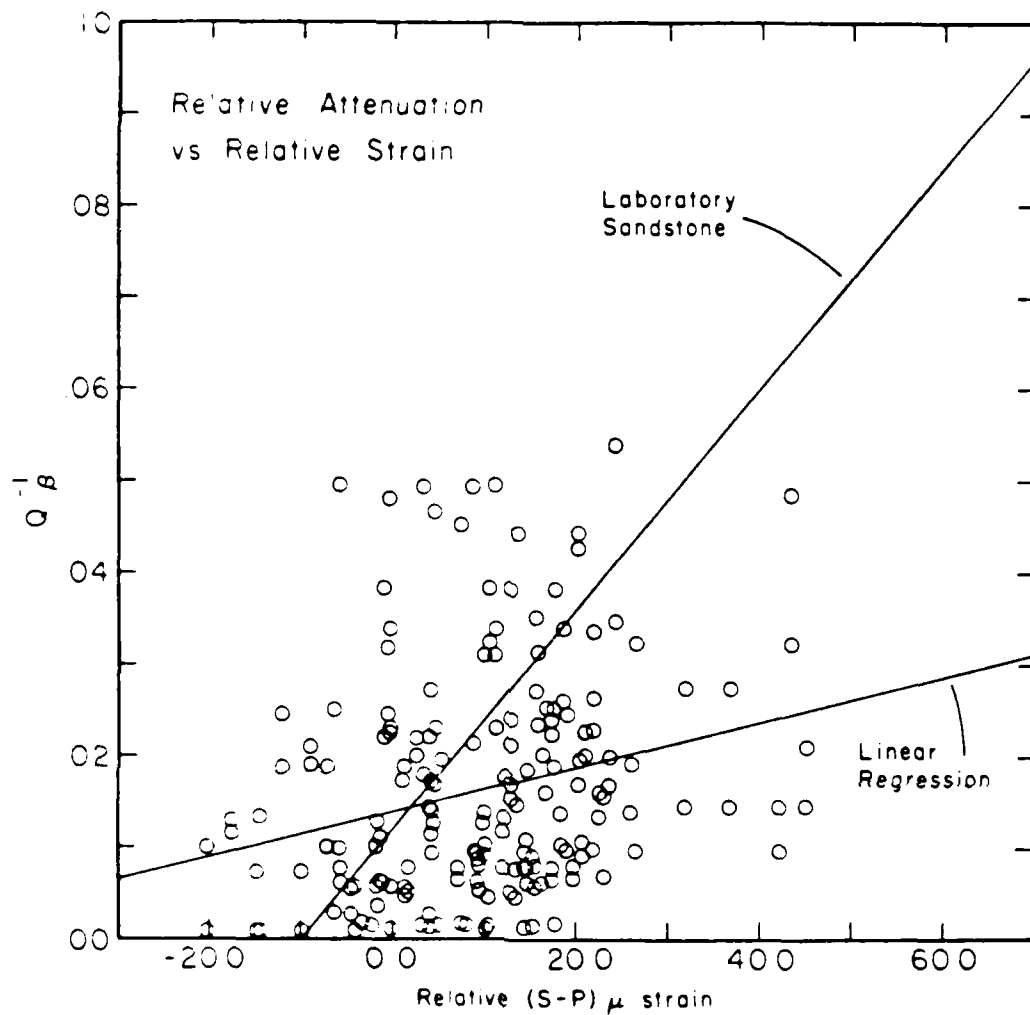


Figure 29. The inverse of shear  $Q$  as a function of the relative shear strains carried by the P and S pulses. The higher slope straight line is a fit to laboratory observations and the lower is a regression fit to the data.

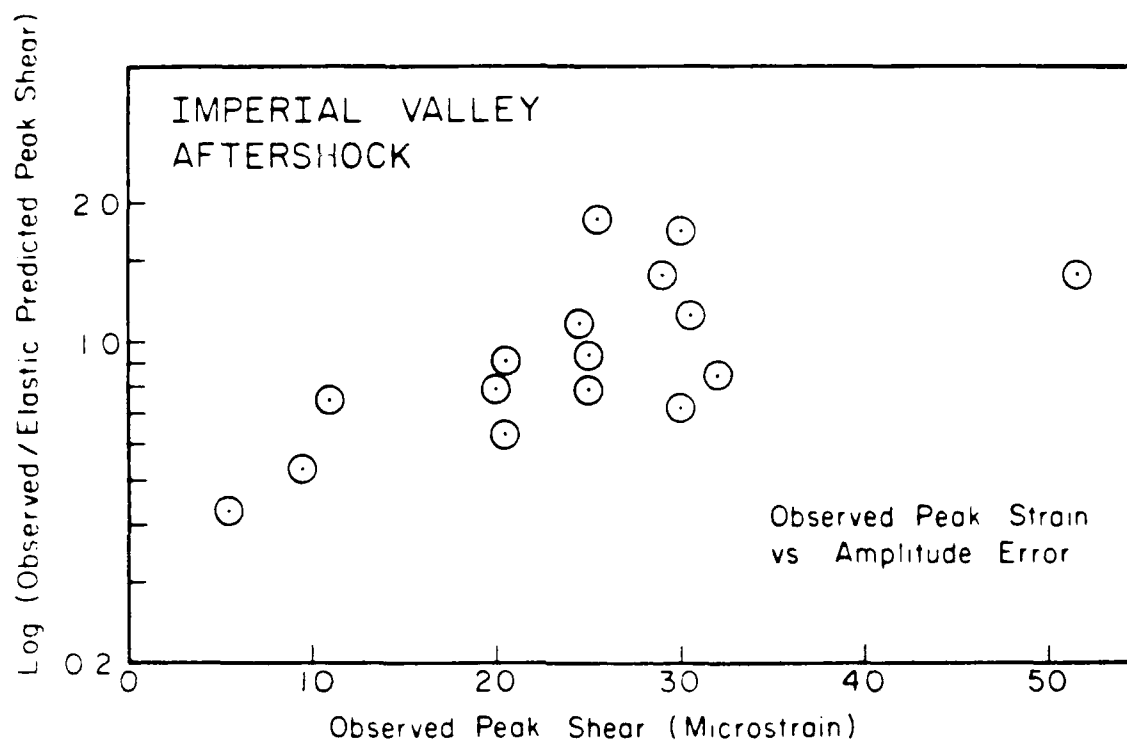


Figure 30. The ratio of observed to predicted (linear elastic) peak shear strain for stations that recorded the Imperial Valley aftershock as a function of the observed peak shear strain. There is no evidence that signals are anomalously attenuated as peak shear increases.

is a slight trend to the data, but nothing strongly convincing. Also the sense of the trend is opposite to what would be expected if more attenuation occurs at higher shear strain.

### DISCUSSION

There are two questions which need to be addressed with regard to nonlinear reduction in  $Q$  due to high strains in the seismic near field. The first is can it be observed to occur at all, and the second is, if it does occur, how significant is it to interpretation of near field data? Several authors have argued on both theoretical and observational grounds that it never occurs in the field (Savage, 1969; Winkler et al., 1979) though they may not have been considering motions near to large nuclear explosions. The answer to the first question, as far as this study is concerned is that any evidence for it is weak. There was the difference in the SCOTCH and BOXCAR  $t^*$  measurements in Table 12 and the trend in Figure 27. However, it could be argued that the effect should be very slight in data of the various types examined here. The effect is strongly pressure sensitive and may only occur in shallow layers near the surface of the earth. The answer to the second question is that accounting for this phenomenon is almost certainly unimportant to the correct interpretation of near-field data. Linear elastic or linear anelastic models are all that is required to explain all important observed phenomena in the range of 2 to 20 km. It is interesting to find that small earthquakes generate strains comparable to those generated by nuclear explosions even if those events are as large as 1000 kt in size. The widespread success of linear anelastic models in explaining near field data from earthquakes should lend confidence to the interpretation of near field

data from explosions using the same approach.



## REFERENCES

- Barker, J. S., S. H. Hartzell, L. J. Burdick and D. V. Helmberger (1985a). Effective source functions for underground nuclear tests at Pahute Mesa from near-field modeling, Final Technical Report WCCP-R-85-02, Contract # F49620-83-C-0028, Woodward-Clyde Consultants, Pasadena.
- Barker, J. S., L. J. Burdick and T. C. Wallace (1985b). Analysis of near-field seismic waveforms from underground nuclear explosions. Scientific Report # 1, AFGL-TR-85-0321, TR # ADA165227, Woodward-Clyde Consultants, Pasadena.
- Barker, J. S., R. W. Burger, L. J. Burdick and T. Lay (1986). Inversion for source parameters of underground nuclear explosions with implications for yield estimation, Scientific Report # 2, AFGL-TR-86-0142, TR # ADA174003, Woodward-Clyde Consultants, Pasadena.
- Brown, M. G. (1982). Inverting for the ocean sound speed structure, Ph.D. thesis, UCSD.
- Burdick, L. J. and G. R. Mellman (1976). Inversion of the body waves from the Borrego Mountain earthquake to the source mechanism, *Bull. Seism. Soc. Am.*, **66**, 1485-1499.
- Burdick, L. J., D. M. Cole, D. V. Helmberger, T. Lay and T. Wallace (1982). Effective source functions from local surface measurements, Final Technical Report WCCP-R-82-01, Contract # MDA903-81-C-0269, Woodward-Clyde Consultants, Pasadena.
- Burdick, L. J., T. C. Wallace and T. Lay (1984). Modeling near-field and teleseismic observations from the Amchitka test site, *J. Geophys. Res.*, **89**, 4373-4388.
- Burdick, L. J., T. Lay, D. V. Helmberger and D. G. Harkrider (1984). Implications of records from the spall zone of the Amchitka tests to nonlinear losses in the source region and to elastic radiation by spall. Annual Technical Report WCCP-R-84-03, Contract # F49620-83-C-0028, Woodward-Clyde Consultants, Pasadena.
- Burdick, L. J. and J. S. Barker (1987). Strains and stresses near to explosions and earthquakes, Scientific Report, AFGL-TR-87-0089, Air Force Geophysical Laboratory, Hanscom AFB, Massachusetts. ADA181198
- Burger, R. W., T. Lay and L. J. Burdick (1987). Average Q and yield estimates from the Pahute Mesa test site, *Bull. Seism. Soc. Am.*, **77**, 1274-1294.
- Carroll, R. D. (1966). Preliminary interpretation of geophysical logs, UE206, Pahute Mesa, Nevada Test Site, Technical letter: Special Studies - 1-27, Supplement 1, U.S. Geol. Survey, Open-file Report.

- Chapman, C. H. and J. A. Orcutt (1985). Least-squares fitting of marine seismic refraction data, *Geophys. J.*, **82**, 339-374.
- Dahlman, A. and H. Israelson (1977). *Monitoring Underground Nuclear Explosions*, Elsevier Scientific Publishing Co., Amsterdam, 440 pp.
- Day, S. M. and J. B. Minster (1986). Decay of wave fields near to an explosive source due to high strain nonlinear attenuation, *J. Geophys. Res.*, **91**, 2113-2132.
- Engdahl, E. R. (1972). Seismic effects of the MILROW and CANNIKIN nuclear explosions, *Bull. Seism. Soc. Am.*, **62**, 1411-1424.
- Hamilton, R. M. and J. H. Healy (1969). Aftershocks of the BENHAM nuclear explosion, *Bull. Seism. Soc. Am.*, **59**, 2271-2281.
- Hartzell, S. H., L. J. Burdick and T. Lay (1983). Effective source functions for Pahute Mesa nuclear tests, Final Technical Report WCCP-R-83-3, Contract # MDA903-82-C-0170, Woodward-Clyde Consultants, Pasadena.
- Hartzell, S. H. and J. N. Brune (1979). The Horse Canyon earthquake of August 2, 1979: Two stage stress release in a strike slip earthquake, *Bull. Seism. Soc. Am.*, **69**, 1161-1173.
- Haskell, N. A. (1967). Analytic approximation for the elastic radiation from a contained underground explosion, *J. Geophys. Res.*, **72**, 2583-2587.
- Helmberger, D. V. (1974). Generalized ray theory for shear dislocations, *Bull. Seism. Soc. Am.*, **64**, 45-64.
- Helmberger, D. V. and D. G. Harkrider (1978). Modeling earthquakes with generalized ray theory, in J. Miklowitz and J. Achenback - eds., *Proc. of IUTAM Symposium: Modern Problems in Elastic Wave Propagation*, J. Wiley & Sons, New York.
- Helmberger, D. V. and D. M. Hadley (1981). Seismic source functions and attenuation from local and teleseismic observations of the NTS events JORUM and HANDLEY, *Bull. Seism. Soc. Am.*, **71**, 51-67.
- Jackson, D. D. (1979). The use of *a priori* data to resolve non-uniqueness in linear inversion, *Geophys. J.*, **57**, 137-157.
- Kanamori, H. (1967). Spectrum of short period core phases in relation to the attenuation in the mantle, *J. Geophys. Res.*, **72**, 2181-2186.
- Langston, C. A. and M. Franco-Spera (1985). Modeling of the Koyna, India aftershock of 12 December 1967, *Bull. Seism. Soc. Am.*, **75**, 651-670.
- Lin, H. and D. V. Helmberger (1985). The 23.19 aftershock of the Imperial Valley earthquake: more evidence for an asperity, *Bull. Seism. Soc. Am.*, **75**, 689-708.

- Marshall, P. D., D. L. Springer and H. C. Rodean (1979). Magnitude corrections for attenuation in the upper mantle, *Geophys. J.*, 57, 609-638.
- Mavko, G. M. (1979). Frictional attenuation: An inherent amplitude dependence, *J. Geophys. Res.*, 84, 4765-4775.
- Mellman, G. R. (1980). A method for waveform inversion of body-wave seismograms, Ph.D. thesis, Caltech.
- Menke, W. (1984). Asymptotic formulas for the apparent Q of weakly scattering three-dimensional media, *Bull. Seism. Soc. Am.*, 74, 1079-1081.
- Mueller, R. A. and J. R. Murphy (1971). Seismic characteristics of underground nuclear detonations, Part I. Seismic scaling law of underground detonations, *Bull. Seism. Soc. Am.*, 61, 1675-1692.
- Murphy, J. R. and R. A. Mueller (1971). Seismic characteristics of underground nuclear detonations, Part II. Elastic energy and magnitude determinations, *Bull. Seism. Soc. Am.*, 61, 1693-1704.
- Orphal, D. L. (1970). The cavity formed by a contained underground nuclear detonation, Report NVO-1163-TM-15, Environmental Research Corp., Las Vegas.
- Perret, W. R. (1976). Surface motion induced by nuclear motions under Pahute Mesa, Report SLA-73-0348, Sandia Laboratories, Albuquerque.
- Savage, J. C. (1969). Comments on a paper by R. B. Gordon and L. A. Davis, *J. Geophys. Res.*, 74, 726-728.
- Shaw, P. R. (1983). Waveform inversion of explosion seismology data, Ph.D. thesis, UCSD.
- Shaw, P. R. and J. A. Orcutt (1985). Waveform inversion of seismic refraction data and applications to young Pacific crust, *Geophys. J.*, 82, 375-414.
- Stewart, R. R., M. N. Toksoz and A. Timur (1983). Strain dependent attenuation: observations and a proposed mechanism, *J. Geophys. Res.*, 88, 546-554.
- Stump, B. W. and L. R. Johnson (1984). Near-field source characterization of contained nuclear explosions in tuff, *Bull. Seism. Soc. Am.*, 74, 1-26.
- Tittman, B. R., J. R. Bulau, M. Abdel-Gawad, L. Ahlberg, C. Salvado and H. Nadler (1981). Experimental results on seismic losses in porous rock over a wide range of frequencies and physical states, Paper presented at the 51st annual SEG meeting, Los Angeles, CA.
- von Seggern, D. and R. Blandford (1972). Source time functions and spectra for underground nuclear explosions, *Geophys. J.*, 31, 83-97.

- Wiggins, R. A. (1972). The general linear inverse problem: Implications of surface waves and free oscillations for earth structure, *Rev. Geophys. Space Phys.*, **10**, 251-285.
- Winkler, K., A. Nur and M. Gladwin (1979). Friction and seismic attenuation in rocks, *Nature*, **277**, 528-531.
- Yao, Z. X. and D. G. Harkrider (1983). A generalized reflection-transmission coefficient matrix and discrete wavenumber method for synthetic seismograms, *Bull. Seism. Soc. Am.*, **73**, 1685-1699.

DISTRIBUTION LIST

Dr. Monem Abdel-Gawad  
Rockwell Internat'l Science Center  
1049 Camino Dos Rios  
Thousand Oaks, CA 91360

Professor Keiiti Aki  
Center for Earth Sciences  
University of Southern California  
University Park  
Los Angeles, CA 90089-0741

Dr. Ralph Alewine III  
DARPA/STO/GSD  
1400 Wilson Boulevard  
Arlington, CA 22209-2308

Professor Shelton S. Alexander  
Geosciences Department  
403 Deike Building  
The Pennsylvania State University  
University Park, PA 16802

Professor Charles B. Archambeau  
Cooperative Institute for Resch  
in Environmental Sciences  
University of Colorado  
Boulder, CO 80309

Dr. Thomas C. Bache Jr.  
Science Applications Int'l Corp.  
10210 Campus Point Drive  
San Diego, CA 92121

Dr. Robert Blandford  
DARPA/STO/GSD  
1400 Wilson Boulevard  
Arlington, CA 22209-2308

Dr. Lawrence Braile  
Department of Geosciences  
Purdue University  
West Lafayette, IN 47907

Dr. James Bulau  
Rockwell Int'l Science Center  
1049 Camino Dos Rios  
P.O. Box 1085  
Thousand Oaks, CA 91360

Dr. Douglas R. Baumgardt  
Signal Analysis & Systems Div.  
ENSQ, Inc.  
5400 Port Royal Road  
Springfield, VA 22151-2388

Dr. G. Blake  
US Dept of Energy/DE 331  
Forrestal Building  
1000 Independence Ave.  
Washington, D.C. 20585

Dr. S. Bratt  
Science Applications Int'l Corp.  
10210 Campus Point Drive  
San Diego, CA 92121

Woodward-Clyde Consultants  
ATTN: Dr. Lawrence J. Burdick  
Dr. Jeff Barker  
P.O. Box 93245  
Pasadena, CA 91109-3245 (2 copies)

Dr. Roy Burger  
1221 Serry Rd.  
Schenectady, NY 12309

Professor Robert W. Clayton  
Seismological Laboratory/Div. of  
Geological & Planetary Sciences  
California Institute of Technology  
Pasadena, CA 91125

Dr. Vernon F. Cormier/Earth Resources  
Lab, Dept of Earth, Atmospheric and  
Planetary Sciences  
MIT - 42 Carleton Street  
Cambridge, MA 02142

Professor Anton W. Dainty  
ARL/LWH  
Hanscom AFB, MA 01731

Dr. Zoltan A. Der  
ENSQ, Inc.  
5400 Port Royal Road  
Springfield, VA 22151-2388

Professor Adam Dziewonski  
Hoffman Laboratory  
Harvard University  
20 Oxford St.  
Cambridge, MA 02138

Professor John Ebel  
Dept of Geology & Geophysics  
Boston College  
Chestnut Hill, MA 02167

Dr. Jack Evernden  
USGS-Earthquake Studies  
345 Middlefield Road  
Menlo Park, CA 94025

Professor John Ferguson  
Center for Lithospheric Studies  
The University of Texas at Dallas  
P.O. Box 830688  
Richardson, TX 75083-0688

Mr. Edward Giller  
Pacific Sierra Research Corp.  
1401 Wilson Boulevard  
Arlington, VA 22209

Dr. Jeffrey W. Given  
Sierra Geophysics  
11255 Kirkland Way  
Kirkland, WA 98033

Professor Steven Grand  
Department of Geology  
245 Natural History Building  
1301 West Green Street  
Urbana, IL 61801

Professor Roy Greenfield  
Geosciences Department  
403 Deike Building  
The Pennsylvania State University  
University Park, PA 16802

Dr. James Hannon  
Lawrence Livermore Nat'l Lab.  
P.O. Box 808  
Livermore, CA 94550

Professor David G. Harkrider  
Seismological Laboratory  
Div of Geological & Planetary Sciences  
California Institute of Technology  
Pasadena, CA 91125

Professor Donald V. Helmberger  
Seismological Laboratory  
Div of Geological & Planetary Sciences  
California Institute of Technology  
Pasadena, CA 91125

Professor Eugene Herrin  
Institute for the Study of Earth  
& Man/Geophysical Laboratory  
Southern Methodist University  
Dallas, TX 75275

Professor Robert B. Herrmann  
Department of Earth & Atmospheric  
Sciences  
Saint Louis University  
Saint Louis, MO 63150

U.S. Arms Control & Disarm. Agency  
ATTN: Mrs. M. Hoinkes  
Div. of Multilateral Affairs  
Room 5499  
Washington, D.C. 20451

Professor Lane R. Johnson  
Seismographic Station  
University of California  
Berkeley, CA 94720

Professor Thomas H. Jordan  
Department of Earth, Atmospheric  
and Planetary Sciences  
Mass Institute of Technology  
Cambridge, MA 02139

Dr. Alan Kafka  
Department of Geology &  
Geophysics  
Boston College  
Chestnut Hill, MA 02167

Ms. Ann Kerr  
DARPA/STO/GSD  
1400 Wilson Boulevard  
Arlington, VA 22209-2308

Professor Charles A. Langston  
Geosciences Department  
403 Deike Building  
The Pennsylvania State University  
University Park, PA 16802

Professor Thorne Lay  
Department of Geological Sciences  
1006 C.C. Little Building  
University of Michigan  
Ann Harbor, MI 48109-1063



Dr. Arthur Lerner-Lam  
Lamont-Boherty Geological Observatory  
Columbia University  
Palisades, NY 10964

Dr. George R. Mellman  
Sierra Geophysics  
11250 Kirkland Way  
Kirkland, WA 98033

Professor Brian T. Mitchell  
Department of Earth & Atmospheric  
Sciences  
Saint Louis University  
Saint Louis, MO 63156

Professor Thomas V. McEvilly  
Sismographic Station  
University of California  
Berkeley, CA 94720

Dr. Keith L. McLaughlin  
Teledyne Geotech  
314 Montgomery Street  
Alexandria, VA 22314

Mr. Jack Murphy - S-CUBED  
Boston Geophysics Office  
11-80 Sunrise Valley Drive  
Suite 1212  
Boston, VA 22291

Dr. Carl Newton  
Los Alamos National Lab.  
P.O. Box 1663  
Mail Stop C335, Group E553  
Los Alamos, NM 87545

Professor Otto W. Nuttli  
Department of Earth &  
Atmospheric Sciences  
Saint Louis University  
Saint Louis, MO 63156

Professor J. A. Orcutt  
Geological Sciences Div.  
Univ. of California at  
San Diego  
La Jolla, CA 92093

Dr. Frank F. Pilotte  
Director of Geophysics  
Headquarters Air Force Technical  
Applications Center  
Patrick AFB, Florida 32925-6001

Professor Keith Priestley  
University of Nevada  
Mackay School of Mines  
Reno, Nevada 89557

Mr. Jack MacLin  
USGS - Geology, Rm 3 C136  
Mail Stop 928 National Center  
Reston, VA 22092

Professor Paul G. Richards  
Lamont-Doherty Geological  
Observatory of Columbia Univ.  
Palisades, NY 10964

Dr. Norton Rimer  
S-CBED  
A Division of Maxwell Lab  
P.O. 1620  
La Jolla, CA 92038-1620

Dr. George H. Rothe  
Chief, Research Division  
Geophysics Directorate  
U.S. Air Force Technical  
Applications Center  
Patrick AFB, Florida 32925-6001

Professor Larry J. Ruff  
Department of Geological Sciences  
1006 C.C. Little Building  
University of Michigan  
Ann Arbor, MI 48109-1063

Dr. Alan S. Ryall, Jr.  
Center of Seismic Studies  
1300 North 17th Street  
Suite 1450  
Arlington, VA 22209-2308

Professor Charles G. Sammis  
Center for Earth Sciences  
University of Southern California  
University Park  
Los Angeles, CA 90089-0741

Dr. David C. Simpson  
Lamont-Doherty Geological Observ.  
of Columbia University  
Palisades, NY 10964

Dr. Jeffrey L. Stevens  
S-CBED,  
A Division of Maxwell Laboratory  
P.O. Box 1620  
La Jolla, CA 92038-1620

Professor Brian Stump  
Institute for the Study of Earth & Man  
Geophysical Laboratory  
Southern Methodist University  
Dallas, TX 75275

Professor Ta-liang Teng  
Center for Earth Sciences  
University of Southern California  
University Park  
Los Angeles, CA 90089-0741

Dr. R. B. Fittmann  
Rockwell International Science Ctr  
1049 Camino Dos Rios  
P.O. Box 1085  
Thousand Oaks, CA 91360

Professor M. Nafi Toksoz/Earth Resources  
Lab - Dept of Earth, Atmospheric and  
Planetary Sciences  
MIT - 42 Carleton Street  
Cambridge, MA 02142

Dr. Lawrence Turnbull  
OSWR/NED  
Central Intelligence Agency  
CIA, Room 5G48  
Washington, D.C. 20505

Professor Terry C. Wallace  
Department of Geosciences  
Building #11  
University of Arizona  
Tucson, AZ 85721

Professor John H. Woodhouse  
Hofmann Laboratory  
Harvard University  
2 Oxford St.  
Cambridge, MA 02138

\*\*\*

ASIA, PA  
1200 Wilson Boulevard  
Arlington, VA 22209

Defense Technical  
Information Center  
Cameron Station  
Alexandria, VA 22314  
(12 copies)

Defense Intelligence Agency  
Directorate for Scientific &  
Technical Intelligence  
Washington, D.C. 20301

Defense Nuclear Agency/SPSS  
ATTN: Dr. Michael Shore  
6501 Telegraph Road  
Alexandria, VA 22310

AFOSR/SPG  
ATTN: Director  
Bldg 410, Room C22  
Dolling AFB, Wash D.C. 20332

AFTAC/CA (STINFO)  
Patrick AFB, FL 32925-6001

U.S. Geological Survey  
ATTN: Dr. T. Hanks  
Earthquake Resch Center  
405 Middlefield Road  
Menlo Park, CA 94025

SRI International  
333 Ravensworth Avenue  
Menlo Park, CA 94025

Center for Seismic Studies  
ATTN: Dr. C. Romney  
1300 North 17th St., Suite 1450  
Arlington, VA 22209 (3 copies)

Science Horizons, Inc.  
ATTN: Dr. Bernard Minster  
Dr. Theodore Cherry  
710 Encinitas Blvd., Suite 101  
Encinitas, CA 92024 (2 copies)

Dr. G. A. Bollinger  
Department of Geological Sciences  
Virginia Polytechnical Institute  
21044 Derring Hall  
Blacksburg, VA 24061

Dr. L. Sykes  
Lamont Doherty Geological Observ.  
Columbia University  
Palisades, NY 10964

Dr. S. W. Smith  
Geophysics Program  
University of Washington  
Seattle, WA 98195

Dr. L. Timothy Long  
School of Geophysical Sciences  
Georgia Institute of Technology  
Atlanta, GA 30332

Dr. N. Biswas  
Geophysical Institute  
University of Alaska  
Fairbanks, AK 99701

Dr. Freeman Gilbert - Institute of  
Geophysics & Planetary Physics  
Univ. of California at San Diego  
P.O. Box 109  
La Jolla, CA 92037

Dr. Pradeep Talwani  
Department of Geological Sciences  
University of South Carolina  
Columbia, SC 29208

Dr. Donald Forsyth  
Dept. of Geological Sciences  
Brown University  
Providence, RI 02912

Dr. Jack Oliver  
Department of Geology  
Cornell University  
Ithaca, NY 14850

Dr. Muawia Barazangi  
Geological Sciences  
Cornell University  
Ithaca, NY 14853

Wadsworth Associates  
Attn: Dr. George Sutton,  
Dr. Jeff Carter, Dr. Paul Pomeroy  
Box 111  
Lake Ridge, TX 77454 (3 copies)

Dr. Bob Smith  
Department of Geophysics  
University of Utah  
140 East 2nd South  
Salt Lake City, UT 84112

Dr. Anthony Gangi  
Texas A&M University  
Department of Geophysics  
College Station, TX 77843

Dr. Gregory E. Young  
USQ, Inc.  
410 Port Royal Road  
Springfield, CA 22151

Wiedlinger Associates  
Attn: Dr. Gregory Wojcik  
620 Hansen Way, Suite 100  
Palo Alto, CA 94304

Dr. Leon Knopoff  
University of California  
Institute of Geophysics  
& Planetary Physics  
Los Angeles, CA 90024

Dr. Kenneth H. Olsen  
Los Alamos Scientific Lab.  
Post Office Box 1663  
Los Alamos, NM 87545

Professor Jon F. Claerbout  
Professor Amos Nur  
Dept. of Geophysics  
Stanford University  
Stanford, CA 94305 (2 copies)

Dr. Robert Burridge  
Schlumberger-Doll Resch Co.  
Old Quarry Road  
Ridgefield, CT 06877

Dr. Robert Phinney/Dr. F.A. Dahlen  
Dept of Geological  
Geophysical Sci. University  
Princeton University  
Princeton, NJ 08540 (2 copies)

New England Research, Inc.  
ATTN: Dr. Randolph Martin III  
P.O. Box 857  
Norwich, VT 05055

Sandia National Laboratory  
ATTN: Dr. H. B. Durham  
Albuquerque, NM 87185

AFGL/XO  
Hanscom AFB, MA 01731-5000

AFGL/LW  
Hanscom AFB, MA 01731-5000

AFGL/SULL  
Research Library  
Hanscom AFB, MA 01731-5000 (2 copies)

Secretary of the Air Force (SAFRD)  
Washington, DC 20330

Office of the Secretary Defense  
DDR & E  
Washington, DC 20330

HQ DNA  
ATTN: Technical Library  
Washington, DC 20305

Director, Technical Information  
DARPA  
1400 Wilson Blvd.  
Arlington, VA 22209

Los Alamos Scientific Laboratory  
ATTN: Report Library  
Post Office Box 1663  
Los Alamos, NM 87544

Dr. Thomas Weaver  
Los Alamos Scientific Laboratory  
Los Alamos, NM 97544

Dr. Gary McCortor  
Mission Research Corp.  
733 State Street  
P.O. Drawer 719  
Santa Barbara, CA 93102

Dr. Al Florence  
SRI International  
333 Ravenwood Avenue  
Menlo Park, CA 94025-3493

Dr. W. H. K. Lee  
USGS  
Office of Earthquakes, Volcanoes,  
& Engineering  
Branch of Seismology  
345 Middlefield Rd  
Menlo Park, CA 94025

\*\*\*



Dr. Peter Basham/Earth Physics Branch  
Department of Energy and Mines  
1 Observatory Crescent  
Ottawa, Ontario  
CANADA K1A 0Y3

Dr. Eduard Berg  
Institute of Geophysics  
University of Hawaii  
Honolulu, HI 96822

Dr. Michel Bouchon - Universite  
Scientifique et Medicale de Grenoble  
Lab de Geophysique - Interne et  
Tectonophysique - I.R.I.G.M-B.P.  
38402 St. Martin D'Heres  
Gedex FRANCE

Dr. Hilmar Bungum/NTNF/NORSAR  
P.O. Box 51  
Norwegian Council of Science,  
Industry and Research, NORSAR  
N-2007 Kjeller, NORWAY

Dr. Kin-Yip Chun  
Geophysics Division  
Physics Department  
University of Toronto  
Ontario, CANADA M5S 1A7

Dr. Alan Douglas  
Ministry of Defense  
Blacknest, Brimpton,  
Reading RG7-4RS  
UNITED KINGDOM

Professor Peter Harjes  
Institute for Geophysik  
Rhur University/Bochum  
P.O. Box 102148, 4630 Bochum 1  
FEDERAL REPUBLIC OF GERMANY

Dr. E. Husebye  
NTNF/NORSAR  
P.O. Box 51  
N-2007 Kjeller, NORWAY

Mr. Peter Marshall, Procurement  
Executive, Ministry of Defense  
Blacknest, Brimpton,  
Reading RG7-4RS  
UNITED KINGDOM

Dr. B. Massinon  
Societe Radiomana  
27, Rue Claude Bernard  
75005, Paris, FRANCE

Dr. Pierre Mechler  
Societe Radiomana  
27, Rue Claude Bernard  
75005, Paris, FRANCE

Dr. Ben Menaheim  
Weizman Institute of Science  
Rehovot, ISRAEL 951729

Dr. Svein Mykkeltveit  
NTNF/NORSAR  
P.O. Box 51  
N-2007 Kjeller, NORWAY

Dr. Frode Ringdal  
NTNF/NORSAR  
P.O. Box 51  
N-2007 Kjeller, NORWAY

University of Hawaii  
Institute of Geophysics  
ATTN: Dr. Daniel Walker  
Honolulu, HI 96822

\*\*\*

END

DATE

FILMED

6-88

DTIC